Title
High Dimensional Descriptors of Subcortical Shape as a Basis for Biomarker Discovery in HIV and Major Depressive Disorder

Author
Wade, Benjamin Wade

Publication Date
2016

Peer reviewed|Thesis/dissertation

UNIVERSITY OF CALIFORNIA

Los Angeles

High Dimensional Descriptors of Subcortical Shape as a Basis for Biomarker Discovery in HIV and Major Depressive Disorder

A dissertation submitted in partial satisfaction

of the requirements for the degree Doctor of Philosophy

in Bioengineering

by

Benjamin Wade

2016

ABSTRACT OF THE DISSERTATION

High Dimensional Descriptors of Subcortical Shape as a Basis for Biomarker Discovery in HIV and Major Depressive Disorder

by

Benjamin Wade

Doctor of Philosophy in Bioengineering

University of California, Los Angeles, 2016

Professor Daniel B. Ennis, Co-Chair

Professor Paul Thompson, Co-Chair

Neurological disorders are commonly characterized by disease-specific profiles of neurodegeneration that can be quantified using structural magnetic resonance imaging (MRI). Historically, most structural MRI-based studies of disease-related neurodegeneration have relied on volumetric descriptions of affected brain regions. However, reporting a single scalar summarization of a brain region's morphometry ignores a far richer source of information contained in local descriptions of the structure's morphometry. As a result, anatomical profiles of numerous brain disorders spanning various stages of onset, progression, recovery and their interplay with both cognitive and clinical factors remain poorly described. A promising approach to capturing local structural variations is a family of modeling techniques collectively referred to

as surface-based shape analyses. In the set of studies reported in this dissertation we aimed to identify shape-based biomarkers for the progression of HIV-associated neurodegeneration and prognostic biomarkers for patients with major depression likely to experience symptomatic relief following electroconvulsive therapy. Our studies' conclusions indicate that the incorporation of shape measures are important both for descriptive and predictive modeling frameworks, beyond classical volumetric descriptors. Specifically, we report shape-based patterns of abnormal neurodegeneration among HIV+ pediatric and geriatric cohorts in regions of the basal ganglia. We further leveraged subcortical shape measures in a machine-learning framework to improve the prediction of clinical response to electroconvulsive therapy in patients suffering from major depressive disorder. Our findings suggest that including these descriptors will enhance descriptive models of neurodegeneration and may inform personalized treatment strategies.

The dissertation of Benjamin Wade is approved.

Katherine L. Narr

Marvin Bergsneider

Ian Cook

Thomas R. Belin

Paul Thompson, Committee Co-Chair

Daniel B. Ennis, Committee Co-Chair

University of California, Los Angeles

2016

In dedication to my mother and the memory of my father
who were a constant support along my path.

Table of Contents

BIOGRAPHICAL SKETCH

Benjamin Wade completed his first two years of college studies at Butte College. He attended the University of California, Berkeley, from 2008 to 2010 where he graduated with a degree in interdisciplinary studies, focusing on Neuroscience, Philosophy and Religious Studies. While attending Berkeley, he worked as an undergraduate research assistant in the Relationships and Social Cognition Lab under Professor Ozlem Ayduk studying the neural correlates of delay of gratification in children using functional magnetic resonance imaging.

After completing his undergraduate studies, he spent two years working in the National Institute of Mental Health, Child Psychiatry Branch, under Jay Giedd. There he studied associations between supernumerary sex chromosomes and the morphometry of the corpus callosum, identifying differential contributions to callosum morphometry from X- and Y-linked genes.

In 2012, he entered the Ph.D. program in Bioengineering, Signal and Image Processing, at the University of California, Los Angeles, and was the recipient of the National Science Foundation's Graduate Research Fellowship which funded his first three years of studies. Working with Professors Paul Thompson and Katherine Narr, he applied subcortical shape analyses and machine learning techniques to characterize the neuropathology of HIV infection, mild traumatic brain injury, and predict clinical response to electroconvulsive therapy in patients with major depressive disorder.

Chapter 1: Introduction

Background and motivation

Neurological disorders are commonly characterized by disease-specific profiles of brain tissue atrophy or inflammation. Depending upon the disorder and its severity, the associated patterns of tissue pathology may be homogenously or heterogeneously distributed throughout the brain. Magnetic resonance imaging (MRI) affords a rich description of the subtleties of the brain's structure. Millimeter to sub-millimeter resolution has become relatively commonplace in structural MRI research. Aided by recent advances in image registration methods and developments in pattern recognition methods that are capable of discerning profiles of variation embedded in high dimensional spaces, development of predictive and descriptive biomarkers for neurological disorders has become an increasingly tractable pursuit.

The development of precise biomarkers offers hope of improved medical prognoses and personalized treatments upon translation to the clinical setting in the form of computer-assisted diagnosis (CAD) systems. In theory, a CAD system can discern more subtle patterns of variation than even the well-trained human eye can resolve. Abnormal patterns of brain morphometry embedded in spaces beyond a human's ability to discern may contain information predictive of a patient's likelihood of treatment response or relapse. Because the phenotypes of many common disorders remain poorly understood – whether due to imprecise definitions encompassing several related yet separable pathological states or a paucity of research – across various stages of onset and recovery it is critical to develop algorithms providing both descriptive and predictive insight into their progression.

Effective biomarkers have several important properties: they are highly accurate (maximizing sensitivity, specificity and positive and negative predictive values), minimally invasive while being financially and computationally cost effective. Historically, regional volume has been the primary means of quantifying brain structure due to its relative computational simplicity and intuitive representation of morphometry. However, volume is a simple scalar value that, while informative, fails to leverage the information captured by modern high-resolution scanners and imaging sequences. In recent years, several shape-analytic methods have been developed to model variation of a structure's morphological properties. These are generally divided into local and global descriptors of shape characteristics. Local shape descriptors are capable of localizing regions of variation within a structure – a beneficial property for both clinical applications and use in pattern recognition. In the body of work presented in this dissertation I leverage local surface-based shape modeling to identify and validate biomarkers for the neurological manifestations of human immunodeficiency virus (HIV) and major depressive disorder (MDD).

Background on neurological manifestations of HIV

Rapidly following infection (Epstein and Gelbard, 1999; Li *et al*, 2014) HIV invades the central nervous system by crossing the blood-brain barrier via infected monocytes (Gartner, 2000; Kim *et al*, 2003; Koenig *et al*, 1986). These infected monocytes go on to produce proinflammatory cytokines such as TNF-α leading to microglia and astrocyte activation (Hong and Banks, 2015) resulting release of excitotoxic amino acids, chemokines and cytokines (Gendelman *et al*, 1994; Langford and Masliah, 2001; Zahr *et al*, 2014). Chronic immune activation and inflammation resulting from this process is widely considered the primary mechanism for HIV-related neurodegeneration though other contributing mechanisms include

disrupted metabolic processes, and even neurotoxic side effects of prolonged cART exposure. As well as the observed effects of antiviral treatments, several clinical markers have been related to HIV infection and cognitive performance. Higher HIV RNA viral load and lower nadir CD4 cell counts have widely been linked to more impaired cognitive performance (Martin *et al*, 2006; Nachman *et al*, 2012; Smith *et al*, 2012; Wood *et al*, 2009) which is in turn associated with underlying neurodegeneration. Numerous groups have reported on HIV-related neurodegeneration with convergent evidence highlighting abnormal cortical and subcortical brain morphometry related to HIV positivity, CD4 t-cell count, viral load and reception of the combination antiretroviral therapy (cART) (Ances *et al*, 2012; Becker *et al*, 2012; Fennema-Notestine *et al*, 2013; Jernigan *et al*, 2011; Kallianpur *et al*, 2013; Ragin *et al*, 2015; Wade *et al*, 2015; Wilson *et al*, 2015).

Investigations of structural MRI widely report age-disproportionate degrees of atrophy among HIV+ cohorts in adults (Becker *et al*, 2012; Thompson *et al*, 2005; Towgood *et al*, 2012). Diffusion tensor imaging has also revealed possible interaction effects of HIV infection and age in the reduction of fractional anisotropy and increase of mean diffusivity within subcortical white matter and frontal regions (Chen *et al*, 2009). Studies investigating magnetic resonance spectroscopy also suggest that CNS HIV infection parallels the aging process. For instance, Chang and Harezlak (Chang *et al*, 2004; Harezlak *et al*, 2011) both reported higher ratios of choline compounds : total creatine and myoinositol : creatine in the basal ganglia associated with aging and HIV status.

The life expectancy of HIV+ individuals has dramatically improved since the advent of modern cART regimens and it is now projected that by the year 2020 approximately 70% of HIV+ individuals within the US will be aged 50 or above. Perinatal HIV infection also remains a

major concern in the developing world though long-term survival of infected children has also improved substantially in the cART era. Despite stable treatment upwards of 50% of infected people suffer a degree of HIV-associated neurocognitive disorder (HAND). The prevalence of HAND has not reduced in the cART era though the more severe manifestations of its effects have reduced considerably (Nasi *et al*, 2014). Given the prolonged life expectancy of infected individuals and the potential complications presented by synergistic effects of aging and HIV infection, it is increasingly urgent to understand how the structure of the developing and aging brain might be affected by HIV infection and its clinical sequelae. Neuroimaging currently plays two clinical roles in the evaluation of HIV infection: i) the detection of cerebral atrophy or encephalopathy and ii) the identification of secondary complications resulting from immunosenescence such as HIV-related tumors and opportunistic infections (e.g. toxoplasmosis). The development of more sensitive biomarkers for the neurological effects of HIV may aid in the monitoring of the progression of the disorder and identify patients more likely to suffer severe cognitive decline.

Background on major depressive disorder and electroconvulsive therapy

The prevalence of major depressive disorder (MDD) is staggering, affecting approximately 10-20% of the U.S. population (Kessler *et al*, 2003; Weissman *et al*, 1996) and contributes to about 1 million reported suicides globally each year. The average annual cost to the U.S. alone is estimated to be $42 billion (Grieve *et al*, 2013), outranking the combined costs of cancer and diabetes. Clinical manifestations of MDD encompass multiple dimensions including, but not limited to, anhedonia, apathy and melancholy. This heterogeneity presents considerable challenges to investigators seeking to identify neurobiological mechanisms of MDD presentation and recovery. Brain imaging of MDD has revealed fairly consistent findings of

reduced hippocampal volume (Campbell *et al*, 2004; Schmaal *et al*, 2016) and notable alterations of the anterior cingulate cortex and frontal gyri (Du *et al*, 2012). Functional alterations including hypoactivity of the nucleus accumbens (Liu *et al*, 2011), hyperactivity of the amygdala in response to stressful stimuli (Groenewold *et al*, 2013) and abnormal prefrontal activation patterns (Phillips *et al*, 2003) are widely reported as well.

Antidepressant drugs and behavioral therapy are the most frequently prescribed treatments for MDD, however, nearly two-thirds of patients undergo several drug trials prior to experiencing symptom relief and, even so, up to a third of patients will remain unresponsive to treatment. Electroconvulsive therapy (ECT) elicits rapid symptom relief in approximately 60-70% of patients (Husain *et al*, 2004; Kho *et al*, 2003). Because of this acute efficacy it is an optional line of treatment for patients who remain unresponsive to several lines of drug and behavioral therapy or are at immanent risk of suicide (Kellner *et al*, 2012). Although the many symptomatic dimensions of MDD are commonly linked to disturbances in the prefrontal cortex, anterior cingulate, hippocampus, amygdala, thalamus and striatal/pallidal regions (Drevets *et al*, 2008; Lorenzetti *et al*, 2009; Schmaal *et al*, 2015) the neural mechanisms mediating clinical response to ECT remain largely unknown.

While highly effective, ECT also carries several side effects including temporary memory loss and confusion. Patients seeking this secondary line of treatment would be best served if biomarkers indicating their likelihood of response, degree of response and probability of long-term relapse or sustained response were developed to identify patients likely and unlikely to benefit from treatment. These factors would aid clinicians and patients in navigating the medical decision making process and weighing the potential risks versus rewards of proceeding with ECT.

Organization and overview

The chapters of this dissertation consist of published articles (Chapters 2, 3 and 5), articles in review (Chapter 4) and ongoing research (Chapters 6 and 7). Chapter 2 begins by exploring the question of how to handle high-dimensional shape descriptors in predictive, machine learning framework. Given its high dimensionality, shape data may be more prone to the curse of dimensionality. To explore this possibility we compared the performances of joint feature selection and classification algorithms in classifying Alzheimer's disease and its prodromal state, mild cognitive impairment, apart from typically aging controls using only subcortical shape descriptors. In doing so, we attempted to understand how different strategies of modeling and feature selection would affect classification performances across various ratios of sample sizes to feature set sizes when the feature set is composed exclusively of shape data.

Chapters 3 and 4 focus on the identification and modeling of abnormal brain morphometry resulting from HIV infection in two distinct age groups: geriatrics and pediatrics. In chapter 3 we explore how long-term HIV infection affects the elderly brain aging process. To address this we investigated subcortical shape and volume abnormalities in 63 elderly HIV+ and 31 HIV- participants from the San Francisco area. Chapter 4 similarly addresses whether seropositivity, reception, timing or duration of cART, CD4 count and viral detectability are related to developmental trajectories of subcortical brain structures in 43 perinatally-infected HIV+ and 53 uninfected Thai children. Here we again assessed development using subcortical shape and volume measures in cross-sectional and longitudinal frameworks spanning a one-year time frame.

Chapters 5, 6 and 7 address the development of biomarkers for depression and prediction of clinical response to ECT. In chapter 5 we build on previous work (Joshi *et al*, 2015) that

modeled structural plasticity induced by ECT in regions of the hippocampus and amygldala. There we investigated how ECT affects regions of the striatum and basal ganglia. We modeled changes in the morphometry of these structures longitudinally over the course of ECT index. We additionally developed a support-vector machine classifier to predict individuals who would be responsive to ECT based on pre-treatment patterns of structural brain morphometry.

Chapter 6 consists of ongoing work in the development of prognostic biomarkers for the identification of patients with MDD likely to experience symptomatic remission following ECT. This is a natural extension of work presented in chapter 5 where clinical response was the outcome. The prediction of remission is a more difficult problem considering remission rate is lower than response rate. Responders are typically defined as patients who experience a 50% or more reduction in depressive symptoms according to the clinician-administered Hamilton Depression Rating Scale (HAM-D, outlined in Chapter 5). Remission, however, is defined by a more complete reduction in depressive symptoms, requiring a final HAM-D-17 score ≤ 7 or 8; remitters are necessarily a subset of subjects who are responders.

Chapter 7 outlines current work in biomarker development with the aim of stratifying patients based on their predicted probability of clinical relapse at 6-months following ECT index. There we examine whether relapse prediction is viable from pre-treatment measures of brain structure, end-of-index measures and changes in brain structure over ECT index. Naturally, the ability to predict subsequent relapse prior to treatment would be the most favorable option since relapse risk could then be factored into the initial decision of whether a patient should receive ECT. These lines of research have clear importance as the ability to identify highly responsive patients and perform relapse risk stratification would inform the medical decision making

process, improve personalized treatment strategies and mitigate the incurrence of adverse treatment side effects when a patient is unlikely to benefit.

References

Ances BM, Ortega M, Vaida F, Heaps J, Paul R (2012). Independent effects of HIV, aging, and HAART on brain volumetric measures. *Journal of Acquired Immune Deficiency Syndromes* **59**(1944-7884 (Electronic)): 469-477.

Becker JT, Maruca V, Kingsley LA, J.M. S, Alger JR, Barker PB*, et al* (2012). Factors affecting brain structure in men with HIV disease in the post-HAART era. *Neuroradiology* **54**(1432-1920 (Electronic)): 113-121.

Campbell S, Marriott M, Nahmias C, MacQueen GM (2004). Lower hippocampal volume in patients suffering from depression: a meta-analysis. *Am J Psychiatry* **161**(4): 598-607.

Chang L, Lee PL, Yiannoutsos CT, Ernst T, C.M. M, Richards T*, et al* (2004). A multicenter in vivo proton-MRS study of HIV-associated dementia and its relationship to age. *NeuroImage* **23**(1053-8119 (Print)): 1336-1347.

Chen Y, An H, Zhu H, Stone T, Smith JK, Hall C*, et al* (2009). White matter abnormalities revealed by diffusion tensor imaging in non-demented and demented HIV+ patients. *NeuroImage* **47**(1095-9572 (Electronic)): 1154-1162.

Drevets WC, Price Jl Fau - Furey ML, Furey ML (2008). Brain structural and functional abnormalities in mood disorders: implications for neurocircuitry models of depression. (1863-2653 (Print)).

Du MY, Wu QZ, Yue Q, Li J, Liao Y, Kuang WH*, et al* (2012). Voxelwise meta-analysis of gray matter reduction in major depressive disorder. *Progress in neuro-psychopharmacology & biological psychiatry* **36**(1): 11-16.

Epstein LG, Gelbard HA (1999). HIV-1-induced neuronal injury in the developing brain. *Journal of leukocyte biology* **65**(4): 453-457.

Fennema-Notestine C, Ellis RJ, Archibald SL, Jernigan TL, Letendre SL, Notestine RJ*, et al* (2013). Increases in brain white matter abnormalities and subcortical gray matter are linked to CD4 recovery in HIV infection*. J Neurovirol* **19**(4): 393-401.

Gartner S (2000). HIV infection and dementia. *Science (New York, NY)* **287**(0036-8075 (Print)): 602-604.

Gendelman HE, Baldwin T, Baca-Regen L, Swindells S, Loomis L, Skurkovich S (1994). Regulation of HIV1 replication by interferon alpha: from laboratory bench to bedside. *Research in immunology* **145**(8-9): 679-684; discussion 684-675.

Grieve SM, Korgaonkar MS, Koslow SH, Gordon E, Williams LM (2013). Widespread reductions in gray matter volume in depression. *NeuroImage Clinical* **3**: 332-339.

Groenewold NA, Opmeer EM, de Jonge P, Aleman A, Costafreda SG (2013). Emotional valence modulates brain functional abnormalities in depression: evidence from a meta-analysis of fMRI studies. *Neuroscience and biobehavioral reviews* **37**(2): 152-163.

Harezlak J, Buchthal S, Taylor M, Schifitto G, Zhong J, Daar E*, et al* (2011). Persistence of HIV-associated cognitive impairment, inflammation, and neuronal injury in era of highly active antiretroviral treatment. *AIDS* **25**(1473-5571 (Electronic)): 625-633.

Hong S, Banks WA (2015). Role of the immune system in HIV-associated neuroinflammation and neurocognitive implications. *Brain, behavior, and immunity* **45**: 1-12.

Husain MM, Rush AJ, Fink M, Knapp R, Petrides G, Rummans T*, et al* (2004). Speed of response and remission in major depressive disorder with acute electroconvulsive therapy (ECT): a Consortium for Research in ECT (CORE) report. *The Journal of clinical psychiatry* **65**(4): 485-491.

Jernigan TL, Archibald SL, Fennema-Notestine C, Taylor MJ, Theilmann RJ, Julaton MD*, et al* (2011). Clinical factors related to brain structure in HIV: the CHARTER study. *J Neurovirol* **17**(3): 248-257.

Joshi SH, Espinoza RT, Pirnia T, Shi J, Wang Y, Ayers B*, et al* (2015). Structural Plasticity of the Hippocampus and Amygdala Induced by Electroconvulsive Therapy in Major Depression. *Biological psychiatry*.

Kallianpur KJ, Shikuma C, Kirk GR, Shiramizu B, Valcour V, Chow D*, et al* (2013). Peripheral blood HIV DNA is associated with atrophy of cerebellar and subcortical gray matter. *Neurology* **80**(19): 1792-1799.

Kellner CH, Greenberg RM, Murrough JW, Bryson EO, Briggs MC, Pasculli RM (2012). ECT in treatment-resistant depression. *Am J Psychiatry* **169**(12): 1238-1244.

Kessler RC, Berglund P, Demler O, et al. (2003). The epidemiology of major depressive disorder: Results from the national comorbidity survey replication. *JAMA* **289**(23): 3095-3105.

Kho KH, van Vreeswijk MF, Simpson S, Zwinderman AH (2003). A meta-analysis of electroconvulsive therapy efficacy in depression. *J ect* **19**(3): 139-147.

Kim WK, Corey S, Alvarez X, Williams K (2003). Monocyte/macrophage traffic in HIV and SIV encephalitis. *Journal of leukocyte biology* **74**(5): 650-656.

Koenig S, Gendelman HE, Orenstein JM, Dal Canto MC, Pezeshkpour GH, Yungbluth M*, et al* (1986). Detection of AIDS virus in macrophages in brain tissue from AIDS patients with encephalopathy. *Science (New York, NY)* **233**(4768): 1089-1093.

Langford D, Masliah E (2001). Crosstalk between components of the blood brain barrier and cells of the CNS in microglial activation in AIDS. *Brain pathology (Zurich, Switzerland)* **11**(3): 306-312.

Li Y, Li H, Gao Q, Yuan D, Zhao J (2014). Structural gray matter change early in male patients with HIV. *International journal of clinical and experimental medicine* **7**(10): 3362-3369.

Liu X, Hairston J, Schrier M, Fan J (2011). Common and distinct networks underlying reward valence and processing stages: a meta-analysis of functional neuroimaging studies. *Neuroscience and biobehavioral reviews* **35**(5): 1219-1236.

Lorenzetti V, Allen NB, Fornito A, Yucel M (2009). Structural brain abnormalities in major depressive disorder: A selective review of recent MRI studies. *Journal of affective disorders* **117**(1-2): 1-17.

Martin SC, Wolters PL, Toledo-Tamula MA, Zeichner SL, Hazra R, Civitello L (2006). Cognitive functioning in school-aged children with vertically acquired HIV infection being treated with highly active antiretroviral therapy (HAART). *Developmental neuropsychology* **30**(2): 633-657.

Nachman S, Chernoff M, Williams P, Hodge J, Heston J, Gadow KD (2012). Human immunodeficiency virus disease severity, psychiatric symptoms, and functional outcomes in perinatally infected youth. *Archives of pediatrics & adolescent medicine* **166**(6): 528-535.

Phillips ML, Drevets WC, Rauch SL, Lane R (2003). Neurobiology of emotion perception II: Implications for major psychiatric disorders. *Biological psychiatry* **54**(5): 515-528.

Ragin AB, Wu Y, Gao Y, Keating S, Du H, Sammet C*, et al* (2015). Brain alterations within the first 100 days of HIV infection. *Annals of clinical and translational neurology* **2**(1): 12-21.

Schmaal L, Hibar DP, Samann PG, Hall GB, Baune BT, Jahanshad N*, et al* (2016). Cortical abnormalities in adults and adolescents with major depression based on brain scans from 20 cohorts worldwide in the ENIGMA Major Depressive Disorder Working Group. *Molecular psychiatry*.

Schmaal L, Veltman DJ, van Erp TG, Samann PG, Frodl T, Jahanshad N*, et al* (2015). Subcortical brain alterations in major depressive disorder: findings from the ENIGMA Major Depressive Disorder working group. *Mol Psychiatry*.

Smith R, Chernoff M, Williams PL, Malee KM, Sirois PA, Kammerer B*, et al* (2012). Impact of HIV severity on cognitive and adaptive functioning during childhood and adolescence. *Pediatr Infect Dis J* **31**(6): 592-598.

Thompson PM, Dutton RA, Hayashi KM, Toga AW, Lopez OL, Aizenstein HJ*, et al* (2005). Thinning of the cerebral cortex visualized in HIV/AIDS reflects CD4+ T lymphocyte decline.

Proceedings of the National Academy of Sciences of the United States of America **102**(0027-8424 (Print)): 15647-15652.

Towgood KJ, Pitkanen M, Kulasegaram R, Fradera A, Kumar A, Soni S*, et al* (2012). Mapping the brain in younger and older asymptomatic HIV-1 men: frontal volume changes in the absence of other cortical or diffusion tensor abnormalities. *Cortex* **48**(1973-8102 (Electronic)): 230-241.

Wade BS, Valcour VG, Wendelken-Riegelhaupt L, Esmaeili-Firidouni P, Joshi SH, Gutman BA*, et al* (2015). Mapping abnormal subcortical brain morphometry in an elderly HIV + cohort. *NeuroImage Clinical* **9**: 564-573.

Weissman MM, Bland RC, Canino GJ, et al. (1996). CRoss-national epidemiology of major depression and bipolar disorder. *JAMA* **276**(4): 293-299.

Wilson TW, Heinrichs-Graham E, Becker KM, Aloi J, Robertson KR, Sandkovsky U*, et al* (2015). Multimodal neuroimaging evidence of alterations in cortical structure and function in HIV-infected older adults. *Human brain mapping* **36**(3): 897-910.

Wood SM, Shah SS, Steenhoff AP, Rutstein RM (2009). The impact of AIDS diagnoses on long-term neurocognitive and psychiatric outcomes of surviving adolescents with perinatally acquired HIV. *Aids* **23**(14): 1859-1865.

Zahr NM, Mayer D, Rohlfing T, Sullivan EV, Pfefferbaum A (2014). Imaging neuroinflammation? A perspective from MR spectroscopy. *Brain pathology (Zurich, Switzerland)* **24**(6): 654-664.

Ances BM, Ortega M, Vaida F, Heaps J, Paul R (2012). Independent effects of HIV, aging, and HAART on brain volumetric measures. *Journal of Acquired Immune Deficiency Syndromes* **59**(1944-7884 (Electronic)): 469-477.

Becker JT, Maruca V, Kingsley LA, J.M. S, Alger JR, Barker PB*, et al* (2012). Factors affecting brain structure in men with HIV disease in the post-HAART era. *Neuroradiology* **54**(1432-1920 (Electronic)): 113-121.

Campbell S, Marriott M, Nahmias C, MacQueen GM (2004). Lower hippocampal volume in patients suffering from depression: a meta-analysis. *Am J Psychiatry* **161**(4): 598-607.

Chang L, Lee PL, Yiannoutsos CT, Ernst T, C.M. M, Richards T*, et al* (2004). A multicenter in vivo proton-MRS study of HIV-associated dementia and its relationship to age. *NeuroImage* **23**(1053-8119 (Print)): 1336-1347.

Chen Y, An H, Zhu H, Stone T, Smith JK, Hall C*, et al* (2009). White matter abnormalities revealed by diffusion tensor imaging in non-demented and demented HIV+ patients. *NeuroImage* **47**(1095-9572 (Electronic)): 1154-1162.

Drevets WC, Price Jl Fau - Furey ML, Furey ML (2008). Brain structural and functional abnormalities in mood disorders: implications for neurocircuitry models of depression. (1863-2653 (Print)).

Du MY, Wu QZ, Yue Q, Li J, Liao Y, Kuang WH*, et al* (2012). Voxelwise meta-analysis of gray matter reduction in major depressive disorder. *Progress in neuro-psychopharmacology & biological psychiatry* **36**(1): 11-16.

Epstein LG, Gelbard HA (1999). HIV-1-induced neuronal injury in the developing brain. *Journal of leukocyte biology* **65**(4): 453-457.

Fennema-Notestine C, Ellis RJ, Archibald SL, Jernigan TL, Letendre SL, Notestine RJ*, et al* (2013). Increases in brain white matter abnormalities and subcortical gray matter are linked to CD4 recovery in HIV infection. *J Neurovirol* **19**(4): 393-401.

Gartner S (2000). HIV infection and dementia. *Science (New York, NY)* **287**(0036-8075 (Print)): 602-604.

Gendelman HE, Baldwin T, Baca-Regen L, Swindells S, Loomis L, Skurkovich S (1994). Regulation of HIV1 replication by interferon alpha: from laboratory bench to bedside. *Research in immunology* **145**(8-9): 679-684; discussion 684-675.

Grieve SM, Korgaonkar MS, Koslow SH, Gordon E, Williams LM (2013). Widespread reductions in gray matter volume in depression. *NeuroImage Clinical* **3**: 332-339.

Groenewold NA, Opmeer EM, de Jonge P, Aleman A, Costafreda SG (2013). Emotional valence modulates brain functional abnormalities in depression: evidence from a meta-analysis of fMRI studies. *Neuroscience and biobehavioral reviews* **37**(2): 152-163.

Harezlak J, Buchthal S, Taylor M, Schifitto G, Zhong J, Daar E*, et al* (2011). Persistence of HIV-associated cognitive impairment, inflammation, and neuronal injury in era of highly active antiretroviral treatment. *AIDS* **25**(1473-5571 (Electronic)): 625-633.

Hong S, Banks WA (2015). Role of the immune system in HIV-associated neuroinflammation and neurocognitive implications. *Brain, behavior, and immunity* **45**: 1-12.

Husain MM, Rush AJ, Fink M, Knapp R, Petrides G, Rummans T*, et al* (2004). Speed of response and remission in major depressive disorder with acute electroconvulsive therapy (ECT): a Consortium for Research in ECT (CORE) report. *The Journal of clinical psychiatry* **65**(4): 485-491.

Jernigan TL, Archibald SL, Fennema-Notestine C, Taylor MJ, Theilmann RJ, Julaton MD*, et al* (2011). Clinical factors related to brain structure in HIV: the CHARTER study. *J Neurovirol* **17**(3): 248-257.

Joshi SH, Espinoza RT, Pirnia T, Shi J, Wang Y, Ayers B*, et al* (2015). Structural Plasticity of the Hippocampus and Amygdala Induced by Electroconvulsive Therapy in Major Depression. *Biological psychiatry*.

Kallianpur KJ, Shikuma C, Kirk GR, Shiramizu B, Valcour V, Chow D*, et al* (2013). Peripheral blood HIV DNA is associated with atrophy of cerebellar and subcortical gray matter. *Neurology* **80**(19): 1792-1799.

Kellner CH, Greenberg RM, Murrough JW, Bryson EO, Briggs MC, Pasculli RM (2012). ECT in treatment-resistant depression. *Am J Psychiatry* **169**(12): 1238-1244.

Kessler RC, Berglund P, Demler O, et al. (2003). The epidemiology of major depressive disorder: Results from the national comorbidity survey replication. *JAMA* **289**(23): 3095-3105.

Kho KH, van Vreeswijk MF, Simpson S, Zwinderman AH (2003). A meta-analysis of electroconvulsive therapy efficacy in depression. *J ect* **19**(3): 139-147.

Kim WK, Corey S, Alvarez X, Williams K (2003). Monocyte/macrophage traffic in HIV and SIV encephalitis. *Journal of leukocyte biology* **74**(5): 650-656.

Koenig S, Gendelman HE, Orenstein JM, Dal Canto MC, Pezeshkpour GH, Yungbluth M*, et al* (1986). Detection of AIDS virus in macrophages in brain tissue from AIDS patients with encephalopathy. *Science (New York, NY)* **233**(4768): 1089-1093.

Langford D, Masliah E (2001). Crosstalk between components of the blood brain barrier and cells of the CNS in microglial activation in AIDS. *Brain pathology (Zurich, Switzerland)* **11**(3): 306-312.

Li Y, Li H, Gao Q, Yuan D, Zhao J (2014). Structural gray matter change early in male patients with HIV. *International journal of clinical and experimental medicine* **7**(10): 3362-3369.

Liu X, Hairston J, Schrier M, Fan J (2011). Common and distinct networks underlying reward valence and processing stages: a meta-analysis of functional neuroimaging studies. *Neuroscience and biobehavioral reviews* **35**(5): 1219-1236.

Lorenzetti V, Allen NB, Fornito A, Yucel M (2009). Structural brain abnormalities in major depressive disorder: A selective review of recent MRI studies. *Journal of affective disorders* **117**(1-2): 1-17.

Martin SC, Wolters PL, Toledo-Tamula MA, Zeichner SL, Hazra R, Civitello L (2006). Cognitive functioning in school-aged children with vertically acquired HIV infection being treated with highly active antiretroviral therapy (HAART). *Developmental neuropsychology* **30**(2): 633-657.

Nachman S, Chernoff M, Williams P, Hodge J, Heston J, Gadow KD (2012). Human immunodeficiency virus disease severity, psychiatric symptoms, and functional outcomes in perinatally infected youth. *Archives of pediatrics & adolescent medicine* **166**(6): 528-535.

Nasi M, Pinti M, De Biasi S, Gibellini L, Ferraro D, Mussini C*, et al* (2014). Aging with HIV infection: A journey to the center of inflammAIDS, immunosenescence and neuroHIV. *Immunology Letters* **162**(1, Part B): 329-333.

Phillips ML, Drevets WC, Rauch SL, Lane R (2003). Neurobiology of emotion perception II: Implications for major psychiatric disorders. *Biological psychiatry* **54**(5): 515-528.

Ragin AB, Wu Y, Gao Y, Keating S, Du H, Sammet C*, et al* (2015). Brain alterations within the first 100 days of HIV infection. *Annals of clinical and translational neurology* **2**(1): 12-21.

Schmaal L, Hibar DP, Samann PG, Hall GB, Baune BT, Jahanshad N*, et al* (2016). Cortical abnormalities in adults and adolescents with major depression based on brain scans from 20 cohorts worldwide in the ENIGMA Major Depressive Disorder Working Group. *Molecular psychiatry*.

Schmaal L, Veltman DJ, van Erp TG, Samann PG, Frodl T, Jahanshad N*, et al* (2015). Subcortical brain alterations in major depressive disorder: findings from the ENIGMA Major Depressive Disorder working group. *Mol Psychiatry*.

Smith R, Chernoff M, Williams PL, Malee KM, Sirois PA, Kammerer B*, et al* (2012). Impact of HIV severity on cognitive and adaptive functioning during childhood and adolescence. *Pediatr Infect Dis J* **31**(6): 592-598.

Thompson PM, Dutton RA, Hayashi KM, Toga AW, Lopez OL, Aizenstein HJ*, et al* (2005). Thinning of the cerebral cortex visualized in HIV/AIDS reflects CD4+ T lymphocyte decline. *Proceedings of the National Academy of Sciences of the United States of America* **102**(0027-8424 (Print)): 15647-15652.

Towgood KJ, Pitkanen M, Kulasegaram R, Fradera A, Kumar A, Soni S*, et al* (2012). Mapping the brain in younger and older asymptomatic HIV-1 men: frontal volume changes in the absence of other cortical or diffusion tensor abnormalities. *Cortex* **48**(1973-8102 (Electronic)): 230-241.

Wade BS, Valcour VG, Wendelken-Riegelhaupt L, Esmaeili-Firidouni P, Joshi SH, Gutman BA*, et al* (2015). Mapping abnormal subcortical brain morphometry in an elderly HIV + cohort. *NeuroImage Clinical* **9**: 564-573.

Weissman MM, Bland RC, Canino GJ, et al. (1996). CRoss-national epidemiology of major depression and bipolar disorder. *JAMA* **276**(4): 293-299.

Wilson TW, Heinrichs-Graham E, Becker KM, Aloi J, Robertson KR, Sandkovsky U*, et al* (2015). Multimodal neuroimaging evidence of alterations in cortical structure and function in HIV-infected older adults. *Human brain mapping* **36**(3): 897-910.

Wood SM, Shah SS, Steenhoff AP, Rutstein RM (2009). The impact of AIDS diagnoses on long-term neurocognitive and psychiatric outcomes of surviving adolescents with perinatally acquired HIV. *Aids* **23**(14): 1859-1865.

Zahr NM, Mayer D, Rohlfing T, Sullivan EV, Pfefferbaum A (2014). Imaging neuroinflammation? A perspective from MR spectroscopy. *Brain pathology (Zurich, Switzerland)* **24**(6): 654-664.

Chapter 2: Machine Learning on High Dimensional Shape Data from Subcortical Brain Surfaces: A Comparison of Feature Selection and Classification Methods[1]

High-dimensional shape descriptors (HDSD) are useful for modeling subcortical brain surface morphometry. Though HDSD is a useful basis for disease biomarkers, its high dimensionality requires careful treatment in its application to machine learning to mitigate the curse of dimensionality. We explored the use of HDSD feature sets by comparing the performance of two feature selection approaches, Regularized Random Forest (RRF) and LASSO, to no feature selection (NFS). Each feature set was applied to three classifiers: Random Forest (RF), Support Vector Machines (SVM) and Naïve Bayes (NB). Paired feature-selection-classifier approaches were 10-fold cross-validated on two diagnostic contrasts: Alzheimer's disease and mild cognitive impairment, both relative to controls across varying sample sizes to evaluate their robustness. LASSO aided classification efficiency, however, RRF and NFS afforded more robust performances. Performance varied considerably by classifier with RF being most stable. We advise careful consideration of performance-efficiency tradeoffs in choosing feature selection strategies for HDSD.

Introduction

Disorders that affect the central nervous system are often characterized by patterns of abnormal brain morphometry in regions involved with the disorder. To the extent that a disorder presents with stereotyped patterns of abnormal brain morphometry, these patterns can be used as

[1] The content of this chapter has been published as Wade BSC, Joshi SH, Gutman BA, Thompson PM. Machine learning on high dimensional shape data from subcortical brain surfaces: A comparison of feature selection and classification methods. *Pattern Recognition*. Available at: http://dx.doi.org/10.1016/j.patcog.2016.09.034

biomarkers for the classification of the disorder as well as the monitoring of its progression. Recent advances in biomedical imaging and pattern detection have increased the interest in developing computer assisted diagnostic systems to aid in the detection of neurological disorders based on features derived from structural brain magnetic resonance imaging (MRI).

Historically, studies describing brain morphometry have focused principally on the use of volumetric descriptions of regions of interest (ROIs). While volumetric descriptions confer the advantage of being relatively computationally non-intensive and simple to interpret they also only capture comparatively little information about the morphometry of the actual structure. Recently, it has become increasingly popular to include local shape-based descriptions of brain regions to compliment volumetric measures (Joshi *et al*, 2016; Wade *et al*, 2016; Wade *et al*, 2015b). Shape analysis is most commonly used for registering individual subcortical anatomies to a given template. The template itself could either be created using unbiased registration of individual shapes or by choosing a characteristic anatomical shape from the population. The registration step is followed by statistical analysis, which localizes differences in the geometric shape features at the population level. Different representations of shapes and surfaces give rise to diverse geometric features. While several classes of shape analysis exist including tensor-based morphometry (Ashburner *et al*, 1998) and Laplace-Beltrami spectral analysis (Reuter *et al*, 2009a) we explore the use of shape features defined vertex wise on the surface of subcortical brain regions.

While high-dimensional shape descriptors (HDSD) may offer more information about brain morphometry than simple volumetric descriptions, classification using high-dimensional neuroimaging feature sets is likely to be plagued by the curse of dimensionality. A handful of studies have investigated whether feature selection will boost the performance of classifiers

using high-dimensional neuroimaging feature sets with some reporting significant improvement (Liu *et al*, 2013) and others reporting only marginal to no gains (Casanova *et al*, 2012). Our contribution in this paper is a systematic evaluation of the gains in the performance of a variety of commonly used classifiers afforded by the use of feature selection processes. Specifically, we compare the efficacy of several joint feature selection and classification methods to handle HDSD as a biomarker for brain disorders. We assess each approach using 10-fold cross-validation on two diagnostic contrasts: Alzheimer's disease (AD) versus normal controls (NC) and mild cognitive impairment (MCI) versus NC. Classification of each contrast was based on two separate classes of HDSD: 1) the radial distance (RD), a proxy for the structure's local thickness and 2) the log of the Jacobian determinant (JD), a measure of local surface area expansion or contraction. In order to evaluate the possibility that the performances of these approaches vary as a function of the ratio of the sample size to feature set dimensionality, we additionally report the performances of each approach based on reduced sample sizes of 50% and 25% of the full cohort.

Although dimensionality reduction methods such as principal components analysis, manifold learning and locally linear embedding are powerful methods to reduce the dimensionality of a feature set, they all produce transformations of the original data set. Feature selection methods are normally distinguished from dimensionality reduction methods in that they preserve the original set of features. This is a very desirable property especially in the context of identifying subsets of data in clinical and biological frameworks where the original data point is itself meaningful and transformations could obscure the meaning of the selected feature set. In that spirit we also specifically evaluate the use of the RD and JD descriptors as they capture intuitive properties of a structure's morphometry: deformations in its thickness and surface area

at highly focal regions of the surface. This intuitive interpretation of these descriptors also makes their clinical implications easier to interpret. The joint use of RD and JD is generally beneficial as each captures complementary aspects of a structure's topology. Exploring both descriptors in this study allows us to evaluate the performance of these joint classification approaches across separate descriptors to improve the generalizability of our findings. Our group has previously applied these descriptors to map subcortical morphometry in patients with depression (Wade *et al*, 2016; Wade *et al*, 2015a), mild traumatic brain injury (Tate *et al*, 2016) and HIV (Wade *et al*, 2015b). Numerous other shape descriptors, mentioned previously, have also been successfully applied to map abnormal patterns of brain morphometry in a variety of diseases such as frontotemporal dementia (Macfarlane *et al*, 2015), schizotypal personality disorder (Reuter *et al*, 2009b), Huntington's disease (Faria *et al*, 2016) and many others. However, comparing the performances of these descriptors is beyond the scope of our current paper.

We specifically evaluate two feature selection methods, the regularized random forest (RRF) and the LASSO. The RRF framework is a recently developed extension of the random forest framework to incorporate feature selection and has previously been applied to classifying transactions on the financial market (Endler, 2014), identifying highly informative single nucleotide polymorphisms in genome wide association studies (Nguyen *et al*, 2015), human activity recognition (Uddin and Uddiny, 2015) and brain image classification (Wade *et al*, 2015a), has been shown to improve the performance of random forest classifiers in certain cases (Deng and Runger, 2012; Deng and Runger, 2013a). Meanwhile, the LASSO framework (Tibshirani, 1994, 2011) has been widely applied as a sparse feature selection method in a wide variety of studies and has gained widespread popularity in the neuroimaging literature (Bunea *et al*, 2011; Toiviainen *et al*).

The no free lunch theorem (Wolpert and Macready, 1997) tells us that no single method would be universally optimal across all classification problems, even when limiting our scope to diagnostic classification problems involving neuroimaging data. As such, we are simply setting out to develop heuristics, not rules, for the treatment of this form of HDSD as a feature set in the classification of neurological disorders.

Methods

Subjects

We analyzed AD, MCI and matched NC participants that underwent 1.5T T1-weighted structural brain MRI scans (MPRAGE, repetition time/echo time = 2400/1000 ms, flip angle = 8°, slice thickness = 1.2 mm, final voxel resolution = 0.9375 x 0.9375 x 1.2 mm^3) as part of phase 1 of the Alzheimer's Disease Neuroimaging Initiative (ADNI-1). Our sample included N=143 AD, N=337 MCI and N=202 NC participants scanned at one-year follow-up.

ADNI was launched in 2004 by the National Institutes of Health, the Food and Drug Administration, private pharmaceutical companies, and nonprofit organizations to identify and evaluate biomarkers of AD for use in multisite studies. All ADNI data are publicly available at adni.loni.usc.edu. All ADNI studies are conducted in compliance with the Good Clinical Practice guidelines, the Declaration of Helsinki, and the US 21 CFR Part 50 - Protection of Human Subjects, and Part 56 - Institutional Review Boards. Written informed consent was obtained from all ADNI participants before the study. ADNI is a multisite longitudinal study of patients with AD, MCI, and healthy older adult control.

High dimensional shape features

Previously validated FreeSurfer workflows, including non-brain tissue removal, intensity normalization and automated volumetric parcellation based on probabilistic information from

manually labeled training sets, were used to segment the bilateral thalamus, putamen, pallidum, amygdala, accumbens, caudate and hippocampus from the raw brain MRIs. Each segmented volume was visually inspected to ensure its quality.

A parameterization of each surface was obtained using the Medial Demons method detailed in (Gutman *et al*, 2015; Gutman *et al*, 2012). In short, all surfaces were conformally mapped to the spherical domain. The spherical maps were rigidly rotated to a probabilistic atlas. Next, the Spherical Demons (SD) (Gutman *et al*, 2013) algorithm was used to non-linearly register the spherical maps on the basis of curvature. Two surface-based functions were defined at this stage: first, the global orientation function, defining the direction of the surface and, secondly, the local thickness of the surface with respect to a skeletonized medial core. Finally, SD was redone using both the newly defined medial core in combination with surface curvature to match each surface to the atlas.

From this process, shape features are defined at each vertex: 1) radial distance (RD), a proxy for thickness and 2) the log of the Jacobian determinant (JD) which indicates local surface area dilation or contraction. Among all 14 subcortical surfaces, there were a total of 27,120 vertices; the RD and JD were defined at each.

Feature selection

Classification using high-dimensional feature sets is often aided by feature selection. This is done to mitigate the curse of dimensionality in which data sparsity scales exponentially with its dimensionality as well as limit the potential for overfitting to training data. Feature selection is commonly distinguished from dimensionality reduction methods in that the former retains original values of features considered important by a given criterion while dimensionality reduction most often seeks to represent the original features by linear combinations of their

original values in a lower subspace. We implemented two feature selection algorithms: 1) the regularized random forest (RRF) (Deng *et al*, 2012) and 2) the least absolute shrinkage and selection operator (LASSO) (Tibshirani, 1994). We then compared the performance of classifiers using these subsets to classifiers using the full set of features. Feature selection was performed independently on RD and JD sets in order to evaluate the generalizability of differential performances across a variety of shape descriptors.

Regularized random forest feature selection

Random forests (RF) (Breiman, 2001) are a type of supervised classifier constructed from an ensemble of classification and regression trees (CART) that use the majority vote of its constituent terminal nodes to predict the class of a given observation. Each CART is normally provided a bootstrapped sample of 63% of the observations along with a random subset of $\sqrt{m}$ features at each node, where *m* is the number of features.

RRF is an extension of the standard RF framework to facilitate feature selection. The nodes within a standard RF are split by identifying the feature, X_i, that maximizes the gain in the Gini impurity index. The Gini index is calculated for each feature at the present node, v. Gini(v) is given by,

$$\mathrm{Gini(v)} = \sum_{\mathrm{C}=1}^{\mathrm{C}} \hat{\mathrm{p}}_{\mathrm{c}}^{\mathrm{v}} \left(1 - \hat{\mathrm{p}}_{\mathrm{c}}^{\mathrm{v}}\right) \qquad (1)$$

where $\hat{p}_c^v$ is the proportion of observations belonging to class C at node v. The RF algorithm aims to split each CART node by the feature X_i which maximizes the class purity of the resultant child nodes. RRF differs from the standard RF framework in that $\mathrm{Gain(X_i)}$ is penalized by degree λ_i if $\mathrm{X_i}$ has not been used to split a previous node in the tree. That is,

$$\text{Gain}(\text{X}_\text{i}) = \begin{cases} \text{Gain}(\text{X}_\text{i}, v) & \in F \\ \lambda_i \cdot \text{Gain}(\text{X}_\text{i}, v) & \notin F \end{cases} \quad (2)$$

Where F is the set of variables used to split the CART's nodes. λ_i is given by $\lambda_i = (1-\gamma) + \gamma Imp_i'$ where $\gamma \in [0,1]$ and Imp_i' is the normalized importance score associated with feature X_i.

With penalty λ_i a variable not in F is less likely to be used to split the current node. In the RRF framework, feature selection is done by retaining all features in set F. $\gamma = 0$ is the least penalized approach however in order for X_i to be included in set F, it must still be more informative to the partitioning of the feature space than all variables currently in F (Deng and Runger, 2013b). A value for γ was selected using cross validation, outlined subsequently in the section *parameterization of feature selection methods*.

LASSO feature selection

The LASSO is a well-known procedure used to regularize the coefficients, β_j, of a linear regression model subject to an l_1-penalty. Provided a set of standardized features x_{ij} along with centered outcomes, y_i, for i in [1, N], where N is the number of observations, and j in [1, p], where p is the number of features, the LASSO seeks to minimize,

$$\sum_{\text{i}=1}^{\text{N}} (\text{y}_\text{i} - \sum_{\text{j}} \text{x}_{\text{ij}}\beta_\text{j})^2 + \lambda \sum_{\text{j}=1}^{\text{p}} |\beta_\text{j}| \ . \quad (3)$$

This process is the same as minimizing the sum of squares with the added constraint of $\sum|\beta_j| \leq s$. Due to the l_1-penalty, LASSO has the desirable quality of setting the coefficients of unimportant or redundant features to zero. This provides a natural framework for feature selection in which models are constructed using only features with non-zero coefficients. For our purposes the constraint, *s*, was determined empirically using 10-fold cross-validation on the

training data; the *s* affording the minimal cross-validation error was chosen. λ is the shrinkage parameter controlling the degree of coefficient shrinkage. $\lambda(0)$ results in no shrinkage while $\lambda >$ 0 results in increasingly stringent coefficient shrinkage. The shrinkage parameter value was also selected using 10-fold cross validation where the value resulting in the minimum mean cross validation error was selected. Tuning was performed using the glmnet package in R (Friedman *et al*, 2010).

Classifiers

Each of the three feature sets, RRF, LASSO and NFS was used as an input into each of three widely used classifiers. We briefly outline the attributes of the classifiers here.

Random forest

The general RF framework is given previously in the section *regularized random forest feature selection*. The RF classifier used here was composed of 1000 trees, with a minimum leaf node sample requirement of 1. Each weak learner (for CART) was grown to its maximum, unpruned, size and provided a bootstrapped sample of 63% of the observations along with a random subset of $\sqrt{m}$ features, where *m* is the number of features, which are all standard parameterizations of random forests. This parameterization was the same for the RRF framework.

Support vector machines

We implemented an SVM with a radial basis kernel function where the optimal hyperplane is found by,

$$\underset{w}{\operatorname{argmin}}\left(\frac{1}{2}w^t w + C\sum_{i=1}^{N}\xi_i\right) \quad (4)$$

subject to $y_i(w^t\,\phi(x_i)+b) \geq 1-\,\xi_i$ and $\xi_i\,\geq 0, i=1,\ldots,N$ where C is the cost factor that penalizes misclassifications in training examples, w is a vector of coefficients, b is the constant intercept term, ξ_i controls the allowable (functional) margins on either side of the hyperplane, and ϕ is a radial basis kernel. Use of the radial kernel yielded a significantly higher accuracy than a linear SVM. Optimal cost and γ parameters were obtained through cross validation.

Naïve Bayes

The foundation of the NB classifier is Bayes rule which assumes conditional independence of the constituent features of X, $[X_1, X_2,\ldots,X_n]$, with respect to each other given the outcome, Y ∈ [0,1]. With a set of continuous predictive features a Gaussian NB framework is used in which the class probability estimate is,

$$P(Y=1|X) = \frac{1}{1+\exp\left(w_{0+\sum_{i=1}^{n} w_i X_i}\right)} \qquad (5)$$

where w_i in $w_1 \ldots w_n$ are weightings given by, $w_i = \frac{\mu_{i0}-\mu_{i1}}{\sigma_i^2}$ and

$$w_0 = \ln\frac{P(Y=0)}{P(Y=1)} + \sum_i \frac{\mu_{i1}^2-\mu_{i0}^2}{2\sigma_i^2}$$

where $\mu_i\ and\ \sigma_i$ are the mean and standard deviation of feature X_i.

Parameterization of feature selection methods

We performed cross validation across a range of parameters to identify optimal parameters for the feature selection methods, RRF and LASSO. A parameterization was considered optimal if it yielded the both the largest AUC and its runtime was not prohibitively long on a 2 GHz Intel Core i7 with 8Gb of RAM.

The RRF required optimization of both γ and the number of trees within each forest. We considered a range of γ [0,1] in steps of 0.2. The LASSO is actually a special case of the more general elastic net (Zou and Hastie, 2005). The elastic net seeks to minimize the sum of squared errors subject to an interpolation between l_1 and l_2-penalties; that is,

$$\min_{\beta} \|y - X\beta\|^2 \; s.t. \; \lambda P_{\propto}(\beta) \tag{6}$$

where,

$$P_{\propto}(\beta) = \frac{(1-\alpha)}{2}\|\beta\|_2^2 + \alpha\|\beta\|_1 = \sum_{j=1}^{P}\left(\frac{(1-\alpha)}{2}\beta_j^2 + \alpha|\beta_j|\right)$$

and α is the mixing parameter between the two penalties: $\alpha(0)$ yields the ridge penalty while $\alpha(1)$ provides the LASSO. We performed cross validation on a range of alpha values between α = [0,1] in steps of 0.2. λ is again the shrinkage parameter controlling the magnitude of coefficient shrinkage described in the section *LASSO feature selection*.

Influence of sample size

The ratio of sample size to feature set dimensionality lies at the heart of the curse of dimensionality. This suggests that it is important to evaluate the performance of these approaches across varying ratios of sample and feature set sizes. To accomplish this we repeated each analysis on randomly selected subsets of 50% and 25% of each group's original sample size. At 50%, there were N=71 AD, N= 168 MCI and N=101 NC. At 25% there were N= 35 AD, N= 84 MCI and N=50 NC.

Results

Feature selection parameters

We selected optimal feature selection parameters based on their performance in classifying AD versus NC based on RD features using 10-fold cross validation. AUC varied moderately by γ value though not to a statistically significant degree. Runtime increased with increasing γ value, however, also not to a substantial degree. For our purposes we used $\gamma(0)$. AUC did not vary predictably with tree number in the RRF framework, however both runtime and the number of retained features increased substantially with an increased number of trees. Throughout this study we used 1000 trees for both RRF and standard random forest models. RRF CARTs were also grown to their full depth, and each received a bootstrapped sample of 63% of the observations along with a random subset of $\sqrt{m}$ features with a minimum leaf sample size of N=1. In the parameterization of the elastic net we did not observe an association between AUC and alpha. However, $\alpha(0)$ (i.e. ridge penalization) was substantially more time consuming than any other parameterization. $0 < \alpha \leq 1$ yielded nearly identical runtimes with LASSO being somewhat faster than the others. Due to its speed and widespread use we opted to use $\alpha(1)$, i.e. the LASSO, throughout. **Figure 2-1** plots the average AUC and runtimes across various parameterizations of feature selection methods as well as total runtimes for each paired feature selection and classification approach across 10 folds using RD measures to classify AD versus NC using the full set of subjects. Notably, total runtime for RRF-based methods was dramatically higher at > 2.5 hours than NFS methods (> 0.5 hours) and LASSO methods (< 5 minutes).

Feature selection subsets

Supplementary figure **2-S1** plots the percentage of features retained by the RRF and LASSO methods under each diagnostic contrast and sample size. Several differences are shown between the two methods. First, the LASSO selected a far sparser subset of features than the RRF, retaining upwards of about 0.9% of features on any given surface at most. Additionally, the LASSO selected features from only a subset of surfaces, excluding features from the caudate, pallidum and putamen in several instances. On average the ratios of features retained across surfaces did not vary to a large degree under varying sample sizes however the absolute percentage of retained features declined somewhat steadily in relation to smaller sample sizes. In contrast, the RRF selected upwards of about 18% of features from any given surface and retained features from each surface. Again, patterns of features retained across each structure were consistent for RRF under reduced sample sizes. Feature selection varied by diagnosis as well with the RRF retaining more features, on average, for the MCI contrast than the AD contrast. However, the LASSO was reversed here retaining more features for AD than MCI on average. Supplementary figures **2-S2** and **2-S3** map the selected regions for the LASSO and RRF, respectively, for the full set of participants. Supplementary figure **2-S4** maps the importance scores from the RRF framework to the subcortical surfaces, illustrating the relative influence of each region in the diagnostic classifications.

Classification results

Figure 2-2 plots receiver operating characteristic (ROC) curves for each diagnostic contrast grouped by shape feature under given sample sizes; a separate curve is given for each feature-selection-method-classifier combination in the upper triangle of each plot. The lower triangles within each plot provide pairwise results of DeLong's (DeLong *et al*, 1988) for differences in area under the curve (AUC). Black intersections indicate a significant difference in

AUC between the two approaches being compared; green arrows within each significant intersection point to the name of the approach with the larger AUC. Several pairwise comparisons remained significantly different following false discovery rate (FDR) correction for multiple comparisons revealing a number of important trends. Here we simply applied FDR within each unique set of shape metrics within the set of diagnostic contrasts; that is, within each matrix.

At the full sample size and holding feature selection method equal, NB-based classifiers regularly underperformed relative to RF and SVM-based methods under both diagnostic contrasts. In the classification of MCI using JD-based NFS, SVM outperformed RF. Beyond this, however, SVM and RF were highly comparable. Holding classifiers equal to compare feature selection approaches several other trends emerge. Among the NB-based classifiers the RRF outperformed NFS on three out of four comparisons. In two cases SVM-LASSO was outperformed by SVM-NFS and once by SVM-RRF. Table 2-1 provides exact AUC values.

Sample size reduction highlighted further differential performances of these approaches. At 50% of the original sample size, NB-based methods began to have more competitive performances with RF and SVM methods. Only NB-NFS was consistently outperformed by SVM methods in the classification of MCI using JD features. NB-RRF outperformed the SVM-LASSO in the classification of MCI using RD features, however, most NB methods were still outperformed by RF-based approaches. On average RF methods outperformed SVM at this reduced sample size. While most significant differences in performance were related to choice of classifier here, several differences were linked to feature selection method. NB-RRF again regularly outperformed NB-NFS and the SVM-LASSO was outperformed by SVM-RRF in the classification of MCI using RD measures.

At 25% of the original sample sizes, NB-LASSO consistently underperformed relative to RF methods in the classification of AD, however, other NB approaches were competitive with both RF and SVM. NB-NFS only underperformed relative to RF methods in the classification of MCI using RD. Interestingly, in the classification of MCI using RD, SVM methods were entirely outperformed by RF approaches. Again, the majority of differential performances were attributable to the classifiers themselves, but we again note that NB-RRF outperformed NB-NFS regularly in this context. It is also noteworthy that no significant differences were observed between approaches for the classification of MCI using JD features at 25% of observations.

Figure 2-3 plots the average AUC attributable to each (a) feature selection method averaged across each classifier and (b) classifier averaged across feature selection method. In general, we observed that RF-based methods had robust performances across variable sample sizes. SVMs appeared to be rather sensitive to sample size being widely outperformed by RFs when the samples were reduced. NB was widely outperformed by RF across sample sizes but was surprisingly competitive with SVMs at the reduced sample sizes. Among feature selection approaches, LASSO was most affected by sample size reductions while RRF and NFS appear relatively robust to reductions in sample size. Average RRF AUC appears marginally higher than NFS AUC, however, we only observed consistent differences between these two approaches in the context of NB-based approaches as noted in Figure 2-2.

Figure 2-4 illustrates the percentage of comparisons in which classifiers and feature selection methods attained a significantly higher AUC than other methods across the various sample sizes. From Figure 2-4a it is apparent that RF was robust across sample sizes while SVM performances declined with reduced sample sizes. NB was also shown to rarely attain an AUC significantly larger than SVM or RF. Figure 2-4b illustrates that both NFS and LASSO

performances declined substantially when sample size was reduced while RRF performances were somewhat more preserved when sample sizes declined. Figures 2-4(c-d) show the percentage of pairwise instances in which classifiers and feature selection methods had significantly larger AUCs than other specific approaches. Here we see notable instances of SVM outperforming RF and NB when the sample size was full but not when the sample is reduced. At reduced sample sizes, RF and NB demonstrated more widely competitive performances. At the full sample size, NFS performs well with respect to RRF and LASSO feature sets though when the sample is reduced RRF tended to yield higher AUCs than NFS. Additionally, while RRF maintained competitive AUCs across varying sample sizes LASSO declined more heavily with sample size reductions.

Discussion

Given the high degree of inherent spatial correlation within neuroimaging data, including the HDSD described here, we expected that there should be a lower 'effective dimensionality' that feature selection could leverage to the benefit of the classifier. To evaluate this we explored whether the use of feature selection would consistently boost the performance of several commonly used classifiers in the classification of both AD and MCI using nothing but HDSD defined on subcortical surfaces. Chu et al. (Chu *et al*, 2012) noted that feature selection is substantially more important in smaller sample sizes (i.e. lower sample size to feature set dimension ratio). To account for this possibility we additionally assessed the robustness of each approach to systematic sample size reductions. Prior to reducing the sample sizes we generally did not observe consistent significant improvements in classifier performance with the use of LASSO or RRF feature selection methods. SVM and RF based approaches consistently yielded higher AUC than NB while being competitive with each other. RRF feature sets demonstrated

more robustness against reductions in sample size than LASSO. NFS performance declined less rapidly than LASSO with reductions in sample size though it was not as robust as RRF. Greater differences were observed between classifiers than feature selection methods at lower sample sizes.

The relative speed of each approach was also considered. In Figure 2-1c we benchmarked each joint feature selection classifier approach across all 10 cross validation folds. Very distinctly, the RRF-based methods were highly time-consuming, requiring upwards of 3 hours to complete on a dataset of this size. Meanwhile, NFS-based approaches required less than an hour while LASSO was decidedly the fastest, requiring only several minutes to complete all folds.

We explored these patterns across two diagnostic contrasts in order to explore the generalizability of our conclusions. While AD and MCI are of course related to each other, MCI presents with a far more heterogeneous pattern of brain morphometry than AD. This is reflected by the overall higher performance attained under the AD versus NC contrast than the MCI versus NC contrast. Yet, despite the lack of homogeneity in MCI, similar patterns of performances were observed across both feature selection methods and classifiers. This suggests that these patterns of performance may generalize to other notoriously heterogeneous brain disorders such as schizophrenia and attention-deficit disorder. However, future studies are needed to confirm this.

Numerous studies have investigated classifying AD and MCI versus normally aging controls using structural neuroimaging features. For a thorough review we refer the reader to a review by Weiner (Weiner *et al*, 2012). Notably, Cuingnet et al. (Cuingnet *et al*, 2011) compared the efficacy of classifying AD and MCI versus NC using voxel-based methods, cortical thickness measures and shape and volume measures derived exclusively from the hippocampus. Their group reported voxel-based and cortical thickness approaches with specificity and sensitivities of

up to 90% and 75%, respectively, in classifying AD. Their strategies targeting the hippocampus only had reduced specificities of 63% for volume and 84% for shape-based measures with comparable sensitivities to voxel-based and cortical data. Using volumetric measures of the hippocampus and entorhinal cortex only, Fan et al. (Fan *et al*, 2008) also reported high SVM classification accuracies of AD versus NC, MCI versus NC and AD versus MCI at 82%, 72% and 58%, respectively. Chincarini et al. (Chincarini *et al*, 2011) used texture-based features of voxel intensities derived from the medial temporal lobe to distinguish AD from NC subjects with a high AUC of 97% as well as MCI-AD converters from NC (AUC = 92%). It is difficult to directly compare performances across studies due to differences in underlying samples and feature sets, we note that the approaches outlined in this study attaining AUCs of up to 91% for AD versus NC and 82% for MCI versus NC are quite competitive with other existing unimodal classifiers. There is a strong interest in classifying both MCI versus AD as well as MCI-AD converters versus non-converters. While these problems are perhaps more challenging than simply classifying AD versus NC or MCI versus NC, it is beyond the scope of our current investigation. However, we would expect similar patterns of performances to hold across these approaches for those classification problems as well.

Ultimately, the investigator seeking to choose between this set of methods would have to weigh the gains in classification performance against the computational expenses associated with each. We generally observed, for instance, that RRF yielded the most stable performances across a range of sample sizes but also required upwards of three times the amount of computational time compared to NFS approaches. LASSO-based approaches were by far the most computationally efficient but often provided lower AUC, especially at reduced sample sizes. The clear benefit of LASSO in this context is that the sparse feature sets it returns drastically boost

the subsequent classification accuracy, though at the cost of marginally lower performances relative to the more retentive RRF and NFS approaches. SVMs using LASSO subsets appeared particularly prone to underperforming relative to other methods. Because SVM decision boundaries are determined by the data points on or within its margin which is an implicit form of sparsity it is possible that they are more prone to overfitting when the provided feature set is itself sparse as is the case with LASSO. NFS seems to be a reasonable approach in this context as it offered competitive AUC values in many cases while being substantially less computationally expensive than RRF.

A particular limitation of our study is that we explored purely data-driven feature selection approaches. Two previous studies (Chu *et al*, 2012; Cuingnet *et al*, 2011) investigating classification of neuroimaging data both noted that data-driven feature selection methods, such as those employed here, failed to significantly improve classification accuracies, however, feature selection using prior knowledge of a disease's morphometry was significantly beneficial. Importantly, we have focused exclusively on the treatment of HDSD. For many diseases, AD and MCI included, the use of multimodal data has been demonstrated to be most effective in maximizing classification accuracy (Liu *et al*; Westman *et al*, 2012; Zhang and Shen). It would thus be expected that multimodal classifiers would outperform the unimodal approaches described here. However, future studies incorporating HDSD in multimodal frameworks may benefit from our findings when integrating HDSD with other modalities. A further limitation of the current study is, of course, that we only evaluated these approaches on AD and MCI cohorts. AD has a relatively homogenous profile of neurodegeneration, but MCI is more heterogeneous in its manifestations. Although we observed similar patterns of performances across both AD and MCI classification problems this does not ensure that our findings will translate to other

neurological disorders. Our findings serve as a starting point to understand the behavior of these approaches in their application to other disorders.

Overall, our results suggest that classifiers are likely to benefit from feature selection when using HDSD, but at a rather high computational expense. NFS offered somewhat competitive performances with RRF at a fraction of the computational expense. The sparsity induced by LASSO appears to underestimate the effective dimensionality for the classification of AD and MCI using this type of data, leading to the exclusion of informative data points. The gains in overall AUC derived from using RRF and NFS (which are more retentive feature selection approaches than LASSO) may reflect a lack of uninformative data that would otherwise be removed by feature selection. However, there were ultimately significant gains in computational efficiency derived from the use of the LASSO which may be beneficial in certain time-sensitive settings.

Acknowledgements

Chapter 2 is a version of Wade BSC, Joshi SH, Gutman BA, Thompson PM Machine learning on high dimensional shape data from subcortical brain surfaces: A comparison of feature selection and classification methods. (2016). *Pattern Recognition*. In Press.

Shantanu Joshi aided in the design of this study. Boris Gutman assisted in designing the study and developed the shape analytic methods described here. Paul Thompson was the study PI.

This study was funded by award number R01MH092301 from the NIMH, the NIH 'Big Data to Knowledge' (BD2K) Center of Excellence grant U54 EB020403, funded by a cross-NIH consortium including NIBIB and NCI.

References

Ashburner J, Hutton C, Frackowiak R, Johnsrude I, Price C, Friston K (1998). Identifying global anatomical differences: deformation-based morphometry. *Human brain mapping* **6**(5-6): 348-357.

Breiman L (2001). Random Forests. *Machine Learning* **45**(1): 5-32.

Bunea F, She Y, Ombao H, Gongvatana A, Devlin K, Cohen R (2011). Penalized least squares regression methods and applications to neuroimaging. *NeuroImage* **55**(4): 1519-1527.

Casanova R, Hsu FC, Espeland MA (2012). Classification of structural MRI images in Alzheimer's disease from the perspective of ill-posed problems. *PLoS One* **7**(10): e44877.

Chincarini A, Bosco P, Calvini P, Gemme G, Esposito M, Olivieri C*, et al* (2011). Local MRI analysis approach in the diagnosis of early and prodromal Alzheimer's disease. *NeuroImage* **58**(2): 469-480.

Chu C, Hsu AL, Chou KH, Bandettini P, Lin C (2012). Does feature selection improve classification accuracy? Impact of sample size and feature selection on classification using anatomical magnetic resonance images. *NeuroImage* **60**(1): 59-70.

Cuingnet R, Gerardin E, Tessieras J, Auzias G, Lehéricy S, Habert M-O*, et al* (2011). Automatic classification of patients with Alzheimer's disease from structural MRI: A comparison of ten methods using the ADNI database. *NeuroImage* **56**(2): 766-781.

DeLong ER, DeLong DM, Clarke-Pearson DL (1988). Comparing the Areas under Two or More Correlated Receiver Operating Characteristic Curves: A Nonparametric Approach. *Biometrics* **44**(3): 837-845.

Deng H, Runger G (2012). Feature Selection via Regularized Trees.

Deng H, Runger G (2013a). Gene selection with guided regularized random forest. *Pattern Recognition* **46**.

Deng H, Runger G (2013b). Gene Selection with Guided Regularized Random Forests. *Pattern Recogition* **46**: 3483-3489.

Endler A (2014). Application of Binary Classifiers to Filter Transactions on the Financial Market. *Available at SSRN 2462169*.

Fan Y, Batmanghelich N, Clark CM, Davatzikos C (2008). Spatial patterns of brain atrophy in MCI patients, identified via high-dimensional pattern classification, predict subsequent cognitive decline. *NeuroImage* **39**(4): 1731-1743.

Faria AV, Ratnanather JT, Tward DJ, Lee DS, van den Noort F, Wu D*, et al* (2016). Linking white matter and deep gray matter alterations in premanifest Huntington disease. *NeuroImage Clinical* **11**: 450-460.

Friedman J, Hastie T, Tibshirani R (2010). Regularization Paths for Generalized Linear Models via Coordinate Descent. *Journal of statistical software* **33**(1): 1-22.

Gutman B, Jahanshad N, Ching C, Wang Y, Kochunov P, Nichols T*, et al* (2015). Medial Demons Registration Localizes the Degree of Genetic Influence over Subcortical Shape Variability: An N= 1480 Meta-Analysis. *International Symposium on Biomedical Imaging*.

Gutman B, Madsen S, Toga A, Thompson P (2013). A Family of Fast Spherical Registration Algorithms for Cortical Shapes. *Multimodal Brain Image Analysis* **8159**: 246-257.

Gutman B, Wang Y, Rajagopalan P, Toga A, Thompson P (2012). Shape matching with medial curves and 1-D group-wise registration. *International Symposium on Biomedical Imaging* **9**: 716-719.

Joshi SH, Espinoza RT, Pirnia T, Shi J, Wang Y, Ayers B*, et al* (2016). Structural Plasticity of the Hippocampus and Amygdala Induced by Electroconvulsive Therapy in Major Depression. *Biological psychiatry* **79**(4): 282-292.

Liu F, Wee CY, Chen H, Shen D Inter-modality relationship constrained multi-task feature selection for AD/MCI classification.

Liu X, Tosun D, Weiner MW, Schuff N (2013). Locally linear embedding (LLE) for MRI based Alzheimer's disease classification. *NeuroImage* **83**: 148-157.

Macfarlane MD, Jakabek D, Walterfang M, Vestberg S, Velakoulis D, Wilkes FA*, et al* (2015). Striatal Atrophy in the Behavioural Variant of Frontotemporal Dementia: Correlation with Diagnosis, Negative Symptoms and Disease Severity. *PLoS One* **10**(6): e0129692.

Nguyen T-T, Huang JZ, Wu Q, Nguyen TT, Li MJ (2015). Genome-wide association data classification and SNPs selection using two-stage quality-based Random Forests. *BMC Genomics* **16**(2): 1-11.

Reuter M, Franz E, Shenton M, Niethammer M (2009a). Laplace-Beltrami Eigenvalues and Topological Features of Eigenfunctions for Statistical Shape Analysis. *Computer aided design* **41**(10): 739-755.

Reuter M, Franz E, Shenton M, Niethammer M (2009b). Laplace-Beltrami Eigenvalues and Topological Features of Eigenfunctions for Statistical Shape Analysis. *Computer aided design* **41**(10): 739-755.

Tate DF, Wade BS, Velez CS, Drennon AM, Bolzenius J, Gutman BA*, et al* (2016). Volumetric and shape analyses of subcortical structures in United States service members with mild traumatic brain injury. *Journal of neurology*.

Tibshirani R (ed) (1994). Regression Shrinkage and Selection Via the Lasso. *Journal of the Royal Statistical Society, Series B.*

Tibshirani R (2011). Regression shrinkage and selection via the lasso: a retrospective. *Journal of the Royal Statistical Society: Series B (Statistical Methodology)* **73**(3): 273-282.

Toiviainen P, Alluri V, Brattico E, Wallentin M, Vuust P Capturing the musical brain with Lasso: Dynamic decoding of musical features from fMRI data. (1095-9572 (Electronic)).

Uddin MT, Uddiny MA (eds) (2015). Human activity recognition from wearable sensors using extremely randomized trees. *Electrical Engineering and Information Communication Technology (ICEEICT), 2015 International Conference on.* 21-23 May 2015.

Wade BS, Joshi SH, Njau S, Leaver AM, Vasavada M, Woods RP*, et al* (2016). Effect of Electroconvulsive Therapy on Striatal Morphometry in Major Depressive Disorder. *Neuropsychopharmacology : official publication of the American College of Neuropsychopharmacology*.

Wade BS, Joshi SH, Pirnia T, Leaver AM, Woods RP, Thompson PM*, et al* (2015a). Random Forest Classification of Depression Status Based On Subcortical Brain Morphometry Following Electroconvulsive Therapy. *Proceedings / IEEE International Symposium on Biomedical Imaging: from nano to macro IEEE International Symposium on Biomedical Imaging* **2015**: 92-96.

Wade BS, Valcour VG, Wendelken-Riegelhaupt L, Esmaeili-Firidouni P, Joshi SH, Gutman BA*, et al* (2015b). Mapping abnormal subcortical brain morphometry in an elderly HIV + cohort. *NeuroImage Clinical* **9**: 564-573.

Weiner MW, Veitch DP, Aisen PS, Beckett La, Cairns NJ, Green RC*, et al* (2012). The Alzheimer's Disease Neuroimaging Initiative: a review of papers published since its inception. *Alzheimer's & dementia : the journal of the Alzheimer's Association* **8**(1 Suppl): S1-68.

Westman E, Muehlboeck JS, Simmons A (2012). Combining MRI and CSF measures for classification of Alzheimer's disease and prediction of mild cognitive impairment conversion. *NeuroImage* **62**(1): 229-238.

Wolpert DH, Macready WG (1997). No free lunch theorems for optimization. *Evolutionary Computation, IEEE Transactions on* **1**(1): 67-82.

Zhang D, Shen D Multi-modal multi-task learning for joint prediction of multiple regression and classification variables in Alzheimer's disease. (1095-9572 (Electronic)).

Zou H, Hastie T (2005). Regularization and variable selection via the elastic net. *Journal of the Royal Statistical Society: Series B (Statistical Methodology)* **67**(2): 301-320.

Tables

Table 2-1. AUC values for feature-selection-classifier pairings by shape metric, diagnostic contrast and sample size.

		100% of Observations				50% of Observations				25% of Observations			
		RD		JD		RD		JD		RD		JD	
Classifier	Selection	AD	MCI	AD	MCI	AD	MCI	AD	MCI	AD	MCI	AD	MCI
RF	NFS	90	76	87	72	89	74	88	72	91	79	89	71
RF	RRF	90	76	87	72	89	75	89	72	88	82	87	68
RF	LASSO	89	77	88	72	87	72	88	72	85	80	85	68
SVM	NFS	91	76	88	75	84	67	82	67	85	68	84	65
SVM	RRF	90	77	87	73	84	68	83	66	81	70	80	62
SVM	LASSO	88	74	88	72	81	62	84	65	79	67	79	65
NB	NFS	84	70	78	66	84	67	81	38	83	71	83	67
NB	RRF	88	73	81	66	87	72	86	68	89	78	86	71
NB	LASSO	88	74	82	68	82	68	83	61	77	77	67	66

Figures

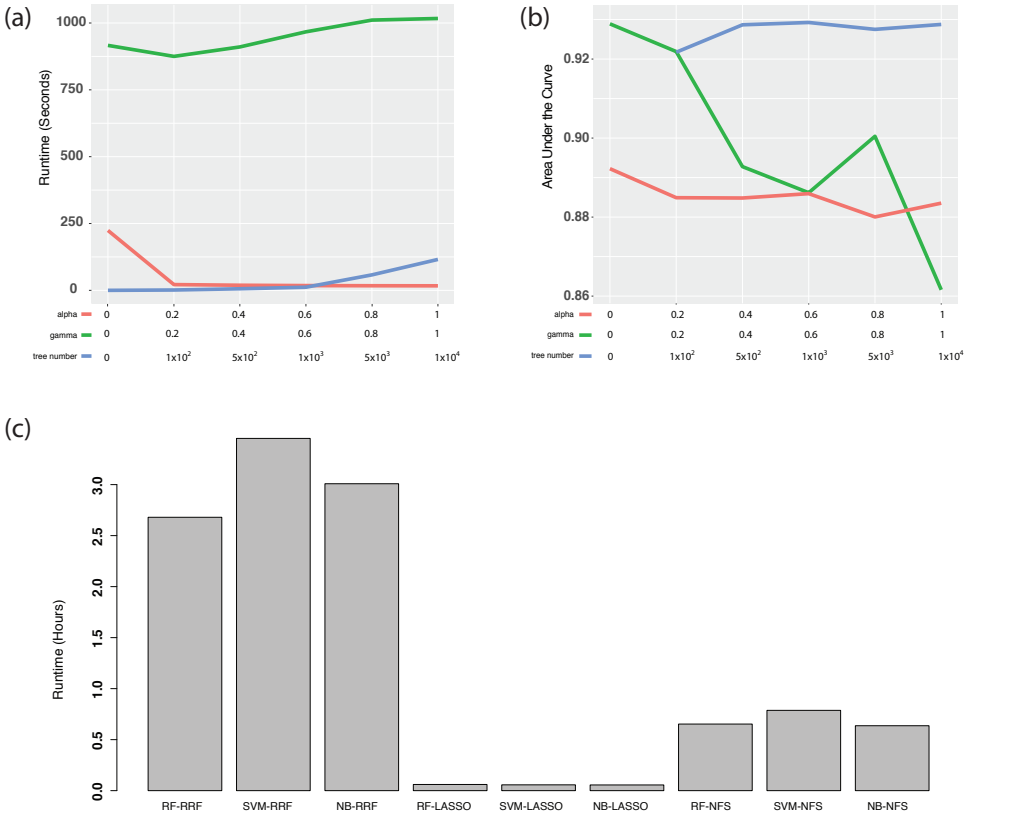

Figure 2-1. Benchmarking and performance evaluation for variable parameterizations of (a-b) feature selection methods and (c) total runtime for all 10-folds of each pairing of feature selection and classification approach. (a) Plots the average runtime of each parameterization of elastic net α value, RRF γ value and tree number. System runtime is given in seconds and is averaged across 10 cross validations using the radial distance measures to classify Alzheimer's disease from normal controls. (b) Plots the average AUC associated with each parameterization of the feature selection methods. For (c) system runtime is given in hours and is the total runtime across all 10 cross validation folds.

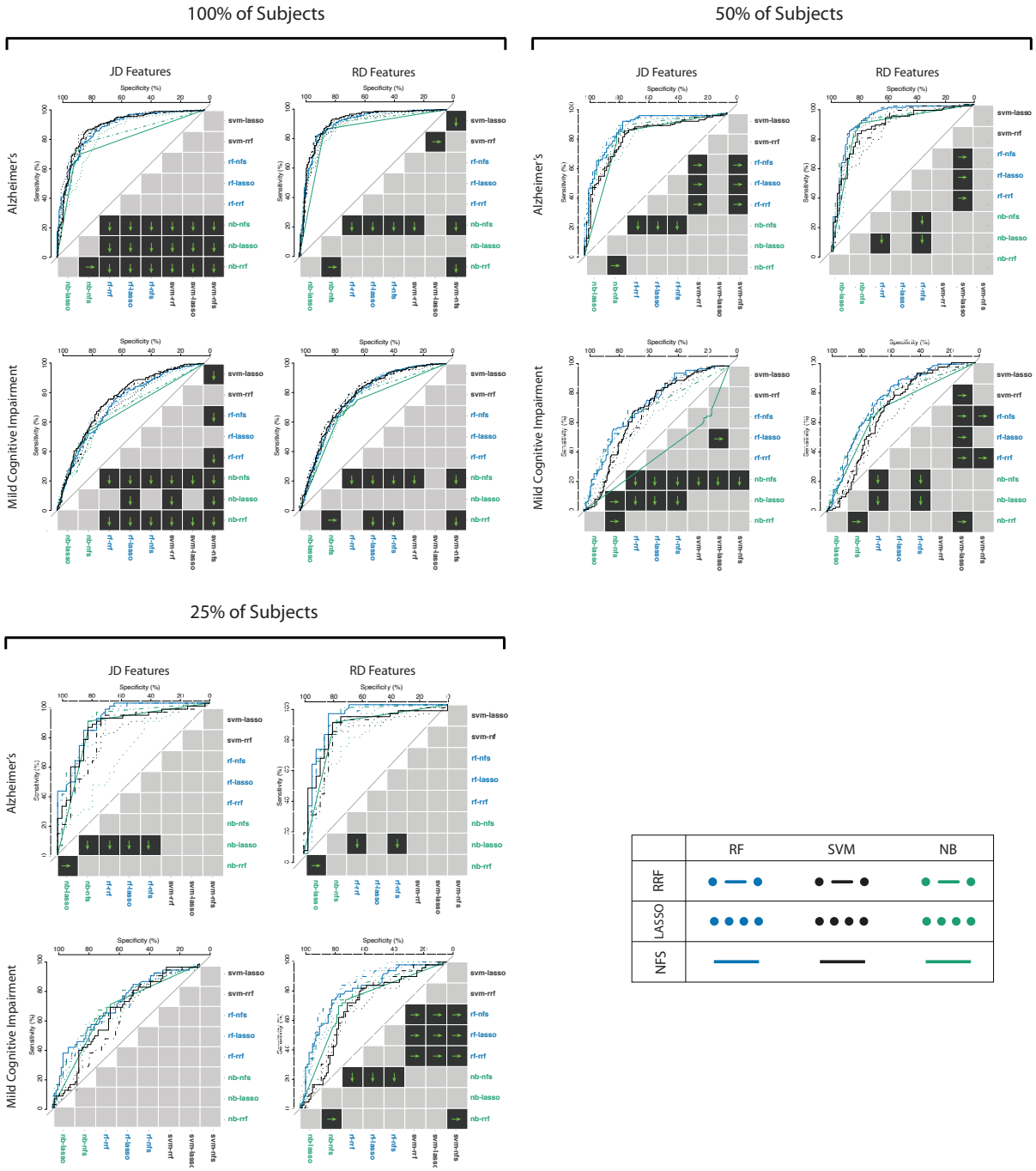

Figure 2-2. ROC curves and pairwise significance tests across differing sample sizes. Each row contains ROCs by diagnostic contrast with shape descriptors column wise. ROC curves are color coded to match the type of classifier while line type is matched based on the feature selection method used. The lower triangle of each figure is the pairwise Delong's test for difference in AUC. Black intersections indicate significant differences in AUC following FDR. Arrows inside each black intersection point to the name of the approach with the significantly larger AUC value.

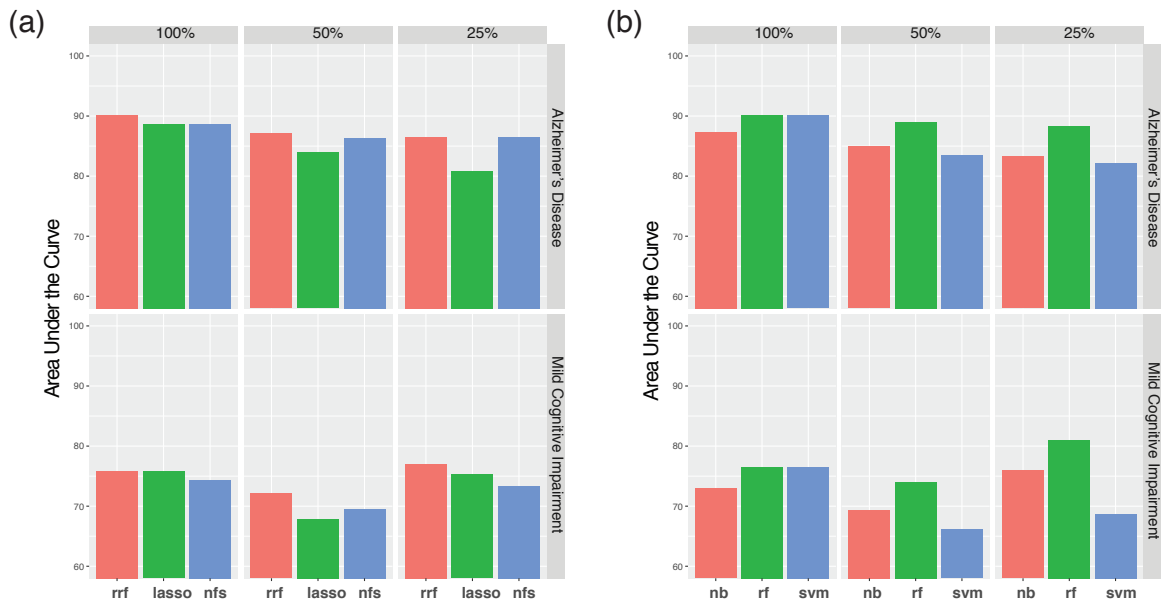

Figure 2-3. AUC by diagnostic contrast by shape metric and sample size averaged across (a) feature selection method and (b) classifier.

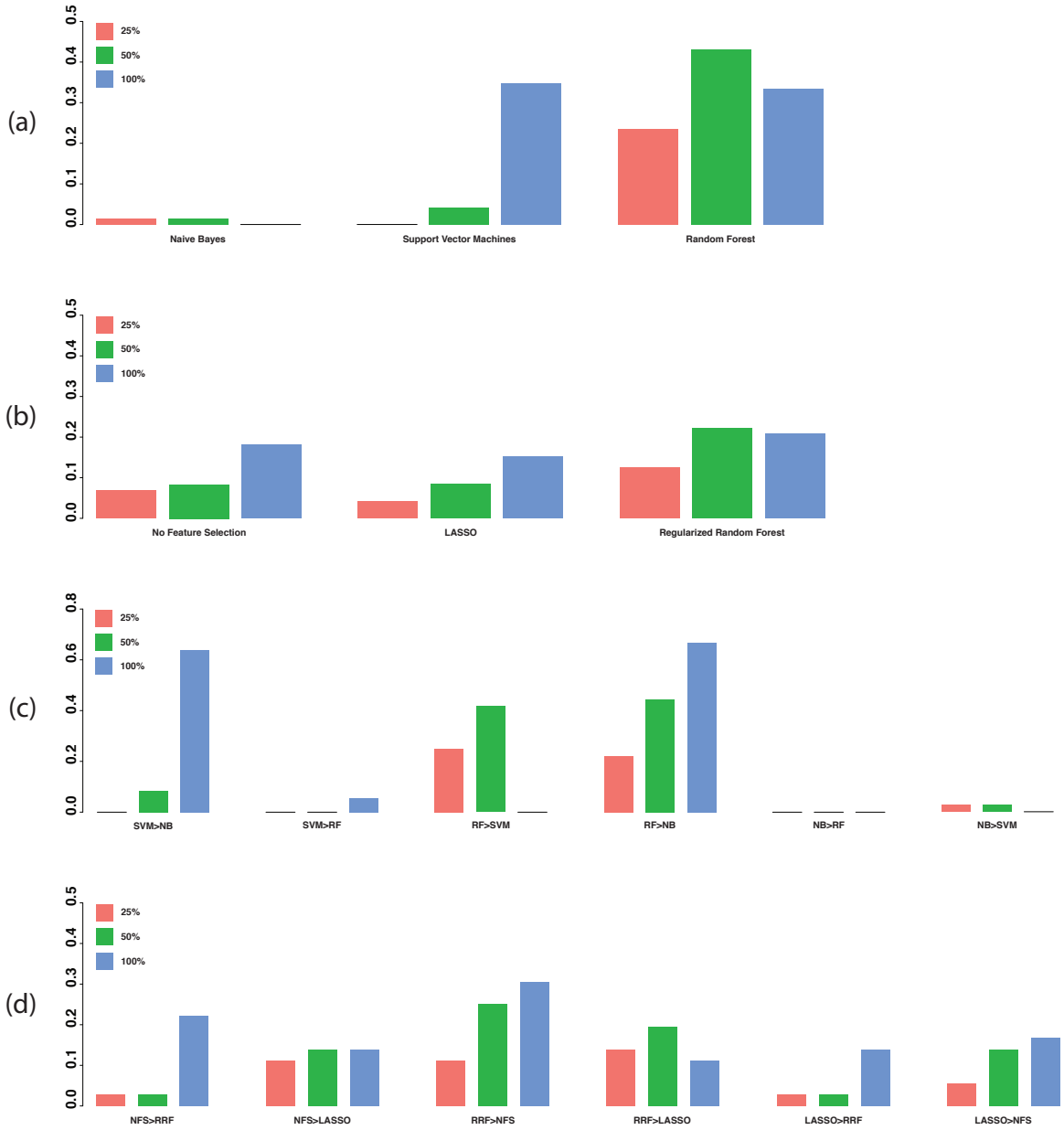

Figure 2-4. Summary of performances of classification and feature selection methods across sample sizes. (a) Percentage of instances in which classifiers have significantly largest AUC value among all comparisons excluding comparisons to itself. (b) Percentage of instances in which a given feature selection method offers significantly largest AUC value among all comparisons excluding comparisons to itself. (c) Percent of instances in which classifiers significantly outperformed other classifiers. (d) Percent of instances in which feature selection methods significantly outperformed other feature selection methods.

Supplementary figures

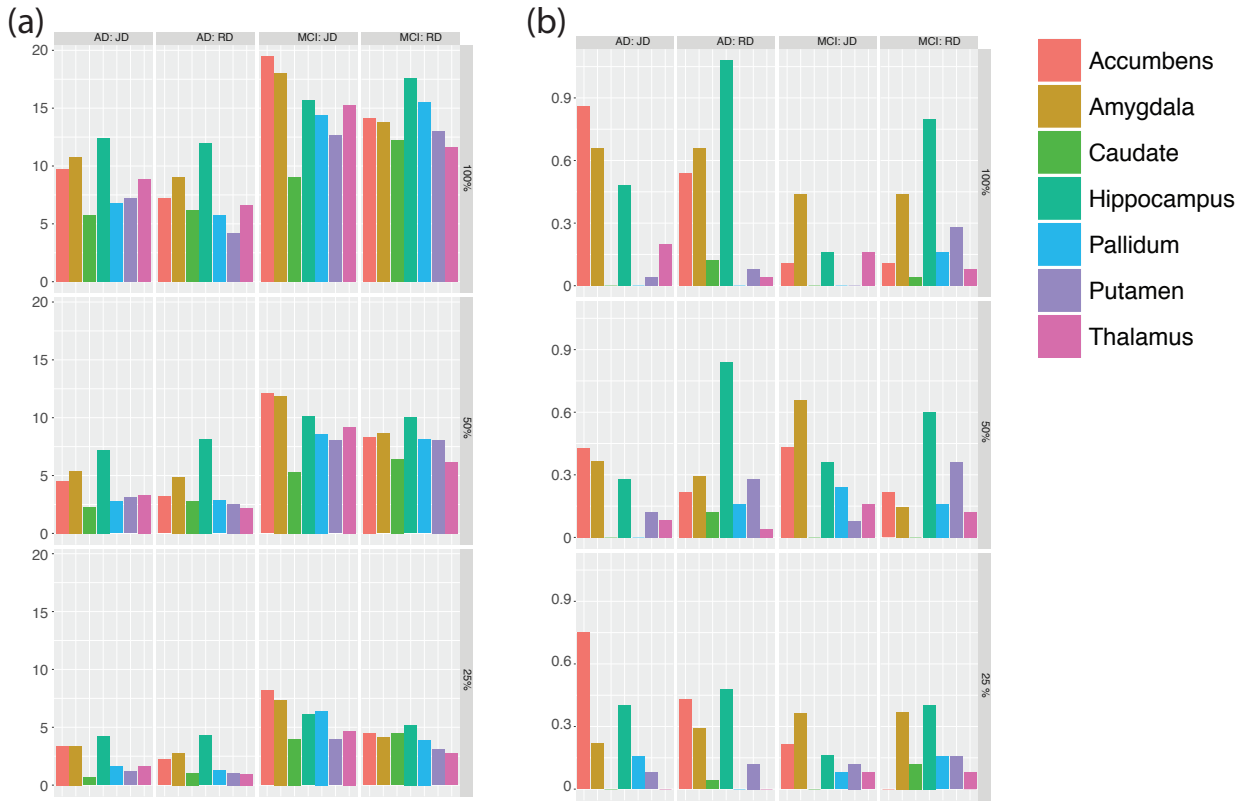

Figure 2-S1. Bar plots of the percentage of features retained under (a) RRF and (b) LASSO stratified by diagnostic contrast, feature set (RD or JD) and percentage of subjects in each sample.

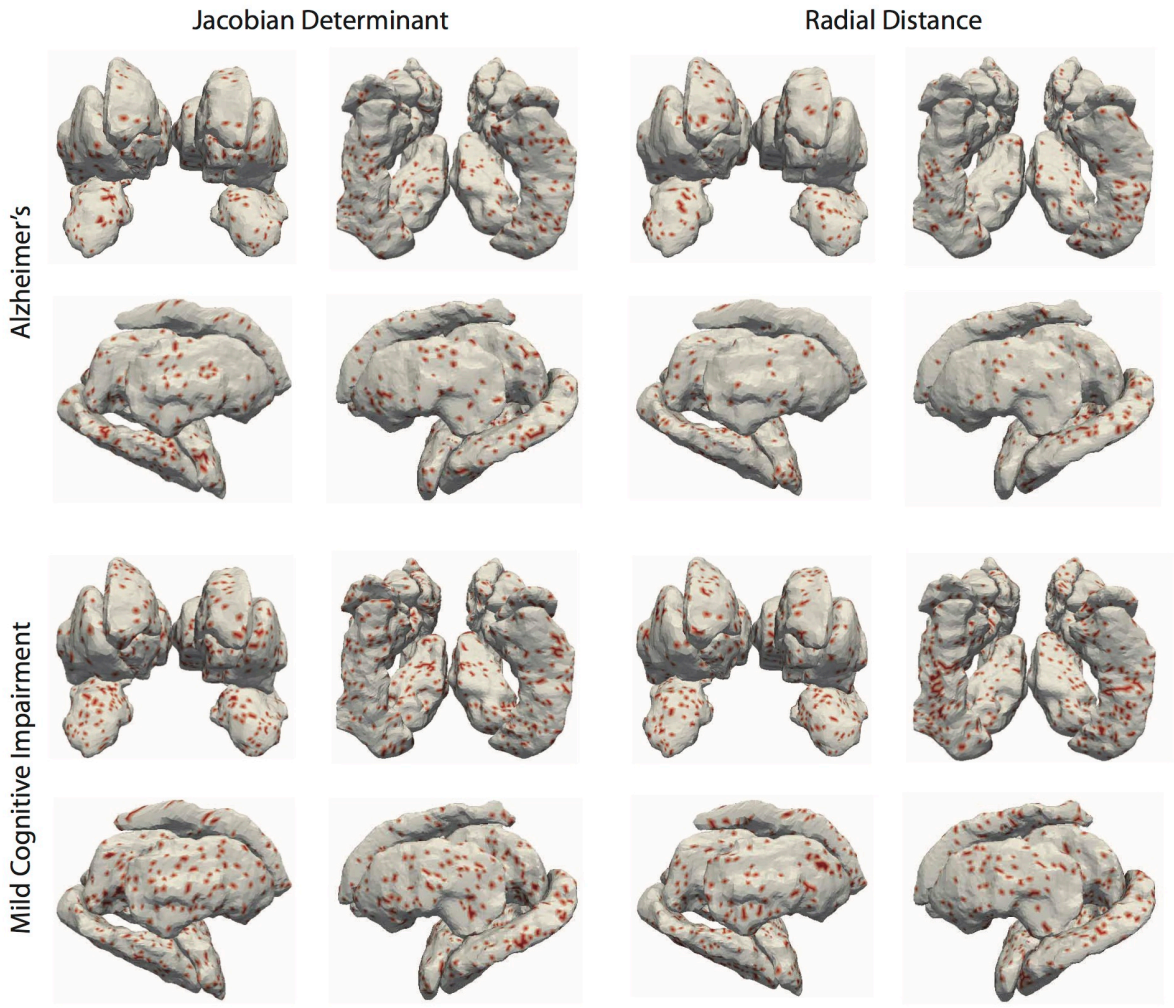

Figure 2-S2. Mapping of LASSO coefficients from single cross validation fold to subcortical surfaces. Since the LASSO feature selection operated by retaining all features with a non-zero coefficient all highlighted regions are effectively the feature subset.

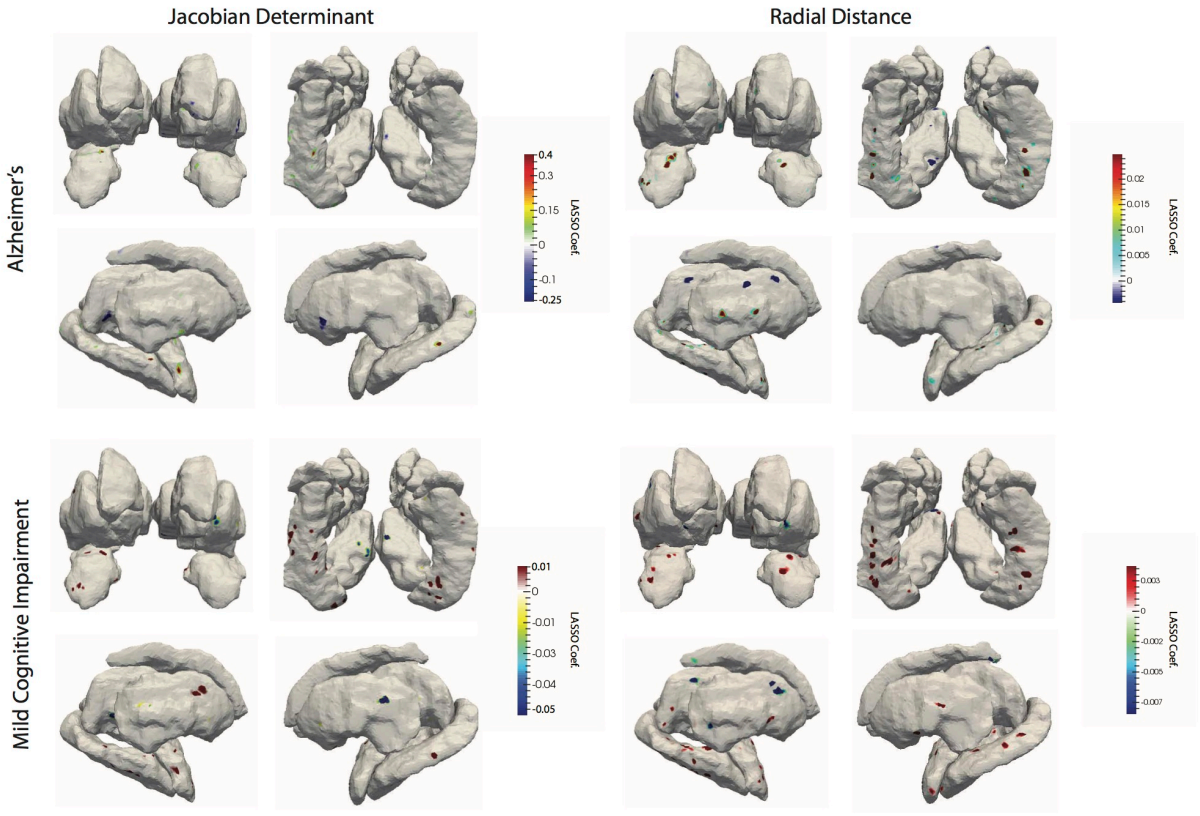

Figure 2-S3. Mapping of RRF-selected regions from single cross validation fold to subcortical surfaces.

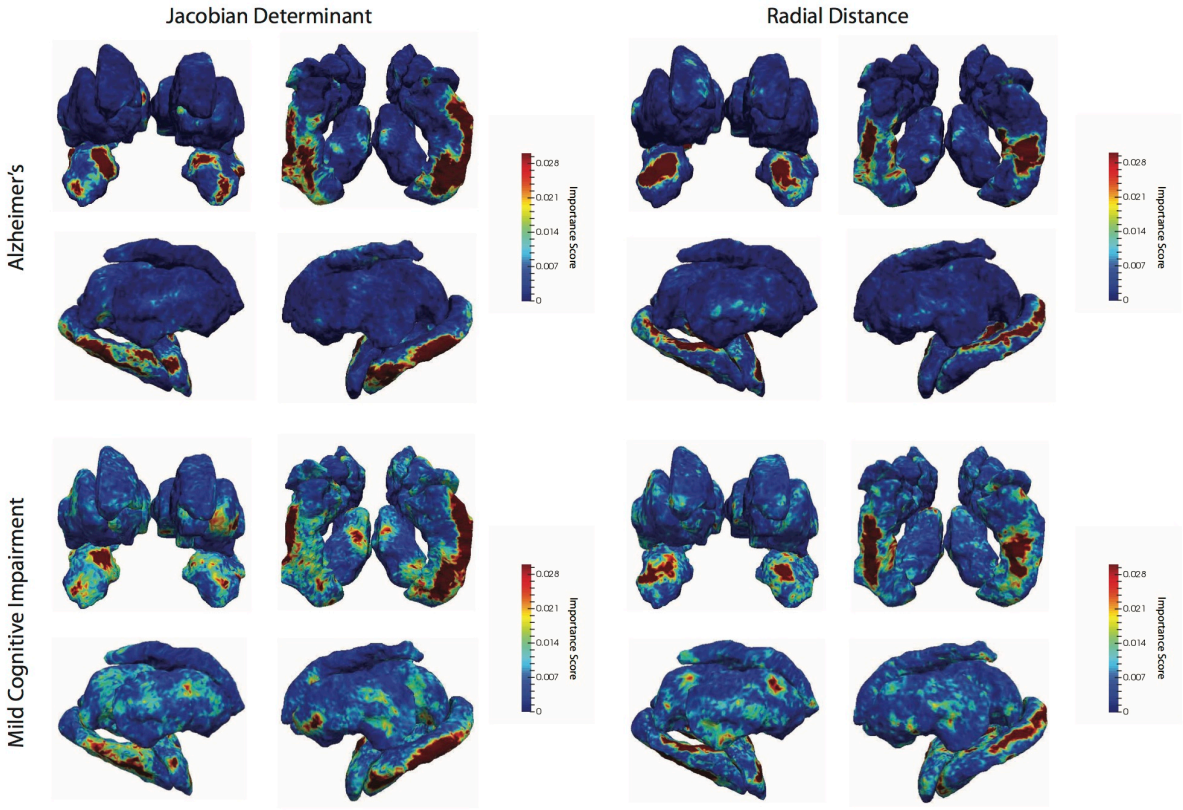

Figure 2-S4. Mapping of RRF importance scores from single cross validation fold to subcortical surfaces.

Chapter 3: Mapping Abnormal Subcortical Brain Morphometry in an Elderly HIV+ Cohort[2]

Over 50% of HIV+ individuals exhibit neurocognitive impairment and subcortical atrophy, but the profile of brain abnormalities associated with HIV is still poorly understood. Using surface-based shape analyses, we mapped the 3D profile of subcortical morphometry in 63 elderly HIV+ participants and 31 uninfected controls. The thalamus, caudate, putamen, pallidum, hippocampus, amygdala, brainstem, accumbens, callosum and ventricles were segmented from high-resolution MRIs. To investigate shape-based morphometry, we analyzed the Jacobian determinant (JD) and radial distances (RD) defined on each region's surfaces. We also investigated effects of nadir CD4+ T-cell counts, viral load, time since diagnosis (TSD) and cognition on subcortical morphology. Lastly, we explored whether HIV+ participants were distinguishable from unaffected controls in a machine learning context. All shape and volume features were included in a random forest (RF) model. The model was validated with 2-fold cross-validation. Volumes of HIV+ participants' bilateral thalamus, left pallidum, left putamen and callosum were significantly reduced while ventricular spaces were enlarged. Significant shape variation was associated with HIV status, TSD and the Wechsler adult intelligence scale. HIV+ people had diffuse atrophy, particularly in the caudate, putamen, hippocampus and thalamus. Unexpectedly, extended TSD was associated with increased thickness of the anterior right pallidum. In the classification of HIV+ participants vs. controls, our RF model attained an area under the curve of 72%.

[2] The content of this chapter has been published as B. S. Wade, V. G. Valcour, L. Wendelken-Riegelhaupt, P. Esmaeili-Firidouni, S. H. Joshi, B. A. Gutman, *et al*., "Mapping abnormal subcortical brain morphometry in an elderly HIV + cohort," *Neuroimage Clin,* vol. 9, pp. 564-73, 2015.

Introduction

Combined antiretroviral therapy (cART) has vastly improved the quality of life for people infected with human immunodeficiency virus (HIV), allowing many to live to an advanced age. The over 55 demographic is the most rapidly growing age group of HIV+ individuals (Hall *et al*, 2008). Yet, following the increased life expectancy, numerous reports studying chronic infection indicate that HIV positivity independently contributes to and synergistically exacerbates age-related neurodegeneration (Canizares *et al*, 2014; Cohen *et al*, 2015) which in many cases results in dramatic cognitive declines and decreased quality of life, with upwards of 50% proceeding to develop a degree of HIV-associated neurocognitive disorders (HAND) (Cysique *et al*, 2004; Simioni *et al*, 2010). Several potential mechanisms for neuronal atrophy have been reported including chronic inflammation, interrupted metabolic processes, immunological senescence, heightened risk for cardiovascular disorders and even side effects of cART. For a more detailed review of these factors we refer the reader to (Canizares *et al*, 2014).

Numerous studies support the view that central nervous system infection parallels the aging process. The Multicenter AIDS Cohort Study (MACS), implementing a longitudinal study with a 5-year follow-up, identified an interaction between HIV status, age and time whereby middle-aged and elderly infected participants exhibited a significant decline in executive function over time relative to uninfected controls who showed no reduction in performance with respect to time (Sacktor *et al*, 2010). In contrast, (Cysique *et al*, 2011) observed that age and HIV status independently contributed to cognitive decline but were unable replicate an interaction between the two.

Literature from structural MRI widely reports age disproportionate degrees of atrophy among HIV+ cohorts. (Becker *et al*, 2012; Thompson *et al*, 2005; Towgood *et al*, 2012) have

reported both HIV-related reductions in frontal grey matter. HIV and age associated reductions in subcortical structures are also widely reported (Ances *et al*, 2012). Diffusion tensor imaging has revealed interactive effects of HIV status and age in the reduction of fractional anisotropy and increase of mean diffusivity within subcortical white matter and frontal regions (Chen *et al*, 2009). Magnetic resonance spectroscopy reports also suggest that CNS HIV infection mimics the effects of aging. (Chang *et al*, 2004; Harezlak *et al*, 2011) both reported higher choline compounds (CHO) : total creatine (CR) and myoinositol (MI) : CR ratios in the basal ganglia associated with aging and HIV status.

Given the complications presented by the synergistic effects of aging and HIV, it is important to further understand the morphological differences that occur between normal aging and aging influenced by HIV infection. While several studies have investigated volumetric differences in elderly HIV+ cohorts, a thorough description of shape differences in elderly HIV+ subjects remains to be explored. Local descriptions of shape variation may offer an additional characterization of HIV-related neurodegeneration by describing localized regions of tissue atrophy and expansion. This level of description could be leveraged as an additional biomarker for the detection of aberrant degeneration, allowing clinicians to offer more targeted interventions when needed.

We report on both the subcortical volumetric and 3D surface-based shape abnormalities in a cohort of 63 elderly HIV+ subjects scanned with high-resolution structural magnetic resonance imaging (MRI) as part of the UCSF (University of California, San Francisco) HIV Over 60 Cohort study. To study subcortical shape, we analyzed: (1) the log of the Jacobian determinant (JD) indexed over structures' surface coordinates and (2) radial distances (RD) of structure surfaces from a medial curve. JD maps indicate localized atrophy or dilation of a

surface area. Complementary to JD, RD indicates the local "thickness" of the structure. We tested associations of morphological descriptors with neuropsychological measures: the Wechsler Adult Intelligence Scale (WAIS) and Wide Range Achievement Test (WRAT) scale. We also tested for associations with several common HIV clinical indices: nadir CD4+ T-cell count (nCD4), time since diagnosis (TSD; in years), and HIV RNA level in plasma. We hypothesized that subcortical shape analysis would reveal regions of significant atrophy in HIV+ people relative to matched controls and in relation to clinical markers of HIV.

We additionally explored the use of shape and volume features in a machine learning framework to classify participants as HIV+ or HIV- using a random forest (RF) classifier; a class of supervised machine learning algorithms that has gained popularity for its accuracy, ease of use, and computational efficiency. Here, the application of machine learning based on brain morphometry is not intended as a potential means of clinical HIV diagnosis; rather the ability to robustly distinguish HIV status based on brain-derived measures would validate that observed differences are highly associated with infection status and potentially relevant to the prediction of further HIV-related neurological atrophy. To our knowledge this is the first study to explore classification of HIV status based solely on brain morphometry.

Methods

Subjects

A sample of 63 elderly HIV+ subjects (2 female; age=64.68 $\pm$ 4.57) and 31 uninfected elderly controls (4 female; age=65.35 $\pm$ 2.21) were recruited as part of a San Francisco Bay Area study of elderly people with HIV. HIV+ participants had an average nCD4 count of 204. 96 $\pm$ 154.85 cells/mm^3, an average TSD of 20.39 years $\pm$ 6.31 years. 24 HIV+ participants had detectable levels of viral RNA (above 50 copies/mm^3). Among those with detectable HIV RNA,

the average viral load was 16,380.58 ± 76,418.68 copies/mm^3. All subjects gave informed consent to take part in the study. Table 3-1 outlines the demographic and clinical characteristics of the participants.

Image acquisition

Each subject underwent a whole-brain high-resolution magnetic resonance imaging (MRI) anatomical brain scan on a Siemens 3 Tesla TIM Trio scanner with a 12-channel head coil. T1-weighted MP-RAGE sequences (240 x 256 matrix; FOV = 256mm; 160 slices; voxel size = 1.0 x 1.0 x 1.0 mm^3; TI = 900 ms; TR = 2300 ms; TE = 2.98 ms; flip angle = 9°.

Morphological descriptors

Previously validated FreeSurfer (Fischl *et al*) workflows, including non-brain tissue removal, intensity normalization and automated volumetric parcellation based on probabilistic information from manually labeled training sets, were used to segment the bilateral thalamus, putamen, pallidum, amygdala, accumbens, caudate and hippocampus from the raw MRIs. All segmentations were visually inspected to ensure their quality.

The parameterization of each surface was obtained using the "medial demons" method detailed in (Gutman *et al*, 2015; Gutman *et al*, 2012). Briefly, each surface was conformally mapped to the spherical domain. The spherical maps were rigidly rotated to a probabilistic atlas. Next, Spherical Demons (SD) (Gutman *et al*, 2013) was used to non-linearly register the spherical maps on the basis of curvature. Two surface-based functions were defined to do this; first, the global orientation function, defining the direction of the surface and, secondly, the local thickness of the surface with respect to a skeletonized medial core. Finally, SD was implemented again using both the newly defined medial core in conjunction with surface-based curvature to match each surface to the atlas.

From this process, two shape features are defined at each vertex: 1) radial distance (RD), a proxy for thickness and 2) the log of the Jacobian determinant (JD) which indicates surface dilation or atrophy. Among all 14 brain region surfaces, there were a total of 27,120 vertices.

Statistical methods

Multiple linear regression was used to model influences of HIV status, nCD4 count, viral load, TSD, HAND status and drug abuse history on the morphometry of each surfaces. The general linear model assumed the following form,

$$Y = \beta_0 + \beta_1 \cdot \text{Main Effect} + \beta_2 \cdot \text{Age} + \beta_3 \cdot \text{Sex} + \beta_4 \cdot \text{ICV} + \epsilon \qquad (1)$$

where *Y* is global volume, for one of the regions, or the locally computed JD or RD; Main Effect is one of HIV status, nCD4 count, viral load or TSD, HAND or drug abuse history. This model was fitted at each of the surface vertices when the outcome of interest was the shape measure, JD or RD. HIV status and viral load were each modeled dichotomously; HIV status was coded as positive or negative and viral load as detectable (above 50 viral RNA copies/mm^3) or undetectable (i.e., binary). nCD4 and TSD were modeled continuously. HAND status and drug abuse history were modeled as positive or negative. HAND encompasses a range of impairments including asymptomatic neurocognitive impairment (ANI), mild neurocognitive disorder (MND) and HIV-associated dementia (HAD); a subject having any of these was considered HAND positive in the regression model. Similarly, due to the small number of subjects having a history of drug abuse we simply model any of, marijuana, cocaine, crack or methamphetamine as having a history of abuse.

Associations of morphometry and cognitive measures were modeled using the following general linear model,

$$Y = \beta_0 + \beta_1 \cdot \text{Main Effect} + \beta_2 \cdot \text{HIV Status} + \beta_3 \cdot \text{Age} + \beta_4 \cdot \text{Sex} + \beta_5 \cdot \text{ICV}$$

$$+ \beta_5 \cdot (\text{Main Effect} \cdot \text{HIV Status}) + \epsilon \quad (2)$$

where Main Effect is one of WAIS or WRAT score modeled continuously and HIV Status is a dichotomous term.

We controlled for multiple comparisons using the standard false discovery rate (FDR) method with a false-positive rate of 5% ($q = 0.05$) (Benjamini and Hochberg, 1995). FDR was performed separately for volumetric and shape-based tests. For the family of volumetric tests, FDR was applied to the set of all subcortical structures. For shape analyses we applied an FDR correction within the family of all tests performed on a single surface; correcting for separate tests within each surface.

Random forest classification

In addition to mapping differences in subcortical morphometry, we wanted to investigate the efficacy of our morphometric descriptors as input features in a machine learning, classification context. Here, we describe the RF framework used in this study.

Developed and detailed by (Breiman, 2001), RFs are supervised classifiers composed of an ensemble of classification and regression trees (CART) and use the majority vote of its terminal nodes to predict the class of a given observation. RF CARTs are constructed from a bootstrapped sample of approximately 2/3 of the original observations. At each node of the CART, a random subset of $\sqrt{M}$ features is assessed. Here the Gini impurity index is calculated for each feature at the given node, v. Gini(v) is given by

$$\mathrm{Gini(v)} = \sum_{\mathrm{C=1}}^{\mathrm{C}} \hat{\mathrm{p}}_{\mathrm{c}}^{\mathrm{v}} \left(1 - \hat{\mathrm{p}}_{\mathrm{c}}^{\mathrm{v}}\right) \tag{3}$$

where $\hat{p}_c^v$ is the proportion of observations belonging to class C at node v. The objective of the RF algorithm is to split each CART node by the feature X_i which maximizes the class purity of the resultant child nodes, v^r and v^l. This is done by choosing the maximum $\mathrm{Gain(X_i, v)}$ given by,

$$\mathrm{Gain\ (X_i, v)} = \mathrm{Gini(X_i, v)} - \omega_{\mathrm{l}}\mathrm{Gini}\left(\mathrm{X_i, v^l}\right) - \omega_{\mathrm{r}}\mathrm{Gini(X_i, v^r)}, \tag{4}$$

where ω_l and ω_r are the proportions of observations in node v assigned to child nodes v^r and v^l, respectively. The importance I, of feature X_i is given by the summation of the decreases in the Gini index at each node where the CART was partitioned by X_i (Gray *et al*, 2013). That is,

$$\mathrm{I_{X_i}} = \frac{1}{\text{total tree number}} \sum_{\mathrm{v} \in \mathrm{S_{X_i}}} \mathrm{Gain(X_i, v)}, \tag{5}$$

where S_{X_i} indicates the set of all nodes split by X_i. Each CART was grown to its full, unpruned extent.

Our RF model was implemented in R (R Core Team, 2014) and used the RRF package (Deng, 2013). The RF was composed of 5000 trees. We trained the model on half of the participants, stratified by HIV status, using the remaining half for cross validation. The training set consisted of 28 HIV+ and 15 HIV- participants while the test set included 27 HIV+ and 15 HIV- participants. The RF model was constructed using a combination of all morphological features; all volumetric, RD and JD values were entered as predictors of HIV status.

The significance of the RF was assessed using a permutation test. This was done by first computing the observed area under (AUC) the receiver operating characteristic curve (ROC)

from the prediction of the test set. This observed AUC was compared to a null distribution of 1000 AUC values resulting from the classification of HIV status based on randomly shuffling the labels associated with the observed prediction. The proportion of AUCs in the null distribution that were larger than the observed AUC is the p-value associated with the null hypothesis that the observed AUC is less than or equal to 50%, i.e. classification is no better than chance.

As a follow-up analysis we constructed RF classifiers on feature sets composed uniquely of either RD, JD or volumetric measures. We corrected for the set of all classifier p-values using FDR correction for multiple comparisons.

Results

We found several associations between subcortical morphometry and HIV status and clinical parameters. In the following sections we outline the observed morphometry associated with HIV status, nadir CD4 count, detectability of viral load and TSD.

HIV status

Volumetrically, the callosum (β_{dx} = -290, -10.7%, t = -2.81, $p < 0.05$), left pallidum (β_{dx} = -180, -7.6%, t = -3.47, $p < 0.01$), left putamen (β_{dx} = -330, -5.7%, t = -2.40, $p < 0.05$), left thalamus (β_{dx} = -390, -5.9%, t = -2.91, $p < 0.05$) and right thalamus (β_{dx} = -440, -6.3%, t = -3.00, $p < 0.05$) were all significantly smaller in HIV+ participants. Ventricular spaces were, on average, enlarged in HIV+ subjects. Specifically, the left lateral (β_{dx} = 5100, 12.7%, t = 2.88, $p < 0.05$), right lateral (β_{dx} = 3900, 8%, t = 2.41, $p < 0.05$) and third (β_{dx} = 420, 15.5%, t = 3.68, $p < 0.01$) ventricular spaces were all significantly larger in HIV+ participants. **Figure 3-1** illustrates volumetric differences between HIV+ and HIV- participants. All units for volumetric measures are in mm^3.

Shape mapping revealed widespread regions of atrophy in the HIV+ cohort. Specifically, RD maps, illustrated in **Figure 3-2**(a), identified significant atrophy of the bilateral medial aspect of the caudate head; regions of atrophy and expansion were observed in the posterior tail regions as well. Several regions of the bilateral pallidum, left putamen and right inferior thalamus and inferior hippocampus were also significantly atrophied in HIV+ participants. JD mapping, depicted in **Figure 3-2**(b), corroborated the observed widespread atrophy in a set of regions only partially overlapping with those found in the RD maps. The JD maps highlight atrophy laterally and medially in the bilateral thalamus, anteriorly in the left putamen and right accumbens and in the inferior-posterior right hippocampus. Morphometry differences outside of these regions were below the set statistical threshold of significance.

Nadir CD4+ counts

There were no detectable volumetric or shape-based associations between nCD4 counts and morphometry.

Viral load

No significant shape or volume differences were found between HIV+ participants with and without detectable viral RNA levels.

Time since diagnosis

The volume of the right pallidum ($\beta_{duration}$ = 6.3, t = 2.43, p > 0.05) was positively associated with TSD prior to correction for multiple comparisons but failed to survive FDR. Corroborating this, both RD and JD maps of the right pallidum indicate significant local expansion in its anterior aspect in relation to increased TSD; RD and JD results survived FDR (see **Figure 3-3**).

Drug abuse history

No significant associations were found between brain morphometry and drug abuse history.

HIV-associated neurocognitive disorder

HAND revealed no observable associations with brain morphometry.

Cognitive measures

Both WAIS and WRAT scores were significantly larger in the HIV- cohort, $t(54) = -3.97$, and $t(70) = -3.43$, respectively, both $p < 0.001$. The interaction of HIV status and WAIS or WRAT score was not significantly associated with volume. However, the thickness of the left caudate was widely associated with the interaction of HIV status and WAIS score. **Figure 3-4** maps both the main effect of WAIS score (c-d) and the interaction of HIV status and WAIS score (a-b) on subcortical thickness. Figure 3-4 (c-d) indicates that WAIS is significantly positively associated with left caudate thickness in the control group. Figure 3-4(a-b) indicates that the magnitude of the association is significantly reduced in the HIV+ cohort. The direction of the association between thickness and WAIS score is shown to be inverse in (e-f), which maps the association only within HIV+ participants. No significant associations between shape and WRAT score were observed.

HIV status classification

Classification of HIV status using the full set of morphology descriptors with a 2-fold cross validation yielded an area under the receiver operating characteristic (ROC) curve (AUC) of 72.3% ($q = 0.025$). We also used a more computationally expensive leave-one-out cross validation, but this did not improve our classifier's performance, giving an AUC of 71.9%.

Again, using 2-fold cross validation, we investigated the performance of feature subsets comprised exclusively of one of, volume, RD or JD features. **Figure 3-5** plots the ROC curves for each set of classifier inputs. The volumetric subset afforded an AUC of 70.4% (q = 0.025); RD 72.3% (q = 0. 025) and JD 65.8% (q = 0.080).

In **Figure 3-6** we mapped the importance scores of each RD and JD value derived from the RF model to the corresponding surface location, providing a visual representation of how each region's shape-based morphometry drove the RF model. **Figure 3-7** complements this by plotting the importance score for each region; RD and JD-based importance scores were averaged within each surface. **Figure 3-7** indicates that RD features were weighted more heavily than their JD counterparts. We also note that the only volumetric measure that was relevant to the RF was the left pallidum. Comparing **Figure 3-6** to **Figure 3-2**, there is widespread correspondence between regions considered important to the RF classifier and regions that were statistically significant in modeling the effects of HIV. While this is perhaps not surprising, it serves to validate both sets of findings.

Discussion

The development of cART has allowed for HIV infected individuals to live to advanced ages and as a result it is estimated that the proportion of HIV+ people over the age of 45 years is close to 50% and the demographic of over 55 years is the most rapidly growing among those with HIV (Cohen *et al*, 2015; Hall *et al*, 2008). While cardiovascular diseases such as stroke and hypertension (Gorelick *et al*, 2011) as well as depression (Vink *et al*, 2009) and diabetes (McBean *et al*, 2004) are all common comorbidities associated with aging and may contribute to neurodegeneration, accumulating evidence indicates that HIV exacerbates and uniquely contributes to age-related neurodegeneration (Holt *et al*, 2012). Several lines of evidence have

also suggested that particular cART therapies may have neurotoxic properties that affect cognition and brain aging (Ances *et al*, 2008; Robertson *et al*, 2010; Schweinsburg *et al*, 2005). The advancing age of the HIV+ population and the suggested viral contribution to the aging process underlies the importance of characterizing the progression of brain atrophy in the older HIV population. The development of biomarkers to track the extent of the viral effects in the central nervous system may help to further inform clinicians in selecting the appropriate line of therapy for a particular patient. Using standard volumetric and novel surface-based shape descriptors we were able to identify several important HIV-related patterns of brain abnormalities.

Previous studies have noted that HIV has a proclivity for subcortical regions such as the basal ganglia (Aylward *et al*, 1995; Aylward *et al*, 1993; Berger and Nath, 2000; Gottumukkala *et al*, 2014) where the virus may replicate and maintain a reservoir despite active cART therapy. Atrophy of these subcortical regions is commonly reported in HIV-infected individuals. Other reported abnormalities of subcortical structures include hypermetabolism of the thalamus and basal ganglia (Drevets, 2001), a reduction in dopaminergic transporters in the putamen and striatum and increased mean diffusion in the putamen (Chang *et al*, 2008). Corroborating these reported effects, we observed that HIV positivity was associated with greater subcortical atrophy, particularly in the caudate, putamen, pallidum, hippocampus and callosum.

Unexpectedly, we observed a dilation in the anterior aspect of the right pallidum in relation to extended TSD. Several subjects in our HIV+ cohort had a history of methamphetamine use which has been linked to enlarged subcortical volumes (Chang *et al*, 2005; Jernigan *et al*, 2005), however we did not observe an association between drug abuse history and subcortical morphometry. Another possible concern is that TSD could be confounded

by participant age. However, this seems unlikely given the relatively low standard deviation of age among the HIV+ cohort (SD = 4.57).

WAIS scores were differentially associated with the thickness of the left caudate with a positive association within the control group and a negative association within the HIV+ group. The reason for this inverse association remains unclear.

We expected to see patterns of morphometry associated with common clinical measures linked to HIV such as viral load and nadir CD4 count, but none of these associations were significant. This may be due, in part, to limited power, as all subjects were on cART with relatively high CD4 counts and either undetectable or very low plasma HIV RNA levels. To alleviate this, our ENIGMA consortium is beginning a larger-scale project to relate clinical markers of HIV disease burden to brain measures across multiple cohorts (Jean-Paul Fouche *et al*, 2015).

In addition to mapping abnormal subcortical morphometry, we used the morphological descriptors to predict HIV status in a RF framework. While a simpler logistic classifier was considered the dimensionality of our feature set renders these simpler models less tractable and required initial feature selection and feature scaling to allow convergence. Given the requirement of extra steps for a logistic model and the natural added value of importance scores, the RF was a natural choice. This type of predictive framework helps to verify that observed group differences robustly distinguish HIV status. Given the precision of a blood test to diagnose HIV, classifiers based on brain morphometry are not meant to identify infected individuals; rather the added benefit is the identification of potential biomarkers of interest to track the progression of the deleterious viral effects in the brain. In mapping the importance of each surface-based feature derived from the RF back onto the subcortical surfaces, we were able to observe a large degree

of correspondence between thresholded statistical maps and feature importance. This correspondence between importance weightings and statistically differing regions mutually validates the observed profile of changes in HIV participants as well as the potential to use these regions as biomarkers for HIV's effect in subcortical brain regions. The exclusive use of RD features moderately outperformed the exclusive use of volume as predictors, both of which outperformed the JD-only classifier though no feature-specific classifiers outperformed another at the alpha = 0.05 level of significance.

Analysis of the importance scores resulting from the random forest suggests several things. First, we observed that RD (thickness) features were on average more important than JD or volumetric features. In particular thickness of the left thalamus, left pallidum and right caudate were highly important in discerning HIV status. Patterns of importance were similar for JD features but to lesser extents than RD. The volume of the left pallidum was the single most informative feature; yet no other volumetric measures were considered important after taking into account the shape descriptors.

Because the present study is not longitudinal in design, we are unable to address questions of accelerated brain aging caused by HIV. However, we do observe widespread yet concentrated regions of atrophy in the subcortical regions of interest among HIV+ participants that are age disproportionate. The primary regions of advanced atrophy seem concentrated in the basal ganglia, thalamus and caudate. This is a departure from atrophy patterns observed in common forms of neurodegeneration such as Alzheimer's disease which principally targets hippocampal regions. However, as previously noted, increased atrophy of subcortical brain regions has been widely reported in HIV neuroimaging literature. Several studies have also observed decreased cognitive functions in vertically infected children that increase with disease

severity (Chase *et al*, 2000; Le Doare *et al*, 2012; Smith *et al*, 2006) suggesting that neurological dysfunction is a factor in infection at any age. It would be tenuous to directly compare observed differences between these age groups since study designs and protocols differ widely.

We were notably unable to identify a relationship between brain morphometry and viral load, nCD4 count, HAND status or drug abuse history. As this is a cohort of elderly subjects, many of whom were infected prior to the development of modern cART yet managed to survive, the survivorship effect may generally limit our abilities to find such associations; that is it is possible that these individuals are generally healthier. This also limits our ability to generalize these findings to a younger HIV+ population. nCD4 counts have previously been linked to lower regional brain volumes (Hua *et al*, 2013) in a younger cohort. Our lack of observed associations with HAND status also likely reflects the fact that none of our cohort had developed HAD; rather 14 had ANI while 16 had MND, far milder forms of HAND. Drug abuse history was similarly limited by the fact that few of our subjects had a history of drug abuse and those that did were distributed among different classes of drugs.

Conclusions

We have characterized patterns of abnormal brain morphometry in an elderly HIV+ cohort. The increased atrophy observed in HIV+ patients lends support to the idea that HIV contributes to age-disproportionate brain aging. Regions of atrophy were localized by vertex wise descriptions of thickness, dilation and contraction. Pronounced abnormalities were found in the medial head of the caudate, the bilateral pallidum and the putamen and the thalamus. Several other regions exhibited significant abnormalities as well. Ventricular spaces were enlarged in the HIV+ cohort. We also observed a paradoxically positive association between the TSD and the size of the right anterior pallidum that was not attributable to substance abuse history. This effect

may be a product of medication use or even the survivorship effect, however neither effect can be evaluated with this cohort as all are on stable cART and, of course, survivors. Infection status was classifiable using only subcortical morphometry with an AUC of 72.3%. Classification was driven heavily by the thickness of pallidal, thalamic and caudate surfaces. Future studies should further develop the use of these descriptors to aid in tracking the progression of HIV's effect on the aging brain.

Acknowledgements

Chapter 3 is a version of Wade BS, Valcour VG, Wendelken-Riegelhaupt L, Esmaeili-Firidouni P, Joshi SH, Gutman BA, Thompson PM. (2015). Mapping abnormal subcortical brain morphometry in an elderly HIV + cohort. *NeuroImage Clinical* **9**: 564-573.

Victor Valcour lead the parent study which contributed the data used herein. Lauren Wendelken-Riegelhaupt and Pardis Esmaeili-Firidouni aissisted in data management and acquisition. Shantanu Joshi and Boris Gutman aided in data analysis. Boris Gutman developed the shape modeling used in this study. Paul Thompson was the PI of the study.

This work was supported in part by NIH 'Big Data to Knowledge' (BD2K) Center of Excellence grant U54 EB020403, funded by a cross-NIH consortium including NIBIB and NCI and by the National Science Foundation Graduate Research Fellowship under Grant No. DGE-0707424. The clinical work was supported by grant numbers K24-MH098759, K23AG032872, P30-AI027763 (UCSF CFAR) and UL1 RR024131 (UCSF GCRC), the Larry L. Hillblom Foundation and the AIDS Research Institute at UCSF.

Conflict of interest

The other authors have no disclosures related to the study.

References

Ances BM, Ortega M, Vaida F, Heaps J, Paul R (2012). Independent effects of HIV, aging, and HAART on brain volumetric measures. *Journal of Acquired Immune Deficiency Syndromes* **59**(1944-7884 (Electronic)): 469-477.

Ances BM, Roc A, Korczykowski M, Wolf Rl, Kolson DL (2008). Combination antiretroviral therapy modulates the blood oxygen level-dependent amplitude in human immunodeficiency virus-seropositive patients. *Journal of NeuroVirology* **14**(5): 418-424.

Aylward EH, Brettschneider PD, McArthur JC, Harris GJ, Schlaepfer TE, Henderer JD*, et al* (1995). Magnetic resonance imaging measurement of gray matter volume reductions in HIV dementia. *Am J Psychiatry* **152**(7): 987-994.

Aylward EH, Henderer JD, McArthur JC, Brettschneider PD, Harris GJ, Barta PE*, et al* (1993). Reduced basal ganglia volume in HIV-1-associated dementia: results from quantitative neuroimaging. *Neurology* **43**(10): 2099-2104.

Becker JT, Maruca V, Kingsley LA, J.M. S, Alger JR, Barker PB*, et al* (2012). Factors affecting brain structure in men with HIV disease in the post-HAART era. *Neuroradiology* **54**(1432-1920 (Electronic)): 113-121.

Benjamini Y, Hochberg Y (1995). Controlling the false discovery rate- a practical and powerful approach to multiple testing. *Journal of the Royal Statistical Society* **57**: 289–300.

Berger JR, Nath A (2000). HIV dementia and the basal ganglia. *Journal of psychopharmacology* **14**(3): 214-221.

Breiman L (2001). Random Forests. *Machine Learning* **45**(1): 5-32.

Canizares S, Cherner M, Ellis RJ (2014). HIV and aging: effects on the central nervous system. *Seminars in Neurology* **34**(1098-9021 (Electronic)): 27-34.

Chang L, Cloak C, Patterson K, Grob C, Miller EN, Ernst T (2005). Enlarged striatum in abstinent methamphetamine abusers: a possible compensatory response. *Biological psychiatry* **57**(0006-3223 (Print)): 967-974.

Chang L, Lee PL, Yiannoutsos CT, Ernst T, C.M. M, Richards T*, et al* (2004). A multicenter in vivo proton-MRS study of HIV-associated dementia and its relationship to age. *NeuroImage* **23**(1053-8119 (Print)): 1336-1347.

Chang L, Wong V, Nakama H, Watters M, Ramones D, Miller EN*, et al* (2008). Greater than age-related changes in brain diffusion of HIV patients after 1 year. *Journal of NeuroImmune Pharmacology* **3**(4): 265-274.

Chase C, Ware J, Hittelman J, Blasini I, Smith R, Llorente A*, et al* (2000). Early cognitive and motor development among infants born to women infected with human immunodeficiency virus. Women and Infants Transmission Study Group. *Pediatrics* **106**(1098-4275 (Electronic)).

Chen Y, An H, Zhu H, Stone T, Smith JK, Hall C*, et al* (2009). White matter abnormalities revealed by diffusion tensor imaging in non-demented and demented HIV+ patients. *NeuroImage* **47**(1095-9572 (Electronic)): 1154-1162.

Cohen RA, Seider TR, Navia B (2015). HIV effects on age-associated neurocognitive dysfunction: premature cognitive aging or neurodegenerative disease? *Alzheimer's Research & Therapy* **7**(1758-9193 (Electronic)): 37.

Cysique L, Maruff P, Brew B (2004). Prevalence and pattern of neuropsychological impairment in human immunodeficiency virus-infected/acquired immunodeficiency syndrome (HIV/AIDS) patients across pre- and post-highly active antiretroviral therapy eras: A combined study of two cohorts. *Journal of Neurovirology* **10**(6): 350-357.

Cysique LA, Maruff P, Bain MP, Wright E, Brew BJ (2011). HIV and age do not substantially interact in HIV-associated neurocognitive impairment. *Journal of Neuropsychiatry and Clinical Neurosciences* **23**(1545-7222 (Electronic)): 83-89.

Deng H (2013). Guided Random Forest in the RRF Package. *arXiv:13060237*: 1-2.

Drevets WC (2001). Neuroimaging and neuropathological studies of depression: implications for the cognitive-emotional features of mood disorders. *Current opinion in neurobiology* **11**(0959-4388 (Print)): 240-249.

Fischl B, Salat DH, Busa E, Albert M, Dieterich M, Haselgrove C*, et al* Whole Brain Segmentation. *Neuron* **33**(3): 341-355.

Gorelick P, Scuteri A, Black SE, Decarli C, Greenberg SM, Ladecola C*, et al* (2011). Vascular contributions to cognitive impairment and dementia: a statement for healthcare professionals from the american heart association/american stroke association. *Stroke* **42**(9): 2672-2713.

Gottumukkala RV, Romero JM, Riascos RF, Rojas R, Glikstein RS (2014). Imaging of the brain in patients with human immunodeficiency virus infection. *Topics in Magnetic Resonance Imaging* **23**(5): 275-291.

Gray KR, Aljabar P, Heckemann RA, Hammers A, Rueckert D (2013). Random forest-based similarity measures for multi-modal classification of Alzheimer's disease. *NeuroImage* **65**(0): 167-175.

Gutman B, Jahanshad N, Ching C, Wang Y, Kochunov P, Nichols T*, et al* (2015). Medial Demons Registration Localizes the Degree of Genetic Influence over Subcortical Shape Variability: An N= 1480 Meta-Analysis. *International Symposium on Biomedical Imaging*.

Gutman B, Madsen S, Toga A, Thompson P (2013). A Family of Fast Spherical Registration Algorithms for Cortical Shapes. *Multimodal Brain Image Analysis* **8159**: 246-257.

Gutman B, Wang Y, Rajagopalan P, Toga A, Thompson P (2012). Shape matching with medial curves and 1-D group-wise registration. *International Symposium on Biomedical Imaging* **9**: 716-719.

Hall HI, Song R, Rhodes P, Prejean J, An Q, Lee LM*, et al* (2008). Estimation of HIV incidence in the United States. *JAMA* **300**(1538-3598 (Electronic)): 520-529.

Harezlak J, Buchthal S, Taylor M, Schifitto G, Zhong J, Daar E*, et al* (2011). Persistence of HIV-associated cognitive impairment, inflammation, and neuronal injury in era of highly active antiretroviral treatment. *AIDS* **25**(1473-5571 (Electronic)): 625-633.

Holt JL, Kraft-Terry, Chang L, Chang L (2012). Neuroimaging studies of the aging HIV-1-infected brain. *Journal of NeuroVirology* **18**(4): 291-302.

Hua X, Boyle CP, Harezlak J, Tate DF, Yiannoutsos CT, Cohen R*, et al* (2013). Disrupted cerebral metabolite levels and lower nadir CD4 + counts are linked to brain volume deficits in 210 HIV-infected patients on stable treatment. *NeuroImage Clinical* **3**: 132-142.

Jean-Paul Fouche, Neda Jahanshad, John Joska, Robert Paul, Jacqueline Hoare, Victor Valcour*, et al* (2015). The ENIGMA-HIV working group: Association of CD4 with subcortical volume in HIV-positive adults. *Organization of Human Brain Mapping* **Poster Session**.

Jernigan TL, Gamst AC, Archibald SL, Fennema-Notestine C, Mindt MR, Marcotte TD*, et al* (2005). Effects of methamphetamine dependence and HIV infection on cerebral morphology. *american journal of psychiatry* **162**(8): 1461-1472.

Le Doare K, Bland R, Newell ML (2012). Neurodevelopment in children born to HIV-infected mothers by infection and treatment status. *Pediatrics* **130**(1098-4275 (Electronic)): 1326-1344.

McBean AM, Li S, Gilbertson DT, Collins AJ (2004). Differences in diabetes prevalence, incidence, and mortality among the elderly of four racial/ethnic groups: whites, blacks, hispanics, and asians. *Diabetes Care* **27**(10): 2317-2324.

R Core Team (2014). R: A language and environment for statistical computing. R Foundation for Statistical Computing Vienna, Austria.

Robertson KR, Su Z, Margolis DM, Krambrink A, Havlir DV, Evans S*, et al* (2010). Neurocognitive effects of treatment interruption in stable HIV-positive patients in an observational cohort. *Neurology* **20;74**(16): 1260-1266.

Sacktor N, Skolasky RL, Cox C, Selnes O, Becker JT, Cohen B*, et al* (2010). Longitudinal psychomotor speed performance in human immunodeficiency virus-seropositive individuals: impact of age and serostatus. *Journal of NeuroVirology* **16**(1538-2443 (Electronic)): 335-341.

Schweinsburg BC, Taylor MJ, Alhassoon OM, Gonzalez R, Brown GG, Ellis RJ*, et al* (2005). Brain mitochondrial injury in human immunodeficiency virus-seropositive (HIV+) individuals taking nucleoside reverse transcriptase inhibitors. *Journal of NeuroVirology* **11**(4): 356-364.

Simioni S, Cavassini M, Annoni JM, Rimbault Abraham A, Bourquin I, Schiffer V*, et al* (2010). Cognitive dysfunction in HIV patients despite long-standing suppression of viremia. *AIDS* **24**(9): 1243-1250.

Smith R, Malee K, Leighty R, Brouwers P, Mellins C, Hittelman J*, et al* (2006). Effects of perinatal HIV infection and associated risk factors on cognitive development among young children. *Pediatrics* **117**(1098-4275 (Electronic)): 851-862.

Thompson PM, Dutton RA, Hayashi KM, Toga AW, Lopez OL, Aizenstein HJ*, et al* (2005). Thinning of the cerebral cortex visualized in HIV/AIDS reflects CD4+ T lymphocyte decline. *Proceedings of the National Academy of Sciences of the United States of America* **102**(0027-8424 (Print)): 15647-15652.

Towgood KJ, Pitkanen M, Kulasegaram R, Fradera A, Kumar A, Soni S*, et al* (2012). Mapping the brain in younger and older asymptomatic HIV-1 men: frontal volume changes in the absence of other cortical or diffusion tensor abnormalities. *Cortex* **48**(1973-8102 (Electronic)): 230-241.

Vink D, Aartsen MJ, Comijs HC, Heymans MW, Penninx BW, Stek Ml*, et al* (2009). Onset of anxiety and depression in the aging population: comparison of risk factors in a 9-year prospective study. *The American Journal of Geriatric Psychiatry* **17**(8): 642-652.

Tables

Table 3-1. Demographic and Clinical Characteristics

	Patients, N = 63	**Controls, N = 31**
Demographics		
Age, mean (SD), y	64.68 (4.57)	65.35 (2.21)
Gender (M/F)	61/2	27/4
Adjusted education, years*	16.09 (2.25)	17.53 (2.09)
Clinical Information		
CD4, mean (SD), cells/mm^3	516.44 (212.30)	--
Nadir CD4, mean (SD), cells/mm^3	204.96 (154.85)	--
Time since diagnosis, mean (SD), y	20.39 (6.31)	--
Viral load, mean (SD), copies/mm^3	16,380.58 (76,418.68)	--
Detectable viral load, yes/no	24/39	--
Receiving cART, yes/no	63/0	--
History of diabetes	8	0
History of depression*	28	8
APOE Allele, yes/no/unknown	12/51/0	6/13/12
Cognitive Information		
ANI	14	--
MND	16	--
HAD	0	--
WAIS Score, mean (SD)*	48.77 (10.73)	57.27 (7.48)
WRAT Score, mean (SD)*	64.05 (4.26)	66.50 (1.93)
Substance Abuse History	none/recent/remote	
Marijuana	61/0/2	--
Cocaine	55/0/8	--
Crack	62/0/1	--
Meth	57/0/6	--
Alcohol	50/0/13	--

Abbreviations: ANI = Asymptomatic Neurocognitive Impairment; MND = Mild Neurocognitive Disorder; HIV-associated Dementia. *Significant difference between HIV status. WAIS = Wechsler Adult Intelligence Scale; scores available for N=57 patients and N=22 controls. WRAT = Wide Range Achievement Test; scores available for N=57 patients and N=20 controls.

Figures

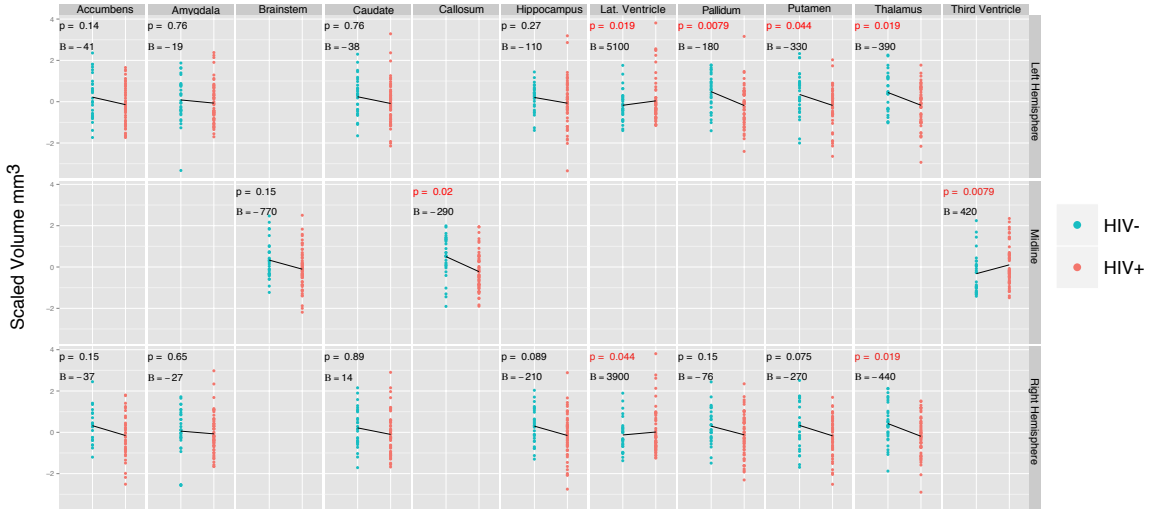

Figure 3-1. Scatterplot of volumetric differences between HIV+ and HIV- participants. The plots are divided into rows showing structures in the left hemisphere (top), midline (middle) and right hemisphere (bottom). All plots have been centered and scaled. The HIV status coefficient (in mm^3) resulting from Equation (1) is given for each plot. Volumetric differences that survive FDR correction are highlighted in red.

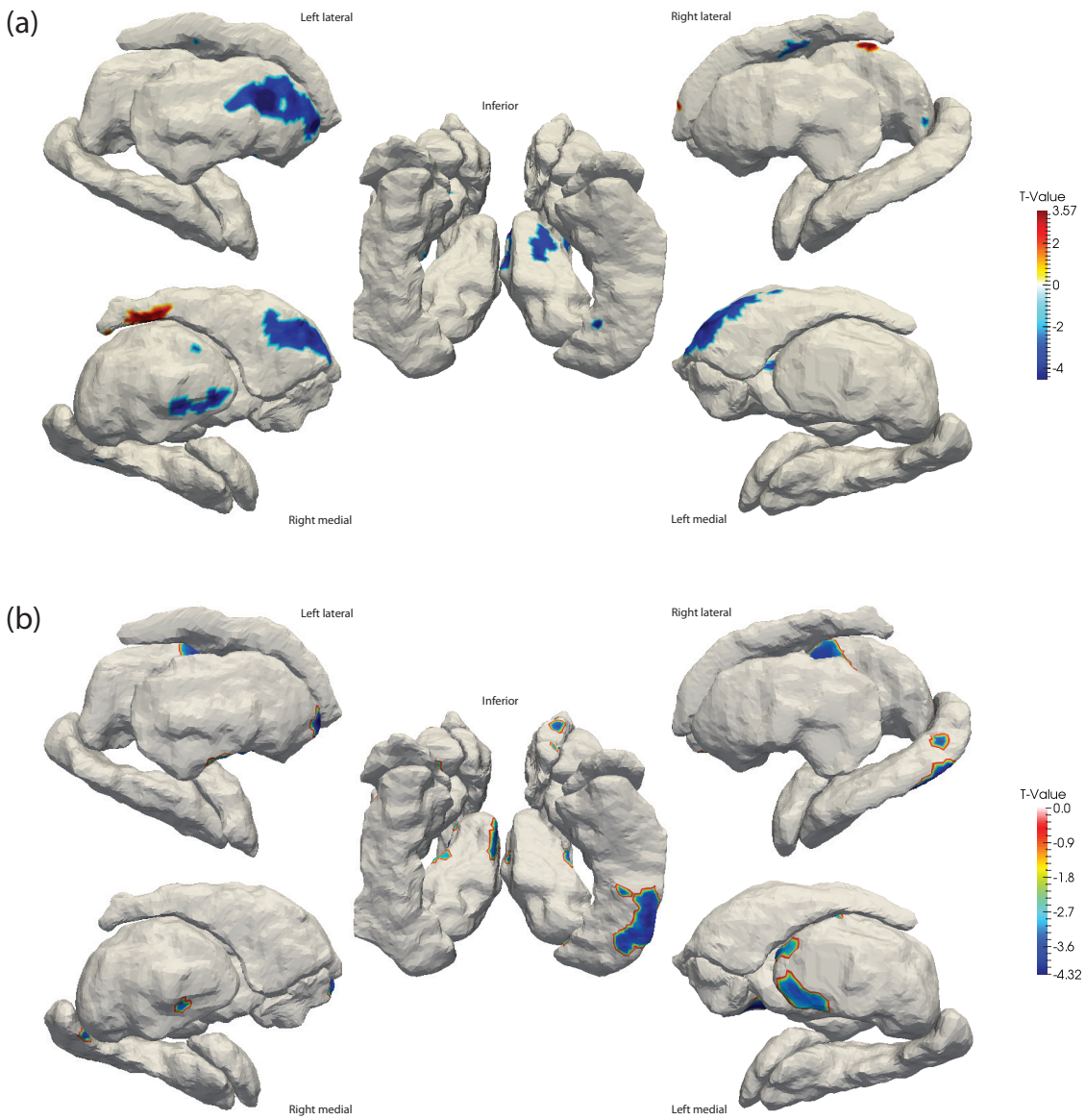

Figure 3-2. FDR-thresholded t-value maps of the HIV+ vs. HIV- contrast. (a) maps the significant differences in RD while (b) maps significant differences in JD. Images are shown in radiological orientation (i.e. left-right flipped), orientations are provided beside each set of surfaces.

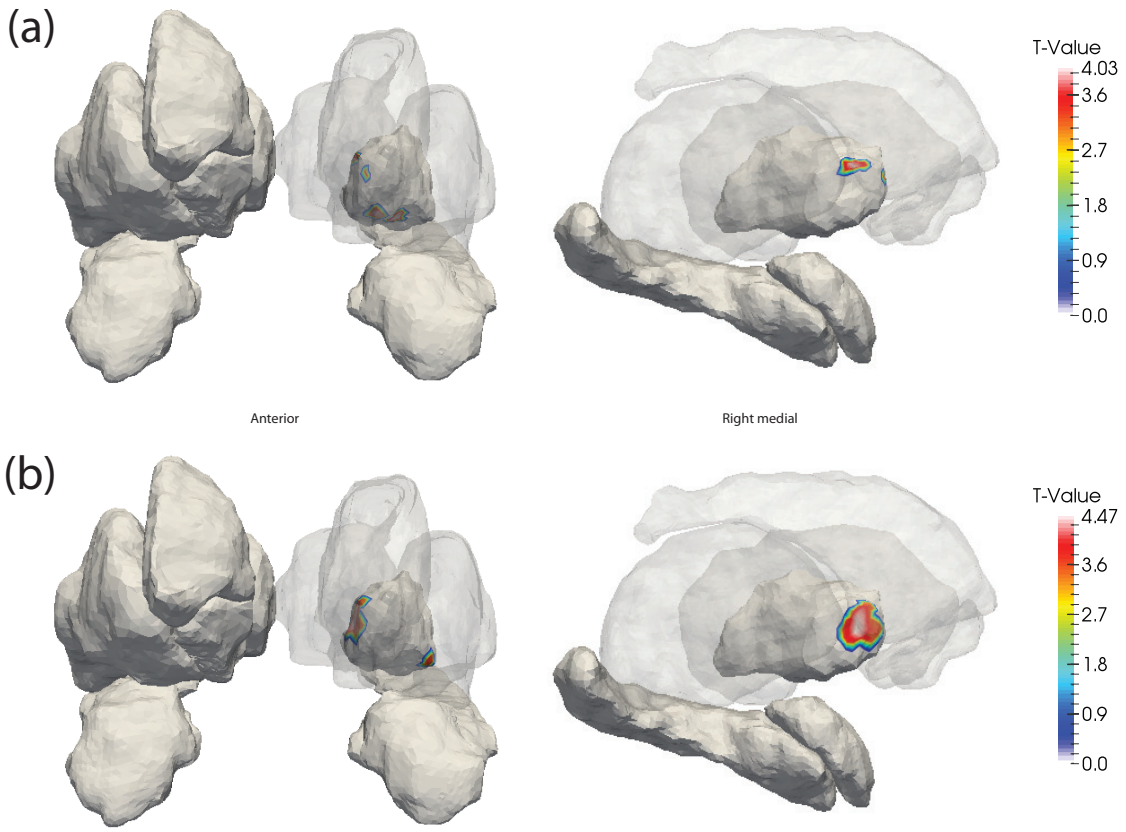

Figure 3-3. FDR-thresholded t-value maps of the association between TSD and (a) RD and (b) JD. Images are in radiological orientation (i.e. left-right flipped). The first column shows an anterior view while the second is the medial view of the right hemisphere structures.

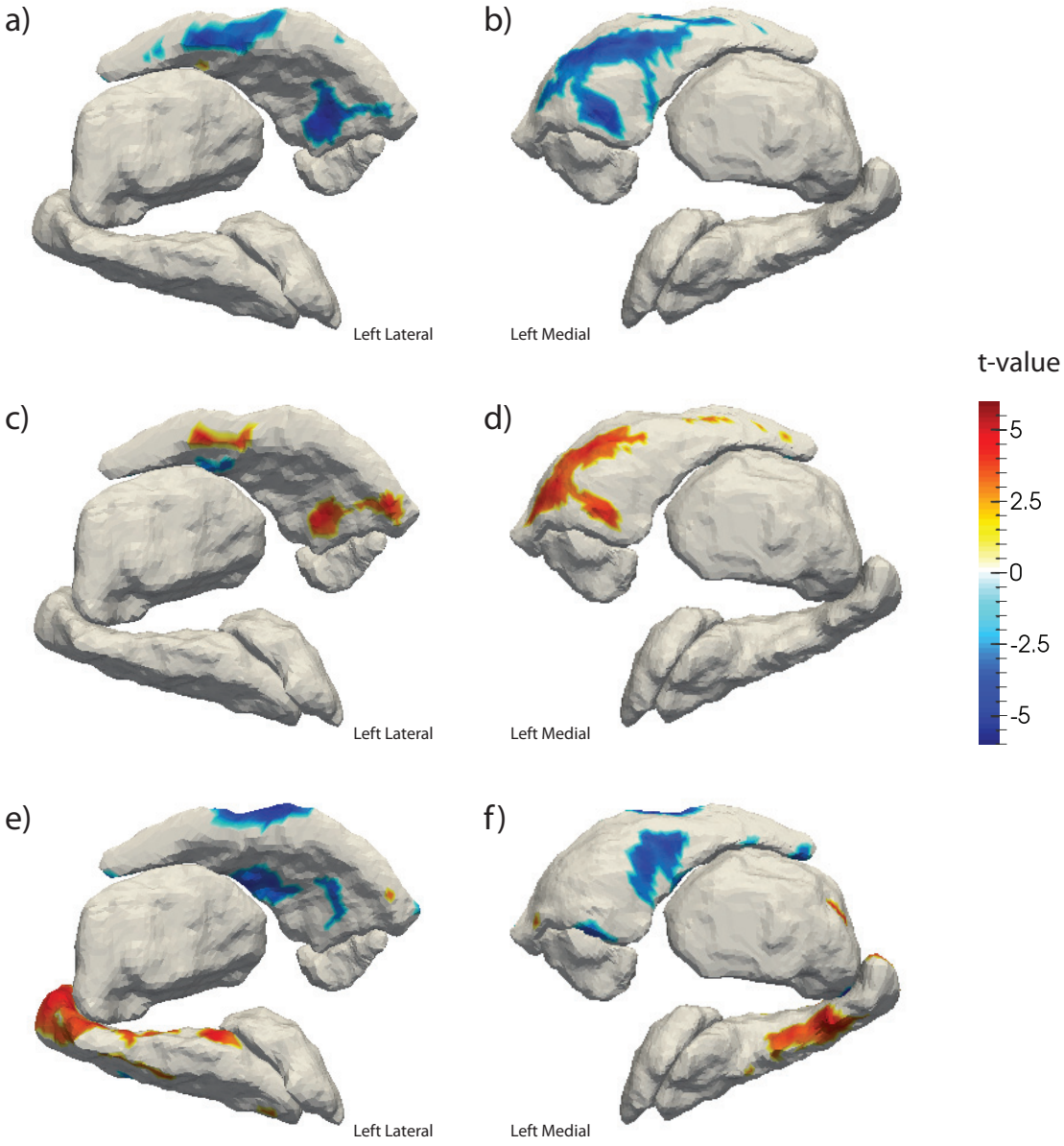

Figure 3-4. FDR-thresholded t-value maps of (a-b) association of thickness and the interaction of WAIS score and HIV Status, (c-d) the main effect of WAIS on thickness and (e-f) the association of WAIS and thickness within the HIV+ cohort only.

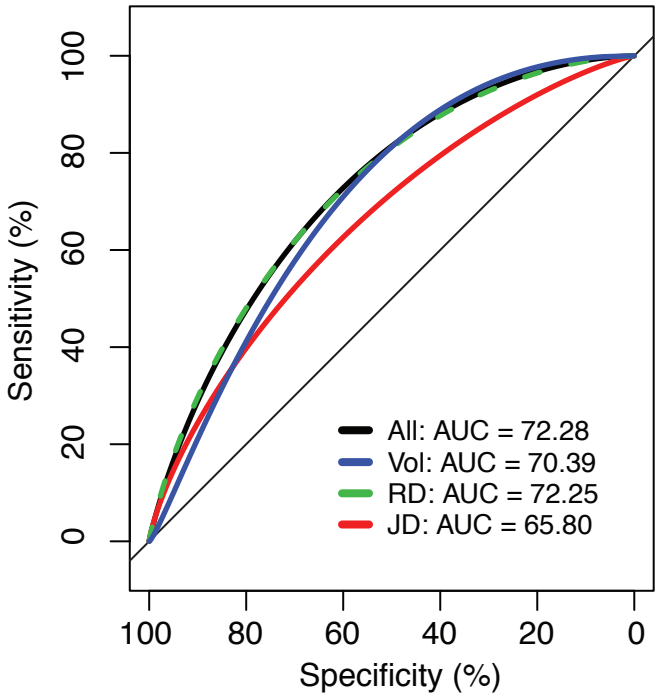

Figure 3-5. ROC curves and associated AUC values for random forest classification using the full set of morphological features. ROCs for feature subsets are also provided.

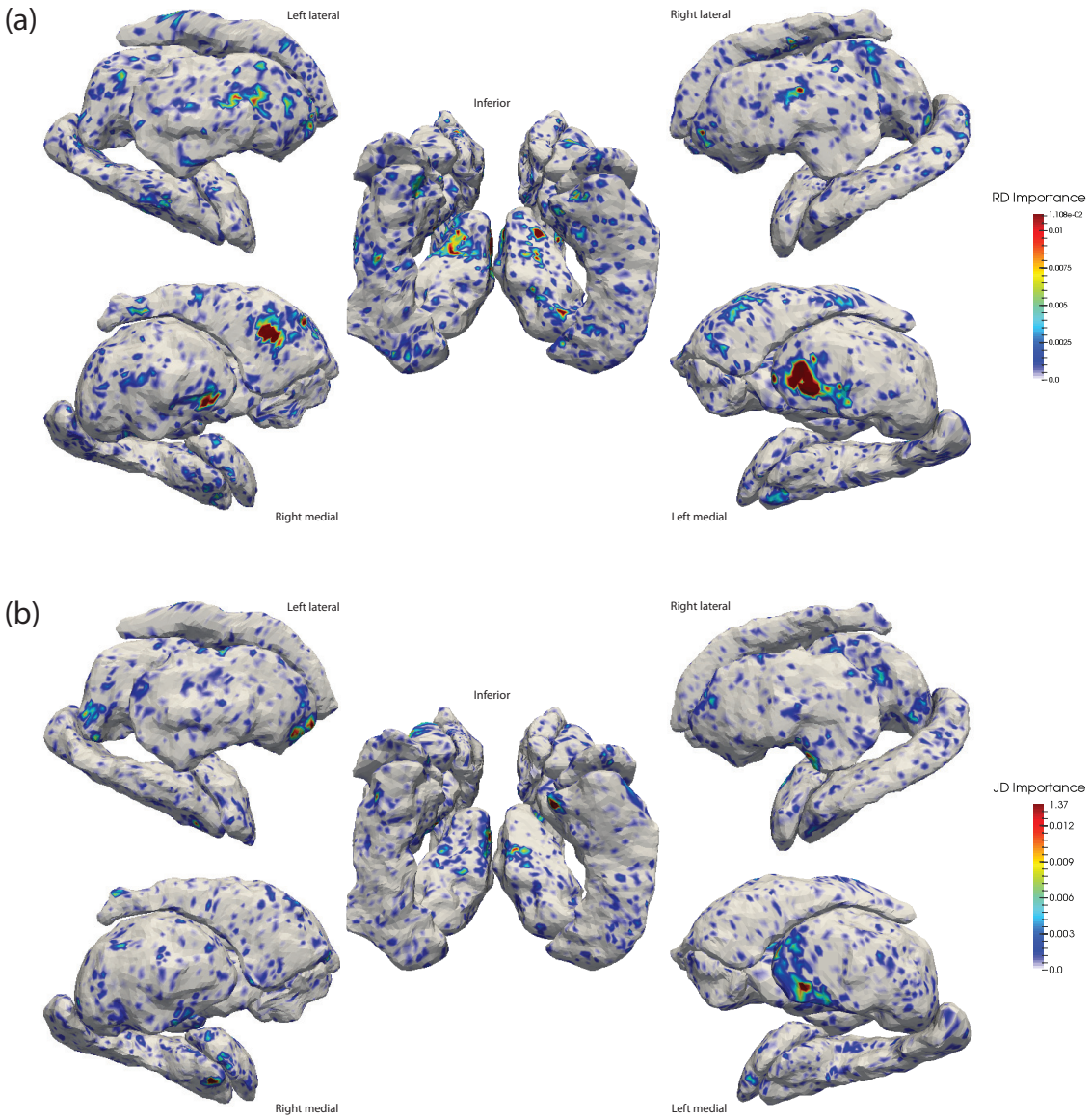

Figure 3-6. Mapping of random forest importance scores in the classification of HIV status to subcortical surfaces. As all features were included in the same RF model, their importance is with respect to all other features. (a) RD and (b) JD feature set importance scores. Images are in radiological orientation (i.e. left-right flipped), orientations are provided beside each set of surfaces.

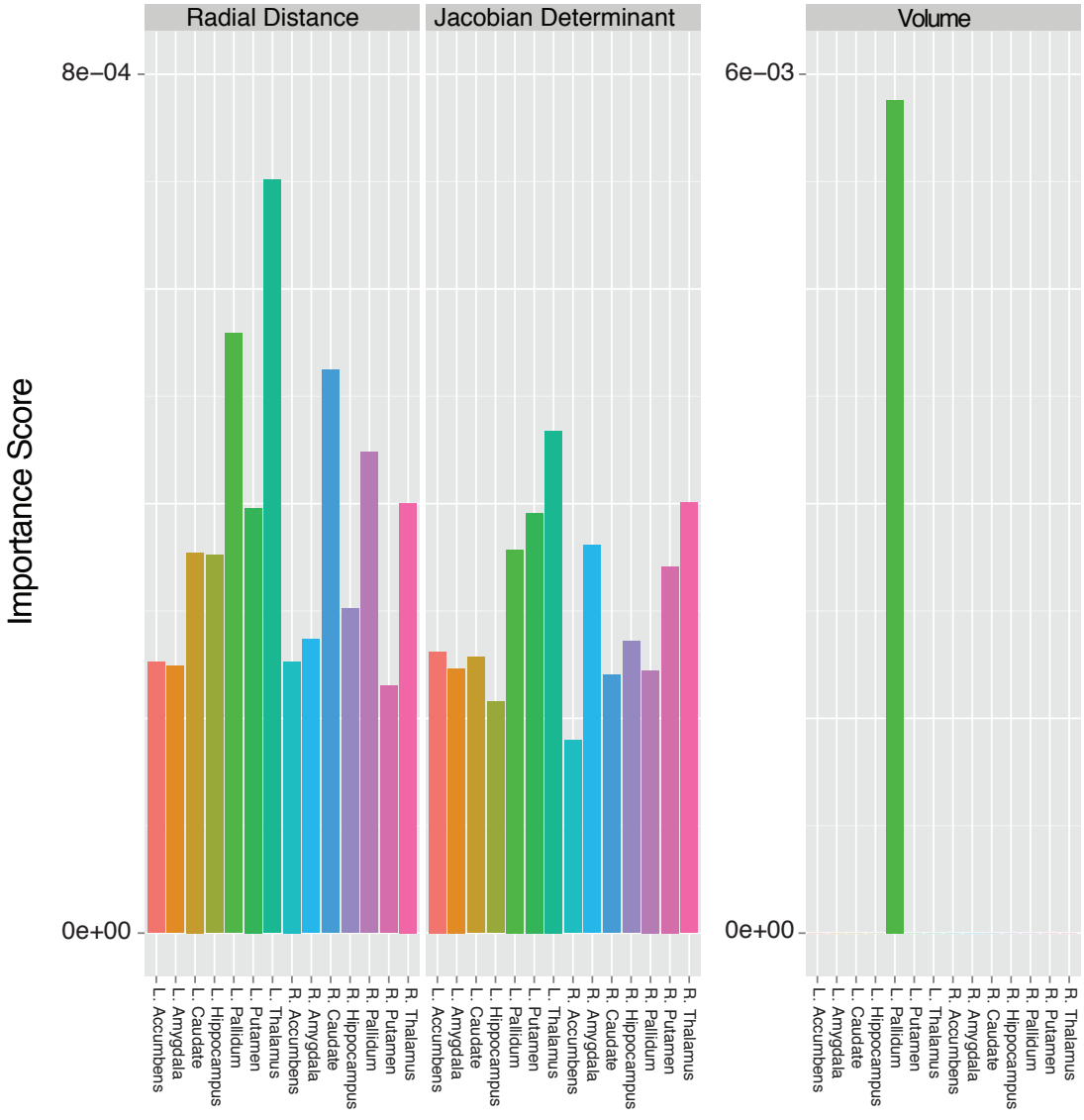

Figure 3-7. Average random forest importance scores by region and feature set.

Chapter 4: Mapping Longitudinal Subcortical Brain Morphometry in Children with HIV[3]

The trajectory of brain development in perinatally-infected HIV+ children is poorly understood and neurodevelopmental measures continue to demonstrate altered trajectories despite availability of combination antiretroviral therapy (cART). Subcortical and cortical atrophy are widely reported in adults; yet, corresponding characterizations of infected pediatric cohorts remains unclear. Using surface-based shape and volumetric analyses, we mapped subcortical morphometry in 43 HIV+ (mean age, 11.09 years) and 54 HIV- (11.06 years) Thai children who underwent structural magnetic resonance imaging at baseline and approximately 52 weeks later. We modeled cross-sectional and longitudinal abnormalities of the accumbens, amygdala, putamen, pallidum, thalamus, caudate and hippocampus related to HIV and cART status, current CD4 count and viral load using mixed and fixed effects models. Smaller baseline size of the bilateral pallidum was observed in HIV+/cART+ relative to HIV- controls whereas the thickness of the putamen, amygdala and thalamus was increased in cART-naïve children. Accelerated gains in the thickness of the right lateral pallidum and surface area of the left anterior accumbens were observed in the HIV+ cohort. Among HIV+ children we observed unexpected inverse associations between the shape and volume of the left pallidum and current CD4 counts that may reflect moderated inflammation in more well-preserved or recovered immune systems. Our findings corroborate reports in adult cohorts of the basal ganglia's vulnerability to HIV infection and suggest that infection also affects pediatric brain development.

[3] The content of this chapter is currently under review in the journal Human Brain Mapping.

Introduction

Perinatally acquired HIV infection is a major concern in the developing world. Long-term survival and quality of life of children perinatally infected with HIV has improved dramatically with better access to combination antiretroviral therapy (cART). Pediatric HIV-related encephalopathy has decreased dramatically in the cART era (Patel *et al*, 2009; Raskino *et al*, 1999; Shanbhag *et al*, 2005), down to 1.6% from a prevalence of 76% prior to cART (Chiriboga *et al*, 2005; Cooper *et al*, 1998; Epstein *et al*, 1986; Patel *et al*, 2009; Tepper *et al*, 1998). However, as the number of chronically-infected children increases, there is a need to understand how HIV may alter early brain development. Despite sustained cART regimens, HIV infection is known to lead to cognitive and fine motor impairments (Brew, 2004; Heaton *et al*, 1995; Sacktor *et al*, 2002; Van Rie *et al*, 2008) that, in adults, are commonly associated with degeneration of regions of the basal ganglia, associated white matter and cortical regions (George *et al*, 2009; Safriel *et al*, 2000).

We and other groups have reported abnormal cortical and subcortical brain morphometry in HIV+ adult cohorts related to HIV serostatus and HIV-related clinical factors such as CD4 t-cell count, viral load and reception of cART (Ances *et al*, 2012; Becker *et al*, 2012; Fennema-Notestine *et al*, 2013; Jernigan *et al*, 2011; Kallianpur *et al*, 2013; Ragin *et al*, 2015; Wade *et al*, 2015; Wilson *et al*, 2015). HIV crosses the blood-brain barrier and invades the central nervous system rapidly after infection (Epstein and Gelbard, 1999; Li *et al*, 2014), typically via infected monocytes during chronic disease (Gartner, 2000; Kim *et al*, 2003; Koenig *et al*, 1986) which subsequently produce proinflammatory cytokines such as TNF that additionally cause microglia and astrocyte activation (Hong and Banks, 2015). Astrocyte and microglia activation commonly result in excitotoxicity through their release of excitotoxic amino acids, chemokines and

cytokines (Gendelman *et al*, 1994; Langford and Masliah, 2001; Zahr *et al*, 2014). Chronic inflammation resulting from this confluence of underlying processes is considered the primary mechanism for HIV-related neurodegeneration though other mechanisms may include disrupted metabolic processes, and even neurotoxic side effects of prolonged cART exposure (Canizares *et al*, 2014). Additionally, while cART effectively reduces viral replication it does not restrict the early production of Tat protein (Anderson *et al*, 2002; Kure *et al*, 1990; Puccini *et al*, 2015) which, when replicated throughout the CNS, continues to produce cytokines and chemokines which cause further inflammatory responses (Ellis *et al*, 2007; Lu *et al*, 2011; Masliah *et al*, 1996).

As well as the observed effects of cART, several clinical markers have been related to both HIV infection and cognitive performance. Higher HIV RNA (viral load) and lower nadir CD4 cell counts have repeatedly been linked to more impaired cognitive performance (Martin *et al*, 2006; Nachman *et al*, 2012; Smith *et al*, 2012; Wood *et al*, 2009). In a study of over 200 HIV+ adults, lower regional brain volumes were associated with lower nadir CD4 counts, though current CD4 count has been differentially associated with brain integrity with some reporting no associations (Hua *et al*, 2013) and others reporting somewhat counterintuitive inverse associations between CD4 count and gray and white matter volumes in people with HIV (Jernigan *et al*, 2011).

Most studies of HIV-related neurodegeneration, as previously discussed, have reported on abnormalities in adult cohorts, with considerably fewer studying the effects of pediatric infection. In a cohort of 40 HIV+ youths, Uban reported globally reduced fractional anisotropy in the presence of increased mean and radial diffusivity among perinatally infected relative to uninfected youths (Uban *et al*, 2015). More severe infection was associated with reduced

fractional anisotropy of the right inferior fronto-occipital and left uncinate fibers. Higher peak viral loads were also inversely associated with working memory performance among the HIV+ cohort. In a study comparing developmental outcomes of HIV exposed but uninfected (HEU) to HIV unexposed and uninfected (HUU) children Jahanshad reported no volumetric or diffusion-based differences between HEU and HUU children (Jahanshad *et al*, 2015). A recent study of 50 children aged 6 – 15 years receiving cART reported decreased fractional anisotropy in association with second-line cART reception, increased mean diffusivity with respect to increased viral load as well as increased axial diffusivity in children with higher viral loads as well as those on second-line cART (Hoare *et al*, 2015). Increased radial diffusivity was additionally associated with lower CD4 counts. In a review of existing literature on perinatally HIV infected children, Laughton reported generally reduced cognitive performance among HIV+ children including reduced processing speed and visual spatial performance (Laughton *et al*, 2013). Puthanakit reported on 284 Thai and Cambodian children, of which the current study is a subset, observing that neurodevelopmental outcomes as measured by Beery Visual Motor Integration, Purdue Pegboard, Color Trails and Child Behavioral Checklist, Wechsler Intelligence Scale and Stanford Binet Memory test did not significantly differ between those with early ART initiation (i.e. when CD4 counts were 15-24%) or those who were deferred (when CD4 < 15%) (Puthanakit *et al*, 2013). However, both early and deferred enrollees performed worse than HIV- children on the Beery Visual Motor Integration, Binet memory and Child Behavioral Checklist and had lower full-scale IQ scores.

In the current study we investigate longitudinal and cross sectional neurodevelopment in a cohort of 43 perinatally-infected HIV+ and 53 HIV-uninfected Thai children between the ages of 6 and 16 from Bangkok and Chang Mai, Thailand, who constitute a subset of the children

reported on previously in the Pediatric Randomized to Early versus Deferred Initiation in Cambodia and Thailand (PREDICT) study (Puthanakit *et al*, 2012). Our analysis spans an approximate one-year timeframe and aimed to determine whether HIV seropositivity, reception, timing or duration of cART, baseline CD4 count and baseline viral detectability are related to developmental trajectories of subcortical brain structures. Importantly, because participants were enrolled to cART based on their CD4 counts being either between 15-24% or below 15%, as in the PREDICT parent study, we do not separately model nadir CD4 count as it is implicitly synonymous with the current CD4 count. In order to capture both gross and potentially subtle abnormalities in developmental trajectories we model both the volume and high-dimensional shape-based characteristics of the accumbens, amygdala, caudate, hippocampus, pallidum, putamen and thalamus using a series of both fixed and mixed effects regression models to capture the contributions of HIV positivity and interactions between clinical factors to subcortical brain development. These high-dimensional shape features, specifically local thickness and relative surface area dilation, have previously been successfully leveraged to model abnormal morphometry in elderly HIV+ individuals relative to age-matched controls (Wade *et al*, 2015), characterize subcortical morphometry in patients with major depressive disorder receiving electroconvulsive therapy (Wade *et al*, 2016), identify biomarkers of Alzheimer's disease (Gutman *et al*, 2015c) and identify the degree of genetic heritability of basal ganglia and limbic structures' morphometry (Gutman *et al*, 2015b).

We hypothesized that the trajectories of subcortical structures in HIV-infected children would be diminished, and structures will be slower to develop, relative to uninfected children and that more extreme clinical measures such as higher viral RNA or lower CD4 counts would be associated with more severe morphological abnormalities. We hypothesized that the baseline

volumes of subcortical structures will be generally reduced in HIV+ children. Additionally, we expected that differences in developmental trajectories associated with HIV status, cART status, or differences associated with various clinical measures may be subtle or localized in particular regions of structures and therefore detected more readily by highly sensitive shape-based rather than traditional global volumetric measures. In addition to the main effects of HIV and cART status as well as HIV-related clinical measures, we explored differential patterns of brain morphometry between HIV- versus HIV+/cART+ and HIV- versus HIV+/cART- children. In this association we expected to observe more pronounced volumetric reductions in HIV+/cART- children than HIV+/cART+ relative to controls. To our knowledge this is the first study reporting on longitudinal shape-based abnormalities in an HIV+ pediatric cohort.

Methods

Participants

A sample of 43 HIV+ (baseline age = 11.09 +/- 2.36; 20 female; 32 on stable cART) and 54 HIV- (baseline age = 11.06 +/- 2.79; 31 female) Thai participants were recruited as part of the ongoing study of HIV-infected children, known as PREDICT: Pediatric Randomized to Early versus Deferred Initiation in Cambodia and Thailand (Puthanakit *et al*, 2013; Puthanakit *et al*, 2012). **Table 4-1** outlines the participants' demographic and clinical characteristics at the baseline time point. The HIV+ children were initially selected for the parent (PREDICT) study due to having remained cART-naive at the time of enrollment and randomization, which occurred between 2005 and 2007. For this imaging analysis, all participants met the following inclusion criteria: (1) age <18 years, (2) able to tolerate MRI, and (3) written informed consent signed by a caregiver and able to provide assent for participants 7 to 12 years of age. Exclusion criteria included prior or current brain infection, neurological or psychiatric disorder, any

congenital abnormality or head injury with a loss of consciousness. Participants were imaged at King Chulalongkorn Memorial Hospital in Bangkok, Khon Kaen University and Chiang Mai University Hospital in Chiang Mai, Thailand. The Institutional Review Boards (IRBs) of each study site, the University of California San Francisco, and the University of Southern California, in Los Angeles each approved the study.

Image acquisition

Participants underwent structural magnetic resonance imaging at two time points: baseline and approximately 52 weeks later (median = 52.71 weeks; range = 31.14 to 116.71 weeks to follow-up). Initially, all participants were assessed at three time points where the third time point was also approximately 52 weeks following time point 2. However, the average age of HIV+ participants was a full year higher than controls. Therefore, we decided to assess the true baseline and 52 week follow-up among HIV+ participants and the actual second and third time points for the control cohort in order to match ages. From here forward baseline and follow-up refer to time points 1 and 2 for HIV+ participants and time points 2 and 3 for controls.

Whole brain structural T1-weighted MRI was performed on GE 1.5 tesla scanners at both study sites using the following protocol: axial plane, 3D SPGR images with a minimum TE at full echo, TR = 11.2 ms, slice thickness = 1.0 mm; 256x256 imaging matrix. Quality assurance of the MRI acquisitions was performed throughout the study. In order to quantify scanner drift across time points both a structural and human phantom were acquired periodically. Additionally, trained technicians manually reviewed all T1 scans and repeated scans with excessive motion artifact.

Morphological descriptors

Previously validated FreeSurfer (Fischl *et al*, 2002) workflows, including non-brain tissue removal, intensity normalization and automated volumetric parcellation based on probabilistic information from manually labeled training sets, were used to segment the bilateral thalamus, putamen, pallidum, amygdala, accumbens, caudate and hippocampus from the raw MRIs. All segmentations were visually inspected following publically available ENIGMA protocols: http://enigma.ini.usc.edu/protocols/imaging-protocols/ to ensure their quality.

To define shape descriptors on the subcortical surfaces, each surface had to be parameterized (i.e. a 3D coordinate mesh, or grid, had to be imposed). The parameterization of each surface was obtained using the medial "Demons" framework detailed in (Gutman *et al*, 2015a; Gutman *et al*, 2012). Briefly, each surface was conformally mapped to the spherical domain and rigidly rotated to a probabilistic atlas. Each segmentation was warped to a spherical template using Spherical Demons (SD) (Gutman *et al*, 2013) on the basis of curvature. At this stage two surface-based functions were defined: (1) the global orientation function used to define the orientation of the surface, and (2) the local thickness of the surface with respect to a skeletonization or the surface "medial core." Finally, SD was implemented again using both the newly defined medial core, in conjunction with surface-based curvature to match each surface to the atlas.

From this mapping process, two shape features were defined at each vertex: (1) radial distance (RD), which is a proxy for the structure's local thickness, and (2) the log of the Jacobian determinant (JD) which indicates regional surface area expansion or contraction. Across all 14 subcortical surfaces, there were a total of 27,120 vertices. **Figure 4-S1** maps the subcortical structures investigated with shape analysis in this study and outlines the number of vertices constituting each surface.

Statistical methods

Mixed effects regression was used to model associations between morphometry and HIV-related factors over time while accounting for the correlation structure across the two time points resulting from repeated participant measures. The outcome of these models was one of the volume or locally defined RD or JD value. All longitudinal models covaried for participant age, sex, days to follow-up (which differed significantly by HIV status) and intracranial volume in the presence of a random participant-level effect term. Main effects of interest were HIV status (dichotomous), cART status (dichotomous), viral detectability (a viral load above 50 copies per ml was considered detectable and modeled dichotomously among HIV+ participants), current CD4 t-cell count (continuous) and cART initiation timing: initiation at baseline versus after baseline but before follow-up (among HIV+ participants). We additionally explored longitudinal associations between morphometry and interactions between HIV and cART status, HIV and cART status by CD4 count, HIV status by cART timing CD4 count by viral detectability and CD4 count by cART status. To establish the significance of the effect of interest in the longitudinal mixed effects models, a likelihood ratio test was conducted between the full model which included all covariates and the effect of interest with an interaction of time point and a nested null model defined using the above terms, aside from the effect of interest by time point interaction term; the effect of interest and time point were instead designated independent terms in the null model. Note that CD4 counts and viral loads were all baseline measurements only and not acquired at follow-up.

Multiple linear regression was used to model baseline associations of HIV status, cART status, viral RNA detectability and CD4 cell count with subcortical morphometry. Interactions explored longitudinally were additionally explored at baseline. Additional interactions between

CD4 count and viral detectability were investigated in their association with morphometry at baseline. These cross-sectional models also covaried for age, sex and ICV. For all models we explored additionally covarying for cART status, CD4 count, viral detectability and days to follow-up time point (for longitudinal models) to rule out confounding effects.

All models were adjusted for multiple comparisons using the standard false discovery rate (FDR) method with a false-positive rate of 5% ($q = 0.05$) (Benjamini and Hochberg, 1995). FDR was performed separately for volumetric and shape-based tests. For the family of volumetric tests, FDR was applied to the set of all subcortical structures. For shape analyses we applied an FDR correction within the family of all tests performed on a single surface correcting for separate tests within each surface.

Results

Demographics

HIV+ and HIV- participants did not differ significantly by age (T = 0.05, df = 94.62, p = 0.95) or sex ($\chi^2 = 0.74, df = 1, p = 0.38$). CD4 counts differed significantly by HIV status (mean HIV- = 965.70, sd = 308.19, mean HIV+ = 727.93, sd = 325.29; T = -3.66, df = 87.90, p = 0.0004). Days to follow-up differed significantly between diagnostic contrasts (T = 4.83, df = 47.99, p < 0.0001) with the average days to follow-up for HIV- being 365.11 (sd = 41.72) and HIV+ being 472.69 (sd = 140.84).

There were no significant differences in age, sex or days to follow-up between cART+ and cART- HIV+ participants. Rates of detectable viral loads were significantly different by cART status with cART- children having a higher rate of detectable levels than those who were on cART ($\chi^2 = 10.5, df = 1, p = 0.0011$). 3 cART+ children had detectable levels while the remaining cART+ participants had undetectable levels. Meanwhile 6 cART- children had

detectable viral loads while the remaining cART- participants did not. CD4 counts differed significantly by cART status (mean cART+ = 853.53, sd = 270.80, mean cART- = 362.54, sd = 140.49; T = 7.68, df = 33.97, $p < 0.00001$).

No significant differences in age or sex were present between participants initiated to cART at baseline (N=32) versus those enrolled between baseline and follow-up (N=9). CD4 count, which was only measured at baseline, differed significantly by cART initiation timing (T = 6.98, df = 29.91, $p < 0.0001$) with those initiated at baseline having higher counts (mean = 837.89, sd = 306.31) than those initiated between baseline and follow-up (mean = 375.44, sd = 133.59).

HIV status

Significant shape variation was observed between HIV+ and HIV- participants. At baseline regional thickness (RD measure) of the right medial pallidum was decreased in the HIV+ cohort while regional RD was increased in the right medial amygdala. The surface area (JD measure) of the left lateral pallidum was reduced while the JD of regions within the right amygdala were both increased and decreased in regions in the HIV+ cohort relative to controls. Significant baseline shape variation associated with HIV status is illustrated in **Figure 4-1**(a).

Additional interactions between HIV and cART status were present at baseline and illustrated in **Figure 4-1**(b). In this set of comparisons HIV- participants are the reference category and all differences are with respect to cART status among HIV+ participants. The JD of the left medial amygdala was increased among HIV+/cART- relative to the HIV- cohort. In addition, the RD of the left superior putamen, left anterior amygdala, right superior and inferior putamen and right superiorlateral thalamus were increased among HIV+/cART- participants relative to the HIV- cohort. Shape-based differences between HIV- and HIV+/cART+

participants were also present. Specifically, the bilateral medial pallidum RD was reduced and the JD of the right medial amygdala was increased among the HIV+/cART+ relative to HIV- participants.

While no main effect of cART was detected, as discussed subsequently, the significant increases in the JD of the right amygdala among HIV+ participants relative to HIV- appears to be driven primarily by HIV+/cART+ participants. Similarly, the reduction in the right medial pallidum RD among HIV+ participants seems driven by HIV+/cART+ participants as well given that this effect is present only among the cART+ group. Reductions of bilateral pallidum shape measures remained significant after correcting for CD4 count but increases in RD and JD were not present after correcting for CD4 count. Partial F-tests between regression models with and without CD4 count were non-significant for these regions, however, suggesting that CD4 count does not significantly account for the variance in these regions' shapes above and beyond HIV status.

Longitudinally, the increase in the gain of thickness of the right lateral pallidum was significantly increased in the HIV+ group. The rate of surface area increase in the left anterior accumbens was also significantly increased in the HIV+ group, relative to controls. Longitudinal shape differences by HIV status are depicted in **Figure 4-2**(a-b). No significant interactions between HIV and cART status was present longitudinally. These longitudinal associations survived while covarying for days to follow-up.

No significant volumetric variation was observed either at baseline or longitudinally in association with HIV status, however, **Figure 4-S2**(a) plots the percentage of volumetric differences at both time points by HIV status. Though not statistically significant, strong numerical differences were observed at baseline: The total callosum volume was reduced by

13%, the right caudate increased by 8% and the right pallidum reduced by 4% in the HIV+ group relative to controls.

cART status

The JD (surface area) of the right lateral putamen significantly reduced over time among participants enrolled on cART at baseline relative to participants initiating cART between baseline and follow-up (**Figure 4-2**(c)). Because there was a significantly higher CD4 count among those enrolled at baseline we included CD4 as a covariate in this model; the significance of the main effect of initiation timing remained. Significant interactions between cART status and CD4 count were observed and are outlined in section *CD4 count,* below. Otherwise cART status was not a significant main effect associated with shape or volumetric measures. **Figure 4-S2**(b) plots the percentage of volumetric differences between HIV+ children receiving and those not receiving cART. We additionally observed no associations between the percent of a participant's age enrolled on cART and subcortical morphometry in cross-sectional or longitudinal frameworks.

HIV RNA detectability

When modeled longitudinally, there were significant associations between the JD and the detectability of viral RNA within HIV+ participants. Here we observed regions of both significantly increased and decreased rate of gain in surface area in the right accumbens of participants with detectable viral RNA relative to those with undetectable levels. **Figure 4-S3**(a) maps this association. Additionally, there was a significantly increased rate of loss of right lateral ventricle volume ($T = -3.82$, $p < 0.05$) among HIV+ participants with detectable viral loads relative to those without. **Figure 4-S3**(b) shows an interaction plot between right lateral ventricle volume over time stratified by viral detectability. These shape and volume association survived

after covarying for the effects of CD4 count and cART status in addition to the standard age, sex and ICV covariates. No significant baseline associations between shape or volume were observed with respect to viral detectability.

CD4 count

At baseline, there were significant reductions in both the thickness (RD) and surface area (JD) of the left medial and lateral pallidum among HIV+ participants with higher CD4 counts. We observed a significant HIV by cART status interaction with CD4 count in the RD of the left pallidum as well in which the RD of the HIV+/cART+ cohort decreased significantly relative to the increase in RD among HIV- participants at higher CD4 counts; HIV+/cART- children did not reveal a significant interaction. No such interactions were present for JD measures. **Figure 4-3**(a-b) illustrates these associations. Also at baseline, the volume of the left pallidum was significantly associated with the interaction of HIV status and CD4 cell count ($T = -3.725$, $p < 0.05$). Specifically, there was a strong inverse association between left pallidum volume and CD4 cell count within the HIV+ cohort ($T = -3.54$, $p < 0.05$) with a 2.5% reduction in the left pallidum volume for extra 100 CD4 cells/mm^3. In contrast there was a non-significant but positive association between the left pallidum volume and CD4 cell count within the HIV- cohort ($T = 1.29$, $p > 0.05$) with a 0.76% increase in left pallidum volume for every extra 100 CD4 cells/mm^3. This differential association is shown in the interaction plot in **Figure 4-3**(c).

An association of HIV by cART status by CD4 count was also present in the right superior caudate in which the local JD decreased significantly more at higher CD4 counts among HIV+/cART- than HIV- participants (**Figure 4-3**(d)). No direct interaction of HIV status and CD4 count was present in this region.

Longitudinally, there was a significant association between CD4 cell count and the JD of the left putamen. Here, the surface area in the superior left putamen reduced significantly more rapidly in HIV+ participants with higher baseline CD4 cell counts. This longitudinal association is depicted in **Figure 4-3**(e).

Discussion

In this study we investigated the effects of HIV and cART status as well as clinical measures associated with HIV infection on subcortical brain morphometry in perinatally HIV-infected Thai children and age-matched uninfected controls. To sensitize the analyses to subtle effects, we used a combination of volumetric and shape-based approaches across two time points spanning approximately one year.

The primary findings of this study can be parsed into those observed at baseline or longitudinally. At baseline we observed a significant reduction in the thickness of the right medial pallidum, the surface area of the left lateral pallidum and a region of the right amygdala associated with HIV positivity. We also observed increased surface area of regions of the right amygdala in HIV+ participants. Additional regions' shapes varied as a function of the interaction of HIV and cART status. Notably, HIV+/cART+ children exhibited principally increased regions of thickness and surface area. Specifically, the surface area of the left posterior medial amygdala was increased in this cohort relative to HIV- children as was the thickness of regions of the bilateral putamen, left amygdala and right thalamus. Meanwhile, some of the observed primary effects of HIV status appear to be driven by cART reception: both the reduced thickness of the right medial pallidum and increased thickness of the right medial amygdala are shown to be present only in HIV+/cART+ children relative to the HIV- cohort.

Unique to the HIV+/cART+ cohort was a reduced thickness of the left medial pallidum. These associations occurred in the absence of significant differences between HIV+/cART+ and HIV+/cART- children in either shape or volumetric characteristics. The presence of such interactions does, however, suggest independent contributions of cART exposure to subcortical morphometry. The unique changes in HIV+/cART- morphometry were expansions of thickness and surface area which would be consistent with processes of chronic inflammatory responses. However, it is difficult to account for the increased surface area of the right medial amygdala exhibited by HIV+/cART+ participants if moderated inflammation is the underlying process. It is similarly difficult to account for the reduced thickness of the bilateral pallidum in HIV+/cART+ participants relative to controls that is absent in HIV+/cART- children.

The basal ganglia has been shown to be preferentially affected by several disorders including Alzheimer's disease, multiple sclerosis and diabetes (de Jong *et al*, 2008; Kramer *et al*, 2015; van Duinkerken *et al*, 2014) as well as HIV (Aylward *et al*, 1993; Berger and Arendt, 2000; Berger and Nath, 1997; Wright *et al*, 2016). Exact mechanisms for this preferential insult remain poorly characterized though there is evidence that viral replication occurs more readily in perivascular and parenchymal macrophages within the basal ganglia (Pumarola-Sune *et al*, 1987). Similarly, hypermetabolism of the basal ganglia is described in CNS HIV infection (Rottenberg *et al*, 1987) which likely reflects inflammation and may indicate ongoing viral replication. As suggested by Wright, a common mechanism of preferential basal ganglia injury between HIV, Alzheimer's, Diabetes and multiple sclerosis may be tied to vascular damage as well as chronic inflammation (Wright *et al*, 2016).

However, in our study the observed reductions in pallidal volumes were present in HIV+/cART+ relative to HIV- children which may be suggestive of neurotoxicity of prolonged

cART exposure. Existing literature on cART neurotoxicity is mixed. Ciccarelli has, for instance, reported poorer cognitive performances on the stroop and double barrage tasks in elderly patients receiving efavirenz (Ciccarelli *et al*, 2011). Nucleoside reverse transcriptase inhibitors used to suppress HIV replication have additionally been demonstrated to have mitochondrial toxicity which may result in reduced brain mitochondria and CNS cell respiration (Schweinsburg *et al*, 2005). However, in a recent study Brier administered efavirenz and ritonavir (two common antiretroviral medications) to HIV- participants and reported that neither drug was associated with changes in functional connectivity or cerebral blood flow, suggesting that cART has few neurotoxic effects (Brier *et al*, 2015). Our baseline findings are also somewhat contrary to those reported in (Ances *et al*, 2012) who compared the volumes of brain structures of 78 HIV- participants, 26 HIV+/HAART+ (highly active antiretroviral therapy) and 26 HIV+/HAART- participants and identified no independent neurodegeneration associated with HAART reception; but this difference may be due to the large age differences between the two cohorts. Though we similarly did not observe volumetric associations with cART status among HIV+ children or associations between HIV and cART status, high-dimensional shape-based abnormalities were observed in our study.

HIV is also widely reported to adversely affect the integrity of white matter microstructure. Wu reported significantly increased mean diffusivity in HIV-infected participants in the splenium of the callosum (Wu *et al*, 2006). These abnormalities were further associated with HIV-related dementia and deficits in motor speed. Echoing this finding, Hoare found decreased fractional anisotropy in the callosum, superior longitudinal fasciculus and cingulum, in an adult HIV+ cohort (Hoare *et al*, 2011). Investigating an adult cohort, Ragin reported reduced fractional anisotropy in the callosum of HIV+ participants, and increased diffusivity in the

caudate (Ragin *et al*, 2015). Our results are partially aligned with these findings as we have reported a non-significant reduction of the total callosum volume of 13% in the HIV+ cohort. While this effect was only significant prior to FDR correction, its magnitude is at least suggestive of an effect.

Several somewhat unexpected associations between baseline (current) CD4 count and brain morphometry were observed as well and, in several cases, interacted with cART reception. Specifically, we observed significant differential associations between the volume, thickness and surface area of the left pallidum as a function of CD4 count and HIV by cART status. Here, the volume and surface area of the left pallidum were significantly reduced at higher CD4 counts among HIV+ participants while being elevated in HIV- children. The thickness of this region exhibited an additionally significant association with cART status in which HIV+/cART+ participants alone had significantly reduced thickness of the pallidum at higher CD4 counts relative to HIV- participants. HIV+/cART- participants showed a similar interaction in the surface area of the right superior caudate which was significantly reduced at elevated CD4 counts whereas the association was positive among HIV- participants. This is a somewhat unexpected observation as we naively expected to observe positive associations between shape and volume of brain regions and CD4 counts regardless of HIV or cART status. However, this finding is not without precedent. A report from the CNS HIV Antiretroviral Therapy Effects Research (CHARTER) study observed reduced white and grey matter volumes and higher ventricular spaces among HIV+ participants who had higher current CD4 counts (Jernigan *et al*, 2011). These associations were present only when nadir CD4 was accounted for and not present independently of nadir CD4. The authors concluded that it is, therefore, the magnitude of the difference between current and nadir CD4 that is most indicative of infection severity. The

associations of brain morphometry reported in our study are based on current CD4 count which is also the nadir CD4 for those receiving cART given that CD4 levels were by design at their lowest prior to cART initiation. These somewhat unexpected directions of associations may potentially reflect a moderation of inflammatory responses in the presence of additional CD4 cells whereas participants with lower CD4 counts may have ongoing, chronic inflammatory responses in the reported regions.

Longitudinal models of HIV-related abnormalities, revealed an increased rate of gain in the thickness of the right lateral pallidum among HIV+ participants relative to controls. Similarly, the rate of gain of surface area in the left anterior accumbens was higher among the HIV+ cohort. It seems highly unlikely that the observed rates of gains in thickness and surface area are reflective of healthy developmental processes. For reasons discussed previously, HIV infection has a predilection for the basal ganglia, an environment with highly favorable conditions for viral replication. While we can not definitively conclude that the accelerated trajectories of the pallidum and accumbens are reflective of underlying chronic inflammation through either MRS markers or cytokine measures, this is the most likely explanation. Importantly these associations survive when cART status is included as a covariate in the regression model and we observed no longitudinal interaction of HIV and cART status. Although, among HIV+ participants, the timing of cART status was observed to be associated with the trajectory of the right posterior putamen surface area; specifically with those being initiated to cART at baseline having diminished surface area of this region over time relative to those initiated between baseline and follow-up. This association very likely reflects the differential illness severity between these groups as those who were initiated had more severely low CD4 counts. Upon initiation to cART CD4 counts were significantly lower than those who

were enrolled between time points. This effect survived when we covaried for current CD4 counts. Again, given the proclivity of HIV for regions of the basal ganglia including the putamen, it seems reasonable to expect that this is reflective of reduced chronic inflammation among those enrolled to cART at baseline. However, we reiterate that only 9 participants were enrolled to cART between time points which is a very small sample to estimate. Observations in small samples should be replicated in larger cohorts before conclusions are made.

Prior studies have associated viral RNA load with severity of cognitive impairment in children (Koekkoek *et al*, 2008; Nichols *et al*, 2000; Wolters *et al*, 1994; Wood *et al*, 2009). We report longitudinal associations between initial (baseline) viral RNA detectability and the surface area of the right accumbens in which some regions contract and others expand more rapidly over time in children with detectable viral RNA. This effect is somewhat unclear but, taken together with the longitudinal deformations associated directly with HIV status reported previously, may reflect deformations of the accumbens cellular structure. Roscoe reported that the branching complexity of medium spiny neurons of HIV-1 transgenic rats are greatly reduced relative to controls with additional shorter length and volume of dendritic spines of these cells (Roscoe *et al*, 2014). Abnormalities of the accumbens are classically associated with apathy and depression (Levy and Dubois, 2006; Nestler and Carlezon, 2006) which are common comorbid sequelae of HIV infection (Paul *et al*, 2005). These particular findings may have implications for biomarkers of apathy and depression among HIV+ youths. We encourage future investigations to explore this potential association.

We additionally observed a longitudinal association between viral RNA detectability and the volume of the right lateral ventricular space: detectable viral RNA was associated with an increased rate of ventricular space loss between the two time points. Though we would naively

expect detectable viral RNA levels to be associated with poorer health resulting in neuronal atrophy and therefore expanded ventricular spaces, this observation is again consistent with chronic inflammation of surrounding brain tissue which would result in impingements on ventricular spaces as observed here.

Previous studies of structural brain imaging in pediatric cohorts are sparse. As noted by Laughton, there is severe paucity of studies on adolescent HIV from resource-constrained countries in which perinatal infection is most prevalent (Laughton *et al*, 2013). Our study begins to address this void. Several previous studies of brain imaging in pediatric HIV do exist, however. Recently Cohen reported on a cohort of 35 HIV+ children on cART and 37 matched controls between the ages of 8 and 18 years (Cohen *et al*, 2016). They reported a higher rate of white matter hyperintensities, and lower gray and white matter volumes among the HIV+ children. Sarma reported on a comparatively smaller cohort of 16 HIV+ youths on ART and 14 uninfected controls between the ages of 13-25 years (Sarma *et al*, 2014). Using T1-weighted MRI, they reported white matter atrophy of the posterior corpus callosum (CC), bilateral external capsule, bilateral ventral temporal WM, mid cerebral peduncles, and basal pons as well as gray matter volume increases in the left superior frontal gyrus, inferior occipital gyrus, gyrus rectus, right mid cingulum, parahippocampal gyrus, bilateral inferior temporal gyrus, and middle temporal gyrus in the HIV+ cohort versus controls. Previous studies on the efficacy of antiretroviral treatments in adolescence in developing countries have failed to identify significant improvements as a result of treatment. For instance, the parent study of this report identified no significant improvement in cognitive functions in Thai children initiated to ART (Puthanakit *et al*, 2010) and later reported no observable differences between children initiated to ART at an early or deferred period (Puthanakit *et al*, 2013). An additional study in a South African cohort

also reported no cognitive improvements following 6 months of ART (Eley *et al*, 2008). Our findings extend our understanding of brain development in perinatally-infected children. As a result of using highly sensitive shape-based measures we were able to identify both cross-sectional and longitudinal variations in subcortical morphometry related to HIV and cART status that would have been overlooked in a purely volumetric paradigm.

Several notable limitations are important to factor into any interpretation of the reported findings. The first is that the timeframe of one year we report on is arguably narrow for a longitudinal study. The baseline ages of our patients was roughly 11 years, on average, and ranged from 6 to 16 across diagnostic groups. We know from previous studies of adolescent brain development (Giedd, 2004) that this is a time characterized by complex patterns of age and sex-dependent rates of gray matter pruning and myelination. Given this a wider time frame would be beneficial. However, despite this limitation we managed to identify several longitudinal abnormalities among the HIV+ cohort as well as numerous associations at baseline. We additionally note that the time to follow-up was significantly larger in the HIV+ cohort. As such we have included this as a covariate in our longitudinal models and all reported associations survived despite this variability. As discussed previously, the original sample included three time points, however, the HIV+ cohort was a full year older at baseline relative to the control group. To account for this we disregarded the true baseline of the control cohort and final (third) time point of the HIV+ group to force the groups to be age matched. As a result we sacrificed the ability to compare the two groups across a wider timeframe. Additional limitations that should be considered when interpreting these results are the lack of controlling for the effects of either educational level or social economic status of the children or caregivers in our regression models. The interactions between familial and social factors with respect to brain development

are, of course, complex. However, as noted in (Puthanakit *et al*, 2013), the primary caregivers' education and income levels for the HIV+ and HIV- cohorts were comparable and, despite this, neurodevelopmental outcomes were better among the uninfected cohort which suggests a dominant effect of infection. Moreover, the effect of inflammatory responses is difficult to definitively rule in or out of the underlying processes we report here without direct measures of either MRS metabolites such as myo-inositol, total creatine and choline containing compounds, or other biological markers such as pro-inflammatory cytokines. Although numerous studies have identified cortical neurodegeneration in HIV+ cohorts, our focus in the current study was solely on the morphometry of subcortical structures. Of course, an investigation of cortical development in HIV+ children is of great interest as well, however it is beyond the scope of the current study and we encourage future investigations to pursue this fascinating line of research. Lastly, while our sample size was not prohibitively small to detect changes, several larger cohorts such as the Multicenter AIDS Study Cohort (MACS) and The CNS HIV Anti-Retroviral Therapy Effects Research (CHARTER) do exist, though they are not pediatric studies from a developing country.

In conclusion, we observed a number of abnormalities in both baseline and longitudinal morphometry of subcortical structures in HIV+ children. The majority of significant morphological abnormalities were revealed by shape-based descriptors of anatomy rather than standard volumetric characterizations, so many of the differences may be rather subtle overall. While we did not observe main effects of cART treatment on brain structure, interactions of cART status with HIV status were suggestive of the efficacy of cART. Nevertheless, we advise caution in the interpretation of this finding since children were selected for the parent study due to ability to survive without cART at the time of randomization. Thus, survivor tendencies may

mitigate our ability to detect direct associations with cART and its benefits. However viral RNA detectability and CD4 cell count had statistically influences on subcortical structures, primarily in the basal ganglia and, to a lesser extent, the dorsal and ventral striatum that are regions often implicated as being affected by HIV infection in other cohorts.

Acknowledgements

Chapter 4 is a version of Wade BS, Valcour VG, Prasitsuebsai W, Saremi A, Gutman BA, Jahanshad N, Nir TM, Ananworanich J, Watson C, Puthanakit T, Aurpibul L, Kosalaraksa P, Thompson PM. (2017). Mapping Longitudinal Subcortical Morphometry in Children with HIV. *Human Brain Mapping*. In Review.

Victor Valcour, Wasana Prasitsuebsai, Linda Aurpibul, Jintanat Ananworanich, Thanyawee Puthanakit and Pope Kosalaraksa coordinated the parent study which contributed data to this study. Arvin Saremi, Neda Jahanshad and Talia Nir assisted in data analysis and interpretation. Boris Gutman developed the shape analysis method applied here. Christa Watson aided in data management. Paul Thompson was the study PI.

This work was supported by R01MH089722 (VV) and R01MH102151 (JA) and also and also in part by NIH 'Big Data to Knowledge' (BD2K) Center of Excellence grant U54 EB020403, funded by a cross-NIH consortium including NIBIB and NCI and by the National Science Foundation Graduate Research Fellowship under Grant No. DGE-0707424 (BW). The main randomized study was supported by a grant from the National Institute of Allergy and Infectious Diseases of the US National Institutes of Health through the Comprehensive International Program of Research on AIDS Network (U19 AI53741), and was co-funded by the Eunice Shriver Kennedy National Institute of Child Health and Human Development and the National Institute of Mental Health, the National Research Council of Thailand, and National

Health Security Office, Thailand. Antiretroviral drugs were provided by ViiV Healthcare, GlaxoSmithKline, Boehringer Ingelheim, Merck, Abbott, and Roche. The views expressed are those of the authors and should not be construed to represent the positions of the U.S. Army, the Department of Defense, the National Science Foundation, the National Institutes of Health or US Department of Health and Human Services.

References

Ances BM, Ortega M, Vaida F, Heaps J, Paul R (2012). Independent effects of HIV, aging, and HAART on brain volumetric measures. *Journal of Acquired Immune Deficiency Syndromes* **59**(1944-7884 (Electronic)): 469-477.

Anderson E, Zink W, Xiong H, Gendelman HE (2002). HIV-1-associated dementia: a metabolic encephalopathy perpetrated by virus-infected and immune-competent mononuclear phagocytes. *Journal of acquired immune deficiency syndromes (1999)* **31 Suppl 2**: S43-54.

Aylward EH, Henderer JD, McArthur JC, Brettschneider PD, Harris GJ, Barta PE*, et al* (1993). Reduced basal ganglia volume in HIV-1-associated dementia: results from quantitative neuroimaging. *Neurology* **43**(10): 2099-2104.

Becker JT, Maruca V, Kingsley LA, J.M. S, Alger JR, Barker PB*, et al* (2012). Factors affecting brain structure in men with HIV disease in the post-HAART era. *Neuroradiology* **54**(1432-1920 (Electronic)): 113-121.

Benjamini Y, Hochberg Y (1995). Controlling the false discovery rate: a practical and powerful approach to multiple testing. *Journal of the Royal Statistical Society Series B (Methodological)*: 289-300.

Berger JR, Arendt G (2000). HIV dementia: the role of the basal ganglia and dopaminergic systems. *Journal of psychopharmacology* **14**(3): 214-221.

Berger JR, Nath A (1997). HIV dementia and the basal ganglia. *Intervirology* **40**(2-3): 122-131.

Brew BJ (2004). Evidence for a change in AIDS dementia complex in the era of highly active antiretroviral therapy and the possibility of new forms of AIDS dementia complex. *AIDS* **18**: 75-78.

Brier MR, Wu Q, Tanenbaum AB, Westerhaus ET, Kharasch ED, Ances BM (2015). Effect of HAART on Brain Organization and Function in HIV-Negative Subjects. *Journal of neuroimmune pharmacology : the official journal of the Society on NeuroImmune Pharmacology* **10**(4): 517-521.

Canizares S, Cherner M, Ellis RJ (2014). HIV and aging: effects on the central nervous system. *Seminars in Neurology* **34**(1098-9021 (Electronic)): 27-34.

Chiriboga CA, Fleishman S, Champion S, Gaye-Robinson L, Abrams EJ (2005). Incidence and prevalence of HIV encephalopathy in children with HIV infection receiving highly active anti-retroviral therapy (HAART). *The Journal of pediatrics* **146**(3): 402-407.

Ciccarelli N, Fabbiani M, Di Giambenedetto S, Fanti I, Baldonero E, Bracciale L*, et al* (2011). Efavirenz associated with cognitive disorders in otherwise asymptomatic HIV-infected patients. *Neurology* **76**(16): 1403-1409.

Cohen S, Caan MW, Mutsaerts HJ, Scherpbier HJ, Kuijpers TW, Reiss P*, et al* (2016). Cerebral injury in perinatally HIV-infected children compared to matched healthy controls. *Neurology* **86**(1): 19-27.

Cooper ER, Hanson C, Diaz C, Mendez H, Abboud R, Nugent R*, et al* (1998). Encephalopathy and progression of human immunodeficiency virus disease in a cohort of children with perinatally acquired human immunodeficiency virus infection. Women and Infants Transmission Study Group. *The Journal of pediatrics* **132**(5): 808-812.

de Jong LW, van der Hiele K, Veer IM, Houwing JJ, Westendorp RGJ, Bollen E*, et al* (2008). Strongly reduced volumes of putamen and thalamus in Alzheimer's disease: an MRI study. *Brain* **131**(12): 3277-3285.

Eley BS, Smith L, Adnams C (2008). *Neurological and neurocognitive function of HIV-infected children commenced on antiretroviral therapy*. Vol 2.

Ellis R, Langford D, Masliah E (2007). HIV and antiretroviral therapy in the brain: neuronal injury and repair. *Nat Rev Neurosci* **8**(1): 33-44.

Epstein LG, Gelbard HA (1999). HIV-1-induced neuronal injury in the developing brain. *Journal of leukocyte biology* **65**(4): 453-457.

Epstein LG, Sharer LR, Oleske JM, Connor EM, Goudsmit J, Bagdon L*, et al* (1986). Neurologic manifestations of human immunodeficiency virus infection in children. *Pediatrics* **78**(4): 678-687.

Fennema-Notestine C, Ellis RJ, Archibald SL, Jernigan TL, Letendre SL, Notestine RJ*, et al* (2013). Increases in brain white matter abnormalities and subcortical gray matter are linked to CD4 recovery in HIV infection. *J Neurovirol* **19**(4): 393-401.

Fischl B, Salat DH, Busa E, Albert M, Dieterich M, Haselgrove C*, et al* (2002). Whole brain segmentation: automated labeling of neuroanatomical structures in the human brain. *Neuron* **33**(3): 341-355.

Gartner S (2000). HIV infection and dementia. *Science (New York, NY)* **287**(0036-8075 (Print)): 602-604.

Gendelman HE, Baldwin T, Baca-Regen L, Swindells S, Loomis L, Skurkovich S (1994). Regulation of HIV1 replication by interferon alpha: from laboratory bench to bedside. *Research in immunology* **145**(8-9): 679-684; discussion 684-675.

George R, Andronikou S, du Plessis J, du Plessis AM, Van Toorn R, Maydell A (2009). Central nervous system manifestations of HIV infection in children. *Pediatric radiology* **39**(6): 575-585.

Giedd JN (2004). Structural magnetic resonance imaging of the adolescent brain. *Annals of the New York Academy of Sciences* **1021**: 77-85.

Gutman B, Jahanshad N, Ching C, Wang Y, Kochunov P, Nichols T*, et al* (2015a). Medial Demons Registration Localizes the Degree of Genetic Influence over Subcortical Shape Variability: An N= 1480 Meta-Analysis. *International Symposium on Biomedical Imaging*.

Gutman B, Madsen S, Toga A, Thompson P (2013). A Family of Fast Spherical Registration Algorithms for Cortical Shapes. *Multimodal Brain Image Analysis* **8159**: 246-257.

Gutman B, Wang Y, Rajagopalan P, Toga A, Thompson P (2012). Shape matching with medial curves and 1-D group-wise registration. *International Symposium on Biomedical Imaging* **9**: 716-719.

Gutman BA, Jahanshad N, Ching CR, Wang Y, Kochunov PV, Nichols TE*, et al* (2015b). Medial Demons Registration Localizes The Degree of Genetic Influence Over Subcortical Shape Variability: An N= 1480 Meta-Analysis. *Proceedings / IEEE International Symposium on Biomedical Imaging: from nano to macro IEEE International Symposium on Biomedical Imaging* **2015**: 1402-1406.

Gutman BA, Wang Y, Yanovsky I, Hua X, Toga AW, Jack CR, Jr.*, et al* (2015c). Empowering imaging biomarkers of Alzheimer's disease. *Neurobiology of aging* **36 Suppl 1**: S69-80.

Heaton R, Grant I, Butters N, White D, Kirson D, Atkinson J (1995). The HNRC 500-Neuropsychology of HIV infection at different disease stages. *J International Neuropsychological Society* **1**(03): 231-251.

Hoare J, Fouche JP, Phillips N, Joska JA, Donald KA, Thomas K*, et al* (2015). Clinical associations of white matter damage in cART-treated HIV-positive children in South Africa. *J Neurovirol* **21**(2): 120-128.

Hoare J, Fouche JP, Spottiswoode B, Sorsdahl K, Combrinck M, Stein DJ*, et al* (2011). White-Matter damage in Clade C HIV-positive subjects: a diffusion tensor imaging study. *The Journal of neuropsychiatry and clinical neurosciences* **23**(3): 308-315.

Hong S, Banks WA (2015). Role of the immune system in HIV-associated neuroinflammation and neurocognitive implications. *Brain, behavior, and immunity* **45**: 1-12.

Hua X, Boyle CP, Harezlak J, Tate DF, Yiannoutsos CT, Cohen R*, et al* (2013). Disrupted cerebral metabolite levels and lower nadir CD4 + counts are linked to brain volume deficits in 210 HIV-infected patients on stable treatment. *NeuroImage Clinical* **3**: 132-142.

Jahanshad N, Couture MC, Prasitsuebsai W, Nir TM, Aurpibul L, Thompson PM*, et al* (2015). Brain Imaging and Neurodevelopment in HIV-uninfected Thai Children Born to HIV-infected Mothers. *Pediatr Infect Dis J* **34**(9): e211-216.

Jernigan TL, Archibald SL, Fennema-Notestine C, Taylor MJ, Theilmann RJ, Julaton MD*, et al* (2011). Clinical factors related to brain structure in HIV: the CHARTER study. *J Neurovirol* **17**(3): 248-257.

Kallianpur KJ, Shikuma C, Kirk GR, Shiramizu B, Valcour V, Chow D*, et al* (2013). Peripheral blood HIV DNA is associated with atrophy of cerebellar and subcortical gray matter. *Neurology* **80**(19): 1792-1799.

Kim WK, Corey S, Alvarez X, Williams K (2003). Monocyte/macrophage traffic in HIV and SIV encephalitis. *Journal of leukocyte biology* **74**(5): 650-656.

Koekkoek S, de Sonneville LM, Wolfs TF, Licht R, Geelen SP (2008). Neurocognitive function profile in HIV-infected school-age children. *European journal of paediatric neurology : EJPN : official journal of the European Paediatric Neurology Society* **12**(4): 290-297.

Koenig S, Gendelman HE, Orenstein JM, Dal Canto MC, Pezeshkpour GH, Yungbluth M*, et al* (1986). Detection of AIDS virus in macrophages in brain tissue from AIDS patients with encephalopathy. *Science (New York, NY)* **233**(4768): 1089-1093.

Kramer J, Meuth SG, Tenberge JG, Schiffler P, Wiendl H, Deppe M (2015). Early and Degressive Putamen Atrophy in Multiple Sclerosis. *International journal of molecular sciences* **16**(10): 23195-23209.

Kure K, Lyman WD, Weidenheim KM, Dickson DW (1990). Cellular localization of an HIV-1 antigen in subacute AIDS encephalitis using an improved double-labeling immunohistochemical method. *The American journal of pathology* **136**(5): 1085-1092.

Langford D, Masliah E (2001). Crosstalk between components of the blood brain barrier and cells of the CNS in microglial activation in AIDS. *Brain pathology (Zurich, Switzerland)* **11**(3): 306-312.

Laughton B, Cornell M, Boivin M, Van Rie A (2013). Neurodevelopment in perinatally HIV-infected children: a concern for adolescence. *Journal of the International AIDS Society* **16**: 18603.

Levy R, Dubois B (2006). Apathy and the functional anatomy of the prefrontal cortex-basal ganglia circuits. *Cerebral cortex (New York, NY : 1991)* **16**(7): 916-928.

Li Y, Li H, Gao Q, Yuan D, Zhao J (2014). Structural gray matter change early in male patients with HIV. *International journal of clinical and experimental medicine* **7**(10): 3362-3369.

Lu SM, Tremblay ME, King IL, Qi J, Reynolds HM, Marker DF*, et al* (2011). HIV-1 Tat-induced microgliosis and synaptic damage via interactions between peripheral and central myeloid cells. *PLoS One* **6**(9): e23915.

Martin SC, Wolters PL, Toledo-Tamula MA, Zeichner SL, Hazra R, Civitello L (2006). Cognitive functioning in school-aged children with vertically acquired HIV infection being treated with highly active antiretroviral therapy (HAART). *Developmental neuropsychology* **30**(2): 633-657.

Masliah E, Ge N, Mucke L (1996). Pathogenesis of HIV-1 associated neurodegeneration. *Critical reviews in neurobiology* **10**(1): 57-67.

Nachman S, Chernoff M, Williams P, Hodge J, Heston J, Gadow KD (2012). Human immunodeficiency virus disease severity, psychiatric symptoms, and functional outcomes in perinatally infected youth. *Archives of pediatrics & adolescent medicine* **166**(6): 528-535.

Nestler EJ, Carlezon WA, Jr. (2006). The mesolimbic dopamine reward circuit in depression. *Biological psychiatry* **59**(12): 1151-1159.

Nichols S, Mahoney EM, Sirois PA, Bordeaux JD, Stehbens JA, Loveland KA*, et al* (2000). HIV-associated changes in adaptive, emotional, and behavioral functioning in children and adolescents with hemophilia: results from the Hemophilia Growth and Development Study. *Journal of pediatric psychology* **25**(8): 545-556.

Patel K, Ming X, Williams PL, Robertson KR, Oleske JM, Seage GR, 3rd (2009). Impact of HAART and CNS-penetrating antiretroviral regimens on HIV encephalopathy among perinatally infected children and adolescents. *Aids* **23**(14): 1893-1901.

Paul RH, Brickman AM, Navia B, Hinkin C, Malloy PF, Jefferson AL*, et al* (2005). Apathy is Associated With Volume of the Nucleus Accumbens in Patients Infected With HIV. *The Journal of neuropsychiatry and clinical neurosciences* **17**(2): 167-171.

Puccini JM, Marker DF, Fitzgerald T, Barbieri J, Kim CS, Miller-Rhodes P*, et al* (2015). Leucine-rich repeat kinase 2 modulates neuroinflammation and neurotoxicity in models of human immunodeficiency virus 1-associated neurocognitive disorders. *The Journal of neuroscience : the official journal of the Society for Neuroscience* **35**(13): 5271-5283.

Pumarola-Sune T, Navia BA, Cordon-Cardo C, Cho ES, Price RW (1987). HIV antigen in the brains of patients with the AIDS dementia complex. *Annals of neurology* **21**(5): 490-496.

Puthanakit T, Ananworanich J, Vonthanak S, Kosalaraksa P, Hansudewechakul R, van der Lugt J*, et al* (2013). Cognitive function and neurodevelopmental outcomes in HIV-infected Children older than 1 year of age randomized to early versus deferred antiretroviral therapy: the PREDICT neurodevelopmental study. *Pediatr Infect Dis J* **32**(5): 501-508.

Puthanakit T, Aurpibul L, Louthrenoo O, Tapanya P, Nadsasarn R, Insee-ard S*, et al* (2010). Poor cognitive functioning of school-aged children in thailand with perinatally acquired HIV infection taking antiretroviral therapy. *AIDS patient care and STDs* **24**(3): 141-146.

Puthanakit T, Saphonn V, Ananworanich J, Kosalaraksa P, Hansudewechakul R, Vibol U*, et al* (2012). Early versus deferred antiretroviral therapy for children older than 1 year infected with HIV (PREDICT): a multicentre, randomised, open-label trial. *The Lancet Infectious diseases* **12**(12): 933-941.

Ragin AB, Wu Y, Gao Y, Keating S, Du H, Sammet C*, et al* (2015). Brain alterations within the first 100 days of HIV infection. *Annals of clinical and translational neurology* **2**(1): 12-21.

Raskino C, Pearson DA, Baker CJ, Lifschitz MH, O'Donnell K, Mintz M*, et al* (1999). Neurologic, neurocognitive, and brain growth outcomes in human immunodeficiency virus-infected children receiving different nucleoside antiretroviral regimens. Pediatric AIDS Clinical Trials Group 152 Study Team. *Pediatrics* **104**(3): e32.

Roscoe RF, Mactutus CF, Booze RM (2014). HIV-1 Transgenic Female Rat: Synaptodendritic Alterations of Medium Spiny Neurons in the Nucleus Accumbens. *Journal of neuroimmune pharmacology : the official journal of the Society on NeuroImmune Pharmacology* **9**(5): 642-653.

Rottenberg DA, Moeller JR, Strother SC, Sidtis JJ, Navia BA, Dhawan V*, et al* (1987). The metabolic pathology of the AIDS dementia complex. *Annals of neurology* **22**(6): 700-706.

Sacktor N, McDermott MP, Marder K, Schifitto G, Selnes OA, McArthur JC*, et al* (2002). HIV-associated cognitive impairment before and after the advent of combination therapy. *J Neurovirol* **8**(2): 136-142.

Safriel YI, Haller JO, Lefton DR, Obedian R (2000). Imaging of the brain in the HIV-positive child. *Pediatric radiology* **30**(11): 725-732.

Sarma MK, Nagarajan R, Keller MA, Kumar R, Nielsen-Saines K, Michalik DE*, et al* (2014). Regional brain gray and white matter changes in perinatally HIV-infected adolescents(). *NeuroImage : Clinical* **4**: 29-34.

Schweinsburg BC, Taylor MJ, Alhassoon OM, Gonzalez R, Brown GG, Ellis RJ*, et al* (2005). Brain mitochondrial injury in human immunodeficiency virus-seropositive (HIV+) individuals taking nucleoside reverse transcriptase inhibitors. *J Neurovirol* **11**(4): 356-364.

Shanbhag MC, Rutstein RM, Zaoutis T, Zhao H, Chao D, Radcliffe J (2005). Neurocognitive functioning in pediatric human immunodeficiency virus infection: effects of combined therapy. *Archives of pediatrics & adolescent medicine* **159**(7): 651-656.

Smith R, Chernoff M, Williams PL, Malee KM, Sirois PA, Kammerer B*, et al* (2012). Impact of HIV severity on cognitive and adaptive functioning during childhood and adolescence. *Pediatr Infect Dis J* **31**(6): 592-598.

Tepper VJ, Farley JJ, Rothman MI, Houck DL, Davis KF, Collins-Jones TL*, et al* (1998). Neurodevelopmental/neuroradiologic recovery of a child infected with HIV after treatment with combination antiretroviral therapy using the HIV-specific protease inhibitor ritonavir. *Pediatrics* **101**(3): E7.

Uban KA, Herting MM, Williams PL, Ajmera T, Gautam P, Huo Y*, et al* (2015). White matter microstructure among youth with perinatally acquired HIV is associated with disease severity. *Aids* **29**(9): 1035-1044.

van Duinkerken E, Schoonheim MM, Steenwijk MD, Klein M, RG IJ, Moll AC*, et al* (2014). Ventral striatum, but not cortical volume loss, is related to cognitive dysfunction in type 1 diabetic patients with and without microangiopathy. *Diabetes Care* **37**(9): 2483-2490.

Van Rie A, Mupuala A, Dow A (2008). Impact of the HIV/AIDS epidemic on the neurodevelopment of preschool-aged children in Kinshasa, Democratic Republic of the Congo. *Pediatrics* **122**(1): e123-128.

Wade BS, Joshi SH, Njau S, Leaver AM, Vasavada M, Woods RP*, et al* (2016). Effect of Electroconvulsive Therapy on Striatal Morphometry in Major Depressive Disorder. *Neuropsychopharmacology : official publication of the American College of Neuropsychopharmacology*.

Wade BS, Valcour VG, Wendelken-Riegelhaupt L, Esmaeili-Firidouni P, Joshi SH, Gutman BA*, et al* (2015). Mapping abnormal subcortical brain morphometry in an elderly HIV + cohort. *NeuroImage Clinical* **9**: 564-573.

Wilson TW, Heinrichs-Graham E, Becker KM, Aloi J, Robertson KR, Sandkovsky U*, et al* (2015). Multimodal neuroimaging evidence of alterations in cortical structure and function in HIV-infected older adults. *Human brain mapping* **36**(3): 897-910.

Wolters PL, Brouwers P, Moss HA, Pizzo PA (1994). Adaptive behavior of children with symptomatic HIV infection before and after zidovudine therapy. *Journal of pediatric psychology* **19**(1): 47-61.

Wood SM, Shah SS, Steenhoff AP, Rutstein RM (2009). The impact of AIDS diagnoses on long-term neurocognitive and psychiatric outcomes of surviving adolescents with perinatally acquired HIV. *Aids* **23**(14): 1859-1865.

Wright PW, Pyakurel A, Vaida FF, Price RW, Lee E, Peterson J*, et al* (2016). Putamen volume and its clinical and neurological correlates in primary HIV infection. *Aids*.

Wu Y, Storey P, Cohen BA, Epstein LG, Edelman RR, Ragin AB (2006). Diffusion alterations in corpus callosum of patients with HIV. *AJNR American journal of neuroradiology* **27**(3): 656-660.

Zahr NM, Mayer D, Rohlfing T, Sullivan EV, Pfefferbaum A (2014). Imaging neuroinflammation? A perspective from MR spectroscopy. *Brain pathology (Zurich, Switzerland)* **24**(6): 654-664.

Tables

Table 4-1. Demographic and clinical characteristics

	HIV+	**HIV-**
Age, mean (sd), y	11.09 (2.36)	11.06 (2.79)
Sex, M/F	23/20	23/31
cART status, on/deferred	32/11	--
Age of cART initiation, mean (sd), y[a]	9.39 (3.23)	--
Log Viral RNA count, mean (sd), copies/ml	9.85 (11.16)	--
Detectable/undetectable vRNA, (%)[b]	25/75	--
CD4 count, mean (sd), cells/ml*	728 (323)	966 (307)
Days to follow-up*	472.69 (140.84)	365.11 (41.72)
Percent of age on cART, mean (sd)[c]	26.21 (13.99)	--
	HIV+/cART+	**HIV+/cART-**
Age, mean (sd), y	11.10 (2.26)	11.07 (2.72)
Sex, M/F	17/15	6/5
Log Viral RNA count, mean (sd), copies/ml	4.02 (1.23)	8.49 (3.77)
Detectable/undetectable vRNA, (%)*[b]	10/90	75/25
CD4 count, mean (sd), cells/ml*	853.53 (270.80)	362.54 (140.49)

[a]Based on the date that a participant received the first drug in the cART cocktail.

[b]Undetectable vRNA levels are < 50 copies per ml.

[c]Defined as percentage of age on cART at follow-up.

*significant difference

Figures

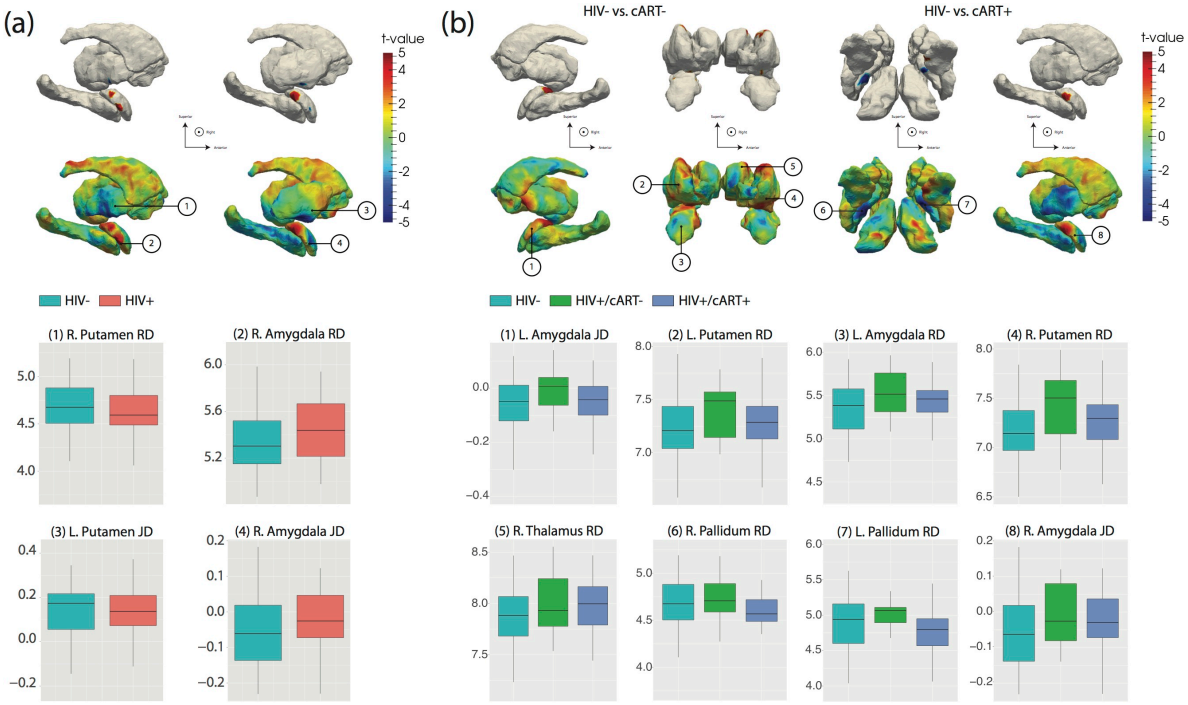

Figure 4-1. (a) T-value maps of the regression of shape on HIV status at baseline. (a, left) Radial distance (thickness) and (a, right) Jacobian determinant (surface area). The top row shows FDR-thresholded t-value maps while the bottom row shows unthresholded maps. Where a significant association was observed boxplots illustrate the average RD or JD value within the whole region. (a_1) Highlights a significantly reduced RD in the right medial pallidum in HIV+ subjects. (a_2) Shows increased RD of the right medial amygdala among HIV+ cohort. (a_3) Indicates reduced JD in the left lateral pallidum in HIV+ while (a_4) shows a regions of primarily increased JD in the right medial amygdala in HIV+. (b) T-value maps of the regression of shape on the interaction of HIV and cART status. (b_1) Significantly increased JD of the posterior medial left amygdala in HIV+/cART- subjects relative to HIV-; (b_2) Increased RD of the right superior putamen in HIV+/cART- subjects relative to HIV-; (b_3) Increased RD of left anterior amygdala in HIV+/cART- vs. HIV-; (b_4) Widely increased RD of right putamen in HIV+/cART- vs. HIV-; (b_5) Increased RD in right superior thalamus in HIV+/cART- vs. HIV-; ($b_6 - b_7$) Reduced bilateral medial pallidum RD in HIV+/cART+ vs. HIV-; Increased JD of right medial amygdala among HIV+/cART+ participants vs. HIV-.

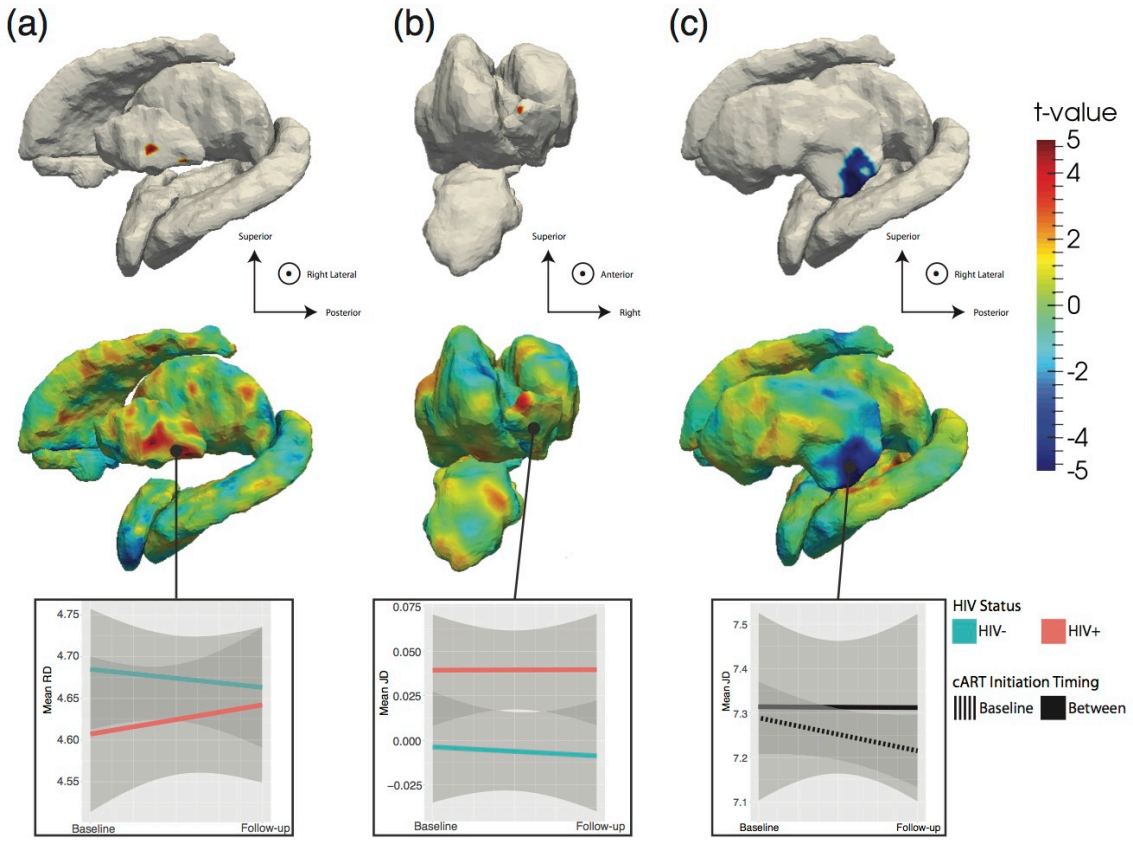

Figure 4-2. T-value maps of the longitudinal regression of (a) radial distance (thickness) and (b) Jacobian determinant (surface area) values on the interaction of HIV status and time. (c) Illustrates the interaction of cART initiation timing: enrollment at baseline vs. between baseline and follow-up. The top row illustrates FDR-thresholded maps with highlighted regions being those surviving multiple comparisons correction. The bottom row shows the uncorrected set of t-maps. For each region containing a significant association an interaction plot is given illustrating the differential trajectories of the shape descriptor over time stratified by HIV status. (a) Indicates that the trajectory of thickness increase is positive over time among HIV+ participants while being negative among HIV- participants. Similarly (b) indicates the rate of gain in the surface area of the anterior left accumbens is higher in the HIV+ cohort. (c) Shows that the surface area of the right lateral posterior putamen reduces over time among participants initiated to cART at baseline relative to those who were initiated between time points, the latter of whom remained relatively stable across time.

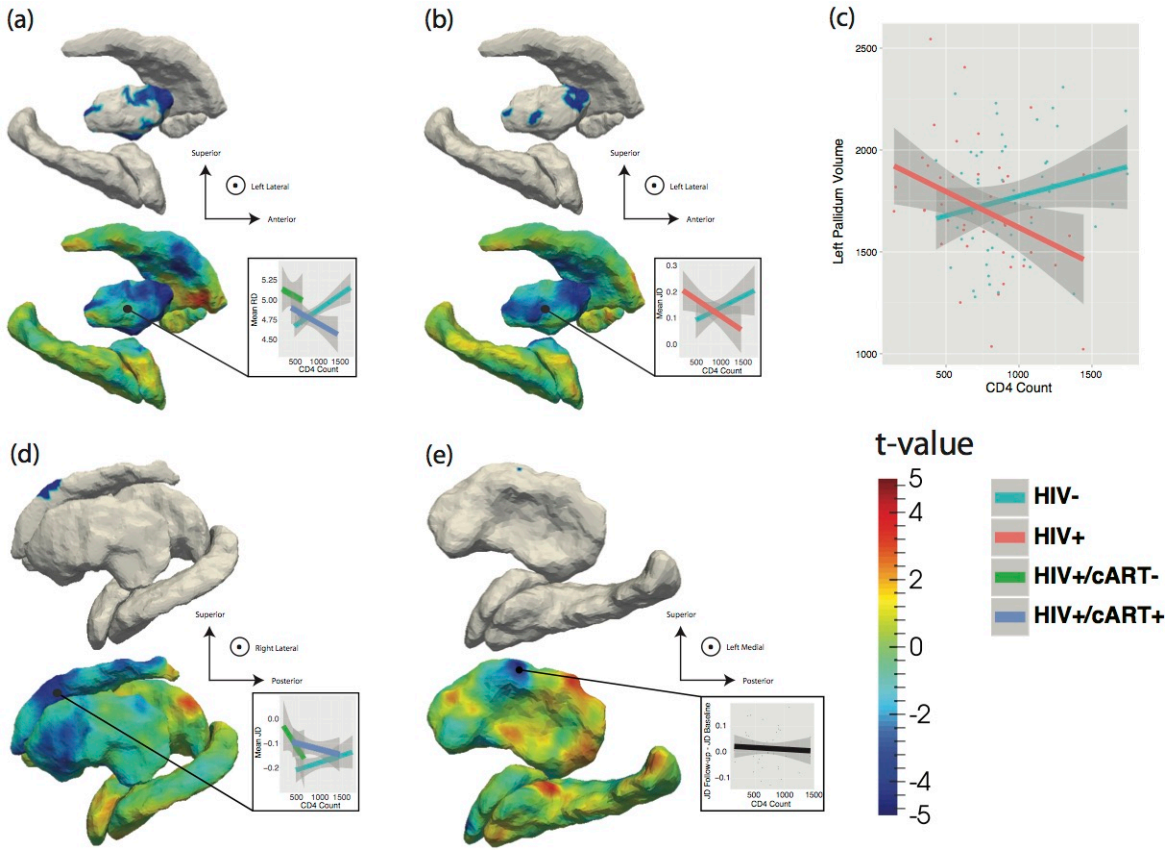

Figure 4-3. Baseline associations between CD4 count and HIV status and cART status where significant. (a) Significant inverse association of CD4 count and RD of left pallidum among HIV+/cART+ vs. HIV- cohort (HIV+/cART- vs. HIV- non-signficant, however, main effect of HIV status was significant). (b) Similarly, a significant inverse association of CD4 count and JD of left pallidum among HIV+ participants vs. HIV- with no significant interaction of cART status. (c) Significant inverse association of CD4 and volume of left pallidum among HIV+ group with positive association among HIV-; no significant interaction of cART status present. (d) Significantly reduced JD of superior right caudate at higher CD4 counts in HIV+/cART- vs. HIV- cohort. No significant main effects of HIV status or CD4 count were present, however. No significant differences between HIV+/cART+ and HIV- cohorts were present here either. (e) Highlights a region of the left superior putamen with a significant inverse association between CD4 count and surface area over time among HIV+ participants. No significant interaction of HIV or cART status was present for this longitudinal association.

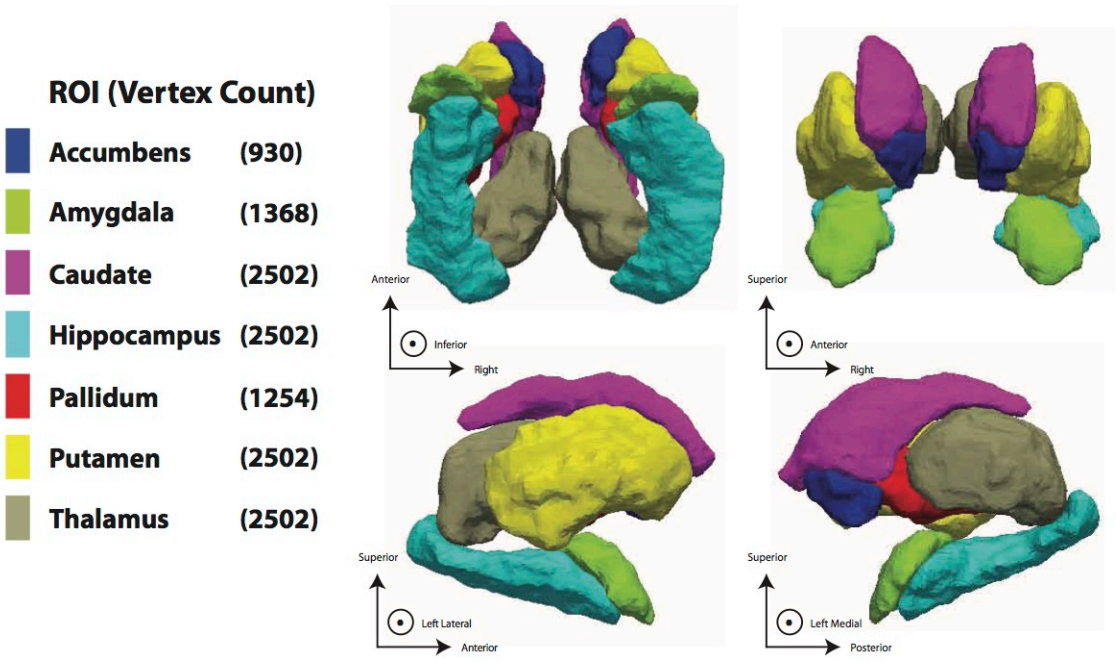

Figure 4-S1. Color-coded illustration of subcortical surfaces reported in this study along with the number of vertices comprising each surface. Note that all images are in radiological orientation throughout this manuscript, that is they are left-right flipped. Circled points within the axes labels indicate the orientation coming out of the page.

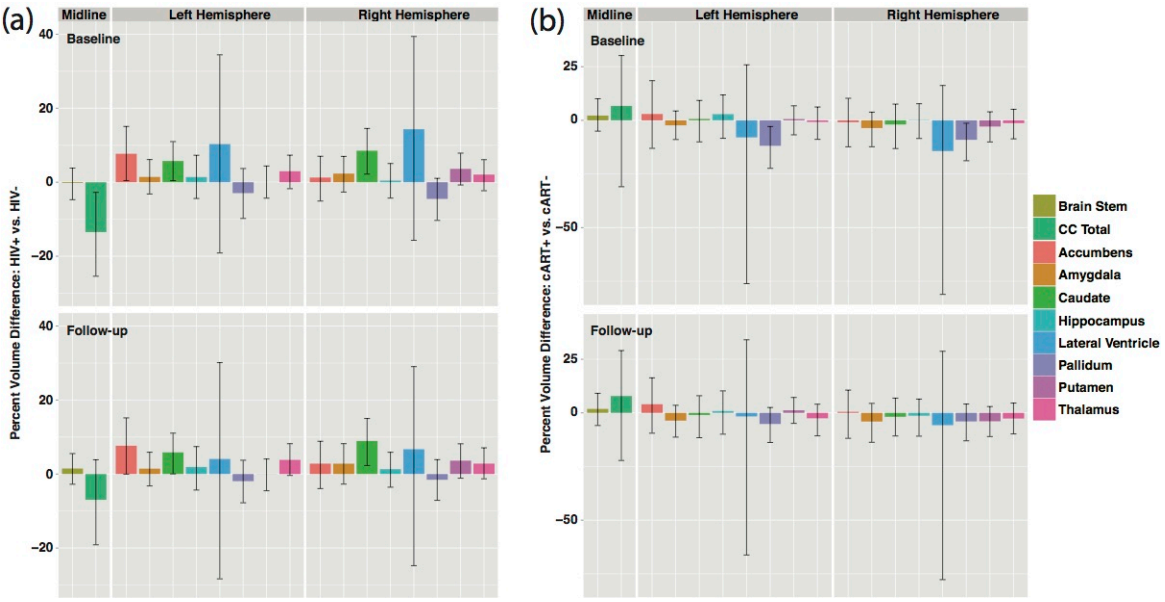

Figure 4-S2. (a) Percent of volumetric difference between HIV+ and HIV- groups at (top) baseline and (bottom) follow-up with bootstrapped 95% confidence intervals. Positive-valued

barplots indicate increased volume in the HIV+ cohort while negatively-valued barplots indicate reduced volume in the HIV+ corhort relative to controls. The majority of regions are numerically, though not significantly, increased in the HIV+ cohort. (b) Percent of volumetric difference between HIV+ participants receiving and not receiving cART at (top) baseline and (bottom) follow-up with bootstrapped 95% confidence intervals. Positive-valued barplots indicate increased volume in the cART+ cohort while negatively-valued barplots indicate reduced volume in the cART+ corhort. Differences are very small on average and not in consistent directions.

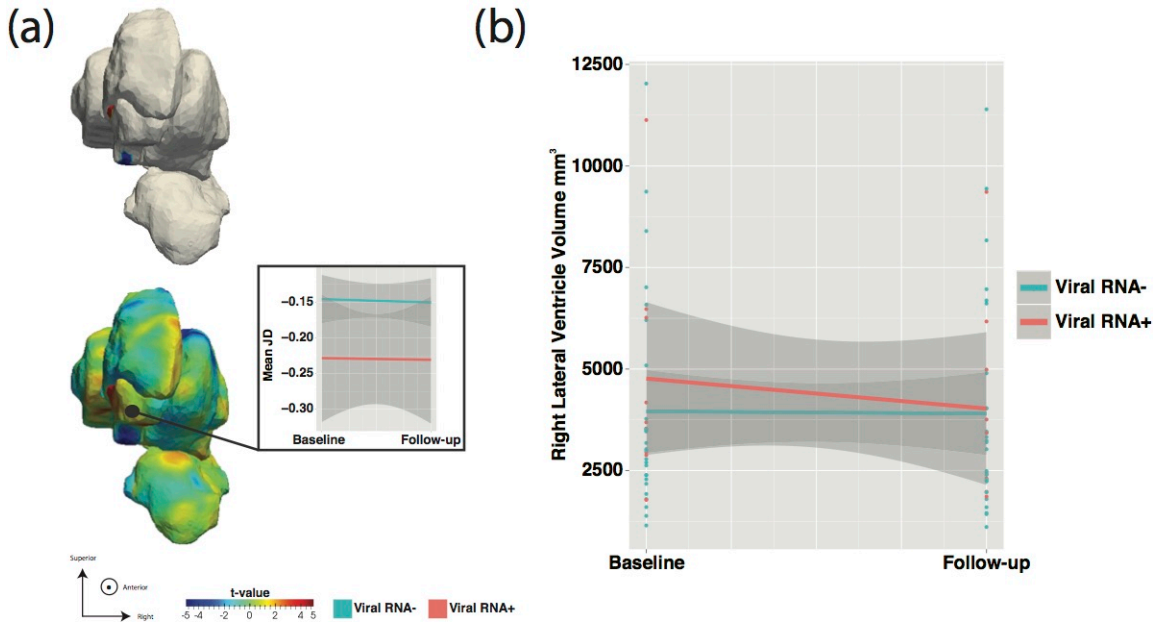

Figure 4-S3. (a) T-value maps of the differential longitudinal association of HIV+ participants with and without detectable levels of viral RNA with the JD (surface area) measure. The top plot is FDR thresholded indicating regions of both significantly expanded and reduced surface area in the right accumbens among participants with detectable viral RNA. Given the differential associations, the interaction plot of the average surface area within the right accumbens does not show a clear direction as the effects are in opposite directions across the surface. (b) Interaction plot of right lateral ventricle volume over time stratified by HIV+ participants with and without detectable viral RNA. The rate of loss of right lateral ventricle volume is more rapid among participants with detectable levels of viral RNA than those without.

Chapter 5: Effect of Electroconvulsive Therapy on Striatal Morphometry in Major Depressive Disorder[4]

Patients with major depression show reductions in striatal and paleostriatal volumes. The functional integrity and connectivity of these regions are also shown to change with antidepressant response. Electroconvulsive therapy (ECT) is a robust and rapidly acting treatment for severe depression. However, whether morphological changes in the dorsal and ventral striatum/pallidum relate to or predict therapeutic response to ECT is unknown. Using structural MRI, we assessed cross-sectional effects of diagnosis and longitudinal effects of ECT for volume and surface-based shape metrics of the caudate, putamen, pallidum and nucleus accumbens in 53 depressed patients (mean age: 44.1 years, 13.8 SD; 52% female) and 33 healthy controls (mean age: 39.1 years, 12.4 SD; 57% female). Patients were assessed before ECT, after their 2nd ECT and after completing an ECT treatment index. Controls were evaluated at two time points. Support vector machines determined if morphometric measures at baseline predicted ECT-related clinical response. Patients showed smaller baseline accumbens and pallidal volumes than controls ($p<.05$). Increases in left putamen volume ($p<.03$) occurred with ECT. Global increases in accumbens volume and local changes in pallidum and caudate volume occurred in patients defined as treatment responders. Morphometric changes were absent across time in controls. Baseline volume and shape metrics predicted overall response to ECT with up to 89% accuracy. Results support that ECT elicits structural plasticity in the dorsal and ventral striatum/pallidum. The morphometry of these structures, forming key components of limbic-

[4] The content of this chapter has been published as B. S. Wade, S. H. Joshi, S. Njau, A. M. Leaver, M. Vasavada, R. P. Woods, *et al*., "Effect of Electroconvulsive Therapy on Striatal Morphometry in Major Depressive Disorder," *Neuropsychopharmacology*, Apr 12 2016.

cortical-striatal-pallidal-thalamic circuitry involved in mood and emotional regulation, may determine patients likely to benefit from treatment.

Introduction

Major depression is one of the most common and economically burdensome psychiatric disorders (Kessler *et al*, 2003). Antidepressants and behavioral therapy are the most frequently prescribed treatments, but up to a third of patients remain unresponsive to initial treatment (Trivedi *et al*, 2006). With a rapid and high response rate, electroconvulsive therapy (ECT) is typically used after other failed treatments and can be particularly beneficial in suicidal, psychotic or catatonic depression (Kellner *et al*, 2012). However, the neural mechanisms underlying clinical response to ECT remain uncertain. To advance therapeutic development, research providing clearer understanding of the neural correlates underlying successful antidepressant response is crucial.

Current theories describe depression as a brain network disorder. Converging evidence suggests neural disturbances occur in a limbic-cortical-striatal-pallidal-thalamic circuit (Drevets *et al*, 2008). Structural alterations in the prefrontal cortex, particularly the anterior cingulate, and subcortical hippocampal, amygdalar, thalamic and striatal/pallidal centers are consistently implicated (Drevets *et al*, 2008; Lorenzetti *et al*, 2009; Schmaal *et al*, 2015). Lesion and functional imaging studies show these regions form networks governing mood regulation, reward sensitivity and emotion (Hamilton *et al*, 2013; Koenigs and Grafman, 2009; Korgaonkar *et al*, 2013; Ochsner *et al*, 2012). Symptoms of depression such as amotivation, anhedonia, apathy, and rumination are linked to functional disturbances in the ventral striatum/pallidum specifically (Disner *et al*, 2011; Kuhn *et al*, 2014; Ochsner *et al*, 2012). The ventral striatum, ventral pallidum and continuity with the ventral caudate nucleus and putamen - basal ganglia regions

with prominent limbic connections (Nieuwenhuys *et al*, 2008; Utter and Basso, 2008) - are themselves strongly interconnected, receive dopaminergic input from ventral midbrain regions (Haber and Knutson, 2010), and receive modulation by serotonergic midbrain pathways and other neurotransmitter systems (Di Matteo *et al*, 2008; Nieuwenhuys *et al*, 2008). The dorsal striatum, including the caudate nucleus, is involved in reward processing as relevant to depression symptomatology (Haber *et al*, 2010).

While less studied than the hippocampus and amygdala, basal ganglia substructures show lower volumes in meta-analyses of depression (Koolschijn *et al*, 2009; Videbech, 1997). Functional imaging studies demonstrate depression-related *hyporesponsivity* in striatal areas (Epstein *et al*, 2006; Smoski *et al*, 2009) and disturbances in fronto-striatal connectivity (Furman *et al*, 2011). Deficits in brain activation and functional connectivity in basal ganglia substructures are suggested to normalize with different antidepressant treatments (Admon *et al*, 2015; Stoy *et al*, 2012). In ECT-treated patients, we recently showed a *hyperconnectivity* between the ventral striatum and ventral default-mode network (DMN), while simultaneously demonstrating *hypoconnectivity* with the anterior DMN, patterns that were modulated by ECT (Leaver *et al*, 2015). These results suggest the striatum is involved in functional desynchronization between dorsal and ventral cortico-limbic neural circuits in major depression and that normalization of these functional disturbances can occur with ECT.

Hippocampal connections with the hypothalamic–pituitary–adrenal (HPA) axis, ventral striatal loop and dopaminergic mesolimbic system appear particularly relevant to the pathophysiology of major depression (Russo and Nestler, 2013). We and other groups have shown that ECT elicits increases in hippocampal (Abbott *et al*, 2014; Joshi *et al*, 2015; Nordanskog *et al*, 2010; Tendolkar *et al*, 2013) and amygdala volume (Joshi *et al*, 2015;

Tendolkar *et al*, 2013). However, whether structural plasticity occurs in the dorsal or ventral striatum/pallidum in association with treatment and illness recovery remains unknown. Since full response to ECT may be observed in only 2-4 weeks (Kellner *et al*, 2012), using ECT as a treatment model may identify predictors and correlates of response over shorter time intervals where effects are expected to overlap with antidepressant therapies. We thus performed volumetric and shape-based analyses to investigate if morphological changes are detectible before and after ECT in four constituents of the ventral basal ganglia: the caudate, putamen, pallidum, and nucleus accumbens. We compared patients to controls, and followed patients prospectively during an ECT treatment index series. Biomarkers predictive of treatment response could provide a major advance towards guiding clinical practice. We thus developed a machine-learning framework to determine if morphometric differences, prior to treatment, might predict patients' responsiveness to ECT. Based on our observations of restoration of functional connectivity (Leaver *et al*, 2015), we predicted that ECT-related structural plasticity would also occur in ventral striatal and connected basal ganglia regions.

Materials and Methods

Subjects

Participants included 53 patients experiencing a major depressive episode (28 females) recruited from individuals scheduled to receive ECT at the University of California, Los Angeles (UCLA) Resnick Neuropsychiatric Hospital. Diagnosis was determined by a board certified psychiatrist following Diagnostic Statistical Manual (DSM) IV-R criteria and additionally confirmed by the Mini-International Neuropsychiatric Interview (M.I.N.I.) (Sheehan *et al*, 1998). All patients had experienced two or more earlier major depressive episodes and failed to respond to at least two prior adequate medication trials in the index episode. Patients with comorbid

psychiatric disorders including schizophrenia, schizoaffective disorders, post-traumatic stress disorder, attention hyperactive deficit disorder, and dissociative disorders were excluded. Forty-five patients were diagnosed with unipolar depression and 8 with bipolar disorder, though mania in the index episode was exclusionary. Other exclusion criteria included dementia, first-episode depression, onset after 50 years, depression related to serious medical illness, or any neuromodulation treatment (e.g., vagal nerve stimulation, repetitive transcranial magnetic stimulation) within 6 months of the ECT index series. All patients were tapered off antidepressants and benzodiazepines in preparation for ECT and were completely free of medication for at least 48 to 72 hours before enrollment and ECT treatment.

Patients were scanned at three time points: (1) baseline, prior to and within 24 hours of the initial ECT session [T1]; (2) after the 2nd ECT session [T2, occurring 36-48 hours after baseline assessment and before the 3rd ECT] and (3) within a week of completing the ECT treatment index series [T3, as individually determined based on stabilization of mood, approximately 4-6 weeks after 1st treatment]. Of the 53 patients completing baseline, 45 completed T2, and 34 completed T3 assessments. Attrition was primarily due to early discontinuation of ECT, inability to come in for or to tolerate repeat scanning and scanner hardware failures.

Thirty-three controls (19 females) with similar demographics to patient participants were recruited from the same geographical area using advertisements. Controls received M.I.N.I. (Sheehan *et al*, 1998) screening to exclude history of depression, other psychiatric or medical illness, or a history of antidepressant use. Controls were scanned at two time points approximately 4-6 weeks apart. Additional exclusion criteria for all participants included history of alcohol or substance abuse within the past 6 months or dependence in the past 12 months, any

neurological disorder, and contraindication to MRI scanning. **Table 5-1** summarizes the demographic and clinical characteristics of our cohort. Subjects in this study overlap with those in two recent investigations of hippocampal and amygdala morphometry (Joshi *et al*, 2015) and functional connectivity (Leaver *et al*, 2015). All participants provided written informed consent as approved by the UCLA Institutional Review Board.

ECT treatment

ECT (5000Q MECTA Corp.) was administered three times a week, using standard protocols for anesthesia (methohexital at 1mg/kg dosage) and paralysis (succinylcholine at 1mg/kg dosage). ECT followed the seizure threshold (ST) titration method: after establishing the ST, treatments were delivered at 5x ST for right unilateral (RUL) d'Elia lead placement, using an ultra brief pulse-width (0.3msec), and at 1.5x ST for bilateral placement, using a brief pulse-width (0.5msec).

Mood ratings

The Montgomery-Åsberg (MADRS) (Montgomery and Asberg, 1979), Hamilton (HAM-D-17) (Hamilton, 1976) depression rating scales and the Quick Inventory of Depressive Symptomology Self Report (QIDS-SR) (Rush *et al*, 2003) were collected at the same time points as brain scanning. Patients were defined as treatment responders if they showed greater than 50% improvement in symptoms on the HAM-D. We additionally report differences in patients who responded with greater than 50% improvement across all mood scales.

Image Acquisition: High-resolution multi-echo T1-weighted MPRAGE images with real time motion correction using navigators (Tisdall *et al*, 2012) were acquired on Siemens 3T Allegra

(Erlangen, Germany) system (TEs/TR=1.74, 3.6, 5.46, 7.32/2530 ms, TI=1260 ms, FA=7°, FOV=256x256 mm, 192 sagittal slices, voxel resolution=1.3×1.0×1.0 mm^3).

Image preprocessing and segmentation

Each T1-weighted image was processed and volumetrically quantified using the Freesurfer suite (version 5.3.0), which is documented and freely available online (http://surfer.nmr.mgh.harvard.edu/). Preprocessing steps included correction for magnetic field inhomogeneities, removal of non-brain tissue and disconnection and segmentation of subcortical regions-of-interest (ROIs) including the bilateral putamen, pallidum, caudate and nucleus accumbens in each subject and time point. All segmentations were visually inspected and manually corrected for minor topographic errors if needed. Intraclass correlation coefficients for each region from control subjects scanned 4-6 weeks apart indicated high concordance (accumbens=.77; pallidum=.80; putamen=.84 and caudate=.93). **Figure 5-1** illustrates the locations of the caudate, putamen, pallidum and accumbens.

Surface-based analysis

To investigate local group-level variation in subcortical anatomy the segmented structures were transformed to a parameterized mesh surface using methods detailed in (Gutman *et al*, 2015). Briefly, each surface was conformally mapped to the spherical domain and rigidly rotated to a probabilistic atlas. Spherical Demons (SD) (Gutman *et al*, 2013) then non-linearly registered the spherical maps based on curvature profiles. Two surface-based functions were defined: (1) the global orientation function, defining the direction of the surface and, (2) the local thickness of the surface with respect to a skeletonized medial core. SD was implemented using both the medial core and curvature to match each surface to the atlas. In this parameterization, two shape features are defined at each vertex: (1) radial distance (RD), a proxy for thickness and

(2) the Jacobian determinant (JD) which indicates surface area dilation or contraction. The number of vertices for each surface scales with the average structure volume maintaining uniform resolution across structures (vertex counts: accumbens=930, caudate=2502, putamen=2502 and pallidum=1254).

Statistical Analysis

Statistical analyses addressed (1) cross-sectional differences between patients and controls at baseline, (2) longitudinal effects of ECT (or time in control subjects), (3) cross-sectional differences between ECT responders and non-responders and (4) predictors of ECT-related clinical response (using baseline imaging measures only). To reduce the number of comparisons while allowing for estimation of lateralized effects, hemisphere was included as a repeated measure in all volumetric analyses (implemented in IBM SPSS Statistics, v22). Shape-based analyses (executed in R; https://www.r-project.org) used the same statistical models except they were conducted in each hemisphere separately to allow for examination of focal effects.

Analysis #1 above used the General Linear Model (GLM) including sex, age, and brain volume as covariates to determine cross-sectional effects of diagnosis (comparing baseline measures between patients and controls). Analysis #2 used the General Linear Mixed Model (GLMM), which models the correlation structure of repeated measurements while leveraging the statistical power gained using each subject as their own control, to determine longitudinal effects of ECT. These models, which allow for unbiased parameter estimates despite missing time points, included subject as a random effect and sex, age and brain volume as covariates. Individual time points were compared pairwise for measures showing significant main effects of ECT. Analysis #3 used the GLM to determine whether change in morphometry over the course of ECT differed in treatment responders and non-responders. Since difference scores (change in

morphometric measures and change in mood scores) were examined, only patients completing all time points (n=34) were examined. Age and sex were included as covariates.

To determine if baseline morphometry predicts ECT response based on the combined and individual mood scales (examined separately), analysis #4 used support vector machines (SVM), a supervised machine-learning algorithm. Leave-one-out cross validation was used to assess the performance of SVMs using a combined feature set of all baseline volume and shape measures. SVMs fit an optimal hyperplane in an n-dimensional feature space to separate labels matching input features. Our SVMs used radial kernels to model non-linear decision boundaries (Sánchez A, 2003). SVMs using radial kernels were compared to linear SVMs using DeLong's test for two receiver operating characteristic curves (ROCs). Though the area under the curve (AUC) between the radial and linear SVMs was not significantly different, radial AUC was larger, thus the radial kernel was used. Grid search was used to find optimal combinations of the SVM cost and gamma parameters. Features were scaled to zero mean and unit variance. The significance of each SVM model was assessed using permutation tests achieved by comparing the observed AUC to a distribution of 1000 simulated AUCs derived from fitting SVMs to randomly shuffled labels. The proportion of permuted models with AUCs larger than the observed AUC provided the permutation p-value.

Based on our *a priori* hypotheses derived from prior findings showing ECT-related changes of functional connectivity in the striatum/pallidum with ECT (Leaver *et al*, 2015), a two-tailed alpha level of .05 was the threshold for significance for volumetric analyses. Surface-based analyses controlled for false positives using False Discovery Rate (FDR) (Benjamini and Hochberg, 1995) using a 5% false positive rate, surface wise.

Finally, *post-hoc* analyses were performed to test for differences between patients diagnosed with unipolar (n=45) or bipolar depression (n=8) and possible lead-placement effects (the % of ECT sessions using RUL) for measures showing significant ECT effects. As lead placement was clinically determined (American Psychiatric Association. Committee on Electroconvulsive Therapy. and Weiner), effects of lead placement were examined while controlling for baseline mood scores.

Results

Demographic and clinical effects

Sex, X^2 (1, 85)=.18, p=.66, and age, F(1, 85)=2.67, p=.11 distributions were similar in ECT patients and controls. MADRS, HAM-D and QIDS rating scales showed highly significant effects of ECT, F(2, 36.75)=38.66, F(2, 38.16)=32.74, F(2, 36.81)=37.60; all p<.0001, respectively. Demographic and clinical details for each group and time point are provided in **Table 5-1**.

Cross-sectional effects of diagnosis

Volumetric analyses showed smaller volumes of the nucleus accumbens, F(1, 81)=4.67, p=.034, -8.0% and pallidum, F(1,81)=3.96, p=.05, -4.9% in patients relative to controls at baseline. Cross-sectional effects were non-significant for the putamen, F(1, 82.04)=2.76, p=.101 and caudate F(1, 80.70)=.095, p=.76 and no region showed hemispheric interactions. Means for each diagnostic group and time point are plotted in **Figure 5-2**. No significant between-group shape variation was observed.

Longitudinal effects of ECT

A significant volumetric association with ECT, F(2, 42.80)=5.36, p=.008 and ECT by hemisphere interaction was observed for the putamen, F(1, 44.17)=3.40, p=.042. A significant increase in left putamen volume occurred with ECT, F(1, 39.83)=3.57, p=.038, 2.4%. Pairwise comparisons of time points revealed significant volume increases between T1 and T3, p=.01 (**Figure 5-2**). Regional shape changes were non-significant for all 4 substructures, though statistical maps, shown in **Figure 5-3,** suggest more diffuse surface expansion with ECT. Effects of time in control subjects were non-significant for both shape and volume.

Effects of morphometric change with clinical response

Significant effects of response status were observed for the volume of the accumbens, F(1, 28)=4.29, p=.048 where responders showed volumetric gain, F(2,18.98)=9.18, p=.002, with no change in non-responders (p>.05). There was a significant effect of response status for change in caudate volume over time, F(1,29.03)=4.29, p=.048. Though volumes tended to increases over time in responders and decrease over time in non-responders, these effects were non-significant within group (both p>.05). Significant regional increases in caudate morphometry were observed with the JD of the left superior and inferior caudate increasing in HAM-D responsive patients and decreasing in non-responsive patients over time. Finally, local decreases in the posterior medial aspect of the right pallidum for RD and JD were present in responders at time point 3. **Figure 5-4** shows significant volume and shape differences by ECT-response.

Baseline predictive effects

Using the entire combined set of baseline shape and volume features, SVM prediction of clinical outcome using the combined mood scale resulted in 90% AUC (95% CI: 68 - 93%, p=0.000), a maximum accuracy (MA) of 89%. Response prediction for individual mood scales yielded 54% AUC (95% CI 29–78%; p=0.599, MA=72%) for HAM-D ; 59% AUC (95% CI 36–

80%; p=0.392, MA=68%) for MADRS and 84% AUC (95% CI 64–93%; p=0.001, MA=75%) for QIDS. **Figure 5-5a** plots the ROC curves associated with each SVM while **Figure 5-5b** plots the associated accuracy, sensitivity and specificity values across a range of decision thresholds. As a post-hoc analysis we investigated the performance of SVMs using metric-specific features in the prediction of response. With performances averaged across mood scales, RD-specific features yielded a mean of 77%, JD 63% and volume 60% AUC. Because overfitting with high-dimensional features is a common problem we tested whether LASSO feature selection, implemented within each cross validation fold, would significantly affect classifier performance. LASSO retained an average of 2 features and provided an AUC of 76%, which did not significantly differ from the full-feature SVM (p=0.226).

Post-hoc analyses of diagnostic category and ECT lead placement

There were no significant differences for volume or shape when comparing unipolar versus bipolar depression. Associations with the proportion of RUL treatments given across the ECT index series also failed to show significant effects for volume or shape.

Discussion

Our study addressed whether ECT impacts the morphometry of four components of the dorsal and ventral basal ganglia that are known to play a role in cognitive and affective function of high relevance to depression: the accumbens, putamen, pallidum and caudate. Each structure's morphometry was modeled using global volumetric and local descriptions of shape variation. Exploring effects of diagnosis and treatment we contrasted ROI morphometry between patients and controls at baseline, in patients across the course of ECT, and between patient responders and non-responders. Finally, we showed that patients' responsiveness to ECT could be predicted from baseline brain morphometry using machine learning.

Cross-sectionally, we observed reduced accumbens and pallidum volumes in patients prior to treatment. This corroborates prior reports of lower striatal volumes in depressed cohorts (Koolschijn *et al*, 2009; Videbech, 1997). We did not detect shape differences between patients and controls, so volumetric differences may be more globally dispersed than focal. Several longitudinal patterns emerged. The left putamen volume increased between baseline and the end of the ECT treatment index. We did not observe significant ECT effects for morphometry in other ROIs. Differential patterns of morphometry were observed within patients based on their responsiveness to ECT. The accumbens volume significantly increased over the course of ECT [**Figure 5-4**(a)]. However, effects in the right medial pallidum suggested more localized volume reductions in responders.

Cumulatively, the above findings support that structural deficits in striatal and paleostriatal structures occur in major depression and ECT leads to neuroplasticity in these regions. While the basal ganglia play pivotal roles in psychomotor function, these regions are also densely connected with proximal limbic regions including the hippocampus and amygdala (Nieuwenhuys *et al*, 2008). Since there is typically a lengthy delay between the initiation of standard antidepressant therapies and clinical response, biomarkers that may help guide future treatment decisions may have substantial clinical impact. Using SVMs to learn differential patterns of brain morphometry between responsive and non-responsive patients, we predicted patient response with up to 89% accuracy when defining response across all mood scales. Some demographic and clinical factors, such as the presence of psychotic symptoms, have been associated with improved ECT response (Petrides *et al*, 2001). Yet, without any other basis for determining potential outcome, an 89% predictive value may be very beneficial, particularly if this prediction generalizes to other forms of antidepressant treatment.

ECT promoted a volumetric increase or local surface deformations in the striatum over short time intervals (4-6 weeks). A leading hypothesis regarding the mechanisms underlying major depression is that neurotrophic factors are adversely affected. This is supported by observations that antidepressant treatments influence transduction pathways associated with neuronal plasticity (Duman, 2002). For example, electroshock - the animal model of ECT - stimulates neurogenesis in the hippocampus of rodents (Malberg *et al*, 2000) and non-human primates (Perera *et al*, 2007). As adult neurogenesis occurs in the hippocampal dentate gyrus, in line with a neurotrophic model of antidepressant response (Fosse and Read, 2013; Kellner *et al*, 2012), several prior structural imaging studies of ECT in humans showed ECT-related increases in hippocampal volume (Abbott *et al*, 2014; Duman, 2002; Jorgensen *et al*, 2015; Nordanskog *et al*, 2010; Tendolkar *et al*, 2013). In a sample overlapping with the current study, we also observed changes in hippocampal morphometry with ECT and relationships with symptom improvement (Joshi *et al*, 2015). Notably, Inta et al. (Inta and Gass, 2015) reported ECT-triggered neurogenesis in striatal and frontal brain regions following ECT in a rat model suggesting that cell proliferation extends beyond the hippocampus. Others (Liu *et al*, 2009) have also reported increased subventricular zone neuroblast cell proliferation to striatal areas following seizures. Further, ECT-related structural neuroplasticity is shown in the amygdala (Joshi *et al*, 2015; Tendolkar *et al*, 2013). These subcortical limbic structures are intricately connected to the striatum, and via the cortico-striatal-pallido-thalamo-cortical loop and projections to the hypothalamus and brainstem, act together to influence emotional expression and motivation (Cardinal *et al*, 2002).

Additional mechanisms may account for ECT-related neuroplasticity. These include an increase in monoamine neurotransmitter production, release of hypothalamic hormones,

increased angiogenesis (Wennstrom *et al*, 2006) glial cell activation (Jansson *et al*, 2009) and gliogenesis (Wennstrom *et al*, 2006). The ventral striatum and parts of the dorsal striatum form part of the mesolimbic dopaminergic pathway involved in reward processing. Patients with depression frequently show diminished ability to derive pleasure or positive motivation from rewarding stimuli leading to symptoms of anhedonia (Zhang *et al*, 2013). Disease-related abnormalities in reward processing are characterized as reflecting "reward *hyposensitivity*", and brain activation studies typically show hypoactivation in striatal and prefrontal regions (Forbes *et al*, 2009; Zhang *et al*, 2013). Human neuroimaging studies also demonstrate that disturbed regulation between regions involved in reward processing occur via the serotonin transporter (Hahn *et al*, 2014). Preclinical studies further show that anxiety and depressive-like behavior associate with lower levels of serotonin and norepinephrine in the striatum (Brenes *et al*, 2008) where serotonergic and adrenergic systems are targets of commonly prescribed antidepressants. Though it is possible that changes in striatal morphometry may be influenced by anesthesia rather than by treatment-related effects, observations of change in responders vs. non-responders makes this less likely.

Because shape-based descriptors are less commonly used than volumetric descriptions of brain structures we endeavored to demonstrate their value as both predictors in the SVM and a descriptor of morphometry. In the context of classification we compared use of RD-only, JD-only and volume-only features and showed the average performance of SVMs using shape-based descriptors was higher than those using volume-only. Overfitting is another concern when using high-dimensional features. Thus we compared an SVM using all features to a LASSO subset. AUC did not significantly differ between these models therefore it is unlikely that significant

overfitting occurred with the full feature set, however, this may be confirmed with a larger sample.

The value of shape-based approaches is their ability to reveal local variation in surface topology rather than simply identify gross volumetric variation. This is particularly valuable since we did not segment sub-nuclei of subcortical structures. The locality of the shape measures could thus inform future studies using subfield measurements. A related concern is that shape and volume are highly correlated. Indeed, the average correlation between RD and volume was r=0.37 and JD and volume r=0.44; however, this is expected since the measures are of the same structure. The value of the descriptors' combined use lies in their ability to reveal separate, complementary aspects of the structure's topology.

Placed in the context of existing literature, ECT-related structural neuroplasticity in basal ganglia substructures could be attributed to neurotrophic factors that include cell and/or synaptic proliferation possibly linked to changes in monoaminergic neurotransmitter systems that form part of prefrontal-striatal-limbic circuitry. Though this is the first study to our knowledge to show that ECT affects the morphometry of the striatum and paleostriatum, several limitations exist. First, despite *a priori* hypotheses justifying the study of these regions, these findings warrant independent replication. Since morphometry of subcortical regions are highly variable even in normal populations, this variability may have impacted our ability to detect local shape changes. Finally, though we investigated relationships with changes in overall symptom ratings in the current study, it is possible that ECT-related neuroplasticity may be more closely related to specific symptoms such as anhedonia, apathy, amotivation and rumination as have been linked with altered striatal circuitry in functional imaging studies.

Our findings provide new evidence to support that ECT induces neuroplastic changes in

striatal regions in addition to other subcortical limbic regions. We also demonstrate that these changes are associated with clinical improvement and have the potential to predict an affected individual's treatment response using machine learning based solely on imaging features.

Acknowledgements

Chapter 5 is a version of Wade BS, Joshi SH, Njau S, Leaver AM, Vasavada M, Woods RP, Gutman BA, Thompson PM, Espinoza R, Narr KL. (2016). Effect of Electroconvulsive Therapy on Striatal Morphometry in Major Depressive Disorder. *Neuropsychopharmacology : official publication of the American College of Neuropsychopharmacology* **41**(10): 2481-2491.

Shantanu Joshi, Amber Leaver, Megha Vasavada, Roger Woods and Randal Espinoza aided in data analysis and interpretation of the findings. Stephanie Njau aided in data management. Boris Gutman developed the shape modeling used in this study. Katherine Narr and Paul Thompson were PIs of the study.

This study was supported by award number R01MH092301 from the National Institute of Mental Health supported this study. This work is also supported in part by NIH 'Big Data to Knowledge' (BD2K) Center of Excellence grant U54 EB020403, funded by a cross-NIH consortium including NIBIB and NCI and by the National Science Foundation Graduate Research Fellowship under Grant No. DGE-0707424.

References

Abbott CC, Jones T, Lemke NT, Gallegos P, McClintock SM, Mayer AR*, et al* (2014). Hippocampal structural and functional changes associated with electroconvulsive therapy response. *Transl Psychiatry* **4**: e483.

Admon R, Nickerson LD, Dillon DG, Holmes AJ, Bogdan R, Kumar P*, et al* (2015). Dissociable cortico-striatal connectivity abnormalities in major depression in response to monetary gains and penalties. *Psychological medicine* **45**(1): 121-131.

American Psychiatric Association. Committee on Electroconvulsive Therapy., Weiner RD (2001). *The practice of electroconvulsive therapy : recommendations for treatment, training, and privileging : a task force report of the American Psychiatric Association*, 2nd edn. American Psychiatric Association: Washington, D.C., viii, 355 p.pp.

Benjamini Y, Hochberg Y (1995). Controlling the false discovery rate: a practical and powerful approach to multiple testing. *Journal of the Royal Statistical Society Series B (Methodological)*: 289-300.

Brenes JC, Rodriguez O, Fornaguera J (2008). Differential effect of environment enrichment and social isolation on depressive-like behavior, spontaneous activity and serotonin and norepinephrine concentration in prefrontal cortex and ventral striatum. *Pharmacology, biochemistry, and behavior* **89**(1): 85-93.

Cardinal RN, Parkinson JA, Hall J, Everitt BJ (2002). Emotion and motivation: the role of the amygdala, ventral striatum, and prefrontal cortex. *Neuroscience and biobehavioral reviews* **26**(3): 321-352.

Di Matteo V, Pierucci M, Esposito E, Crescimanno G, Benigno A, Di Giovanni G (2008). Serotonin modulation of the basal ganglia circuitry: therapeutic implication for Parkinson's disease and other motor disorders. *Progress in brain research* **172**: 423-463.

Disner SG, Beevers CG, Haigh EA, Beck AT (2011). Neural mechanisms of the cognitive model of depression. *Nat Rev Neurosci* **12**(8): 467-477.

Drevets WC, Price Jl Fau - Furey ML, Furey ML (2008). Brain structural and functional abnormalities in mood disorders: implications for neurocircuitry models of depression. (1863-2653 (Print)).

Duman RS (2002). Pathophysiology of depression: the concept of synaptic plasticity. *European psychiatry : the journal of the Association of European Psychiatrists* **17 Suppl 3**: 306-310.

Epstein J, Pan H, Kocsis JH, Yang Y, Butler T, Chusid J*, et al* (2006). Lack of ventral striatal response to positive stimuli in depressed versus normal subjects. *Am J Psychiatry* **163**(10): 1784-1790.

Forbes EE, Hariri AR, Martin SL, Silk JS, Moyles DL, Fisher PM*, et al* (2009). Altered striatal activation predicting real-world positive affect in adolescent major depressive disorder. *Am J Psychiatry* **166**(1): 64-73.

Fosse R, Read J (2013). Electroconvulsive treatment: hypotheses about mechanisms of action. *Frontiers in psychiatry* **4**.

Furman DJ, Hamilton JP, Gotlib IH (2011). Frontostriatal functional connectivity in major depressive disorder. *Biology of mood & anxiety disorders* **1**(1): 11-11.

Gutman B, Jahanshad N, Ching C, Wang Y, Kochunov P, Nichols T*, et al* (2015). Medial Demons Registration Localizes the Degree of Genetic Influence over Subcortical Shape Variability: An N= 1480 Meta-Analysis. *International Symposium on Biomedical Imaging*.

Gutman BA, Madsen SK, Toga AW, Thompson PM (2013). *A family of fast sphericalregistration algorithms for cortical chapes in Multimodal brain image analysis*, xi, 260 pagespp.

Haber SN, Knutson B (2010). The reward circuit: linking primate anatomy and human imaging. *Neuropsychopharmacology : official publication of the American College of Neuropsychopharmacology* **35**(1): 4-26.

Hahn A, Haeusler D, Kraus C, Hoflich AS, Kranz GS, Baldinger P*, et al* (2014). Attenuated serotonin transporter association between dorsal raphe and ventral striatum in major depression. *Human brain mapping* **35**(8): 3857-3866.

Hamilton JP, Chen MC, Gotlib IH (2013). Neural systems approaches to understanding major depressive disorder: an intrinsic functional organization perspective. *Neurobiology of disease* **52**: 4-11.

Hamilton M (1976). Hamilton depression scale. *ECDEU assessment manual for psychopharmacology*. NIMH Rockville, MD, pp 179-192.

Inta D, Gass P (2015). Is forebrain neurogenesis a potential repair mechanism after stroke? *Journal of cerebral blood flow and metabolism : official journal of the International Society of Cerebral Blood Flow and Metabolism* **35**(7): 1220-1221.

Jansson L, Wennstrom M, Johanson A, Tingstrom A (2009). Glial cell activation in response to electroconvulsive seizures. *Progress in neuro-psychopharmacology & biological psychiatry* **33**(7): 1119-1128.

Jorgensen A, Magnusson P, Hanson LG, Kirkegaard T, Benveniste H, Lee H*, et al* (2015). Regional brain volumes, diffusivity, and metabolite changes after electroconvulsive therapy for severe depression. *Acta Psychiatr Scand*.

Joshi SH, Espinoza RT, Pirnia T, Shi J, Wang Y, Ayers B*, et al* (2015). Structural Plasticity of the Hippocampus and Amygdala Induced by Electroconvulsive Therapy in Major Depression. *Biological psychiatry*.

Kellner CH, Greenberg RM, Murrough JW, Bryson EO, Briggs MC, Pasculli RM (2012). ECT in treatment-resistant depression. *Am J Psychiatry* **169**(12): 1238-1244.

Kessler RC, Berglund P, Demler O, et al. (2003). The epidemiology of major depressive disorder: Results from the national comorbidity survey replication. *JAMA* **289**(23): 3095-3105.

Koenigs M, Grafman J (2009). The functional neuroanatomy of depression: distinct roles for ventromedial and dorsolateral prefrontal cortex. *Behavioural brain research* **201**(2): 239-243.

Koolschijn PC, van Haren NE, Lensvelt-Mulders GJ, Hulshoff Pol HE, Kahn RS (2009). Brain volume abnormalities in major depressive disorder: a meta-analysis of magnetic resonance imaging studies. *Human brain mapping* **30**(11): 3719-3735.

Korgaonkar MS, Grieve SM, Etkin A, Koslow SH, Williams LM (2013). Using standardized fMRI protocols to identify patterns of prefrontal circuit dysregulation that are common and specific to cognitive and emotional tasks in major depressive disorder: first wave results from the iSPOT-D study. *Neuropsychopharmacology : official publication of the American College of Neuropsychopharmacology* **38**(5): 863-871.

Kuhn S, Vanderhasselt MA, De Raedt R, Gallinat J (2014). The neural basis of unwanted thoughts during resting state. *Social cognitive and affective neuroscience* **9**(9): 1320-1324.

Leaver AM, Espinoza R, Joshi SH, Vasavada M, Njau S, Woods RP*, et al* (2015). Desynchronization and Plasticity of Striato-frontal Connectivity in Major Depressive Disorder. *Cereb Cortex*.

Liu F, You Y, Li X, Ma T, Nie Y, Wei B*, et al* (2009). Brain injury does not alter the intrinsic differentiation potential of adult neuroblasts. *The Journal of neuroscience : the official journal of the Society for Neuroscience* **29**(16): 5075-5087.

Lorenzetti V, Allen NB, Fornito A, Yucel M (2009). Structural brain abnormalities in major depressive disorder: A selective review of recent MRI studies. *Journal of affective disorders* **117**(1-2): 1-17.

Malberg JE, Eisch AJ, Nestler EJ, Duman RS (2000). Chronic antidepressant treatment increases neurogenesis in adult rat hippocampus. *The Journal of neuroscience : the official journal of the Society for Neuroscience* **20**(24): 9104-9110.

Montgomery SA, Asberg M (1979). A new depression scale designed to be sensitive to change. *The British journal of psychiatry : the journal of mental science* **134**: 382-389.

Nieuwenhuys R, Voogd J, Huijzen Cv (2008). *The human central nervous system*, 4th edn. Springer: Berlin ; New York, xiv, 967 p.pp.

Nordanskog P, Dahlstrand U, Larsson MR, Larsson EM, Knutsson L, Johanson A (2010). Increase in hippocampal volume after electroconvulsive therapy in patients with depression: a volumetric magnetic resonance imaging study. *J ECT* **26**(1): 62-67.

Ochsner KN, Silvers JA, Buhle JT (2012). Functional imaging studies of emotion regulation: a synthetic review and evolving model of the cognitive control of emotion. *Annals of the New York Academy of Sciences* **1251**: E1-24.

Perera TD, Coplan JD, Lisanby SH, Lipira CM, Arif M, Carpio C*, et al* (2007). Antidepressant-induced neurogenesis in the hippocampus of adult nonhuman primates. *The Journal of neuroscience : the official journal of the Society for Neuroscience* **27**(18): 4894-4901.

Petrides G, Fink M, Husain MM, Knapp RG, Rush AJ, Mueller M*, et al* (2001). ECT remission rates in psychotic versus nonpsychotic depressed patients: a report from CORE. *The journal of ECT* **17**(4): 244-253.

Rush AJ, Trivedi MH, Ibrahim HM, Carmody TJ, Arnow B, Klein DN*, et al* (2003). The 16-Item Quick Inventory of Depressive Symptomatology (QIDS), clinician rating (QIDS-C), and self-report (QIDS-SR): a psychometric evaluation in patients with chronic major depression. *Biological psychiatry* **54**(5): 573-583.

Russo SJ, Nestler EJ (2013). The brain reward circuitry in mood disorders. *Nat Rev Neurosci* **14**(9): 609-625.

Sánchez A VD (2003). Advanced support vector machines and kernel methods. *Neurocomputing* **55**(1–2): 5-20.

Schmaal L, Veltman DJ, van Erp TG, Samann PG, Frodl T, Jahanshad N*, et al* (2015). Subcortical brain alterations in major depressive disorder: findings from the ENIGMA Major Depressive Disorder working group. *Mol Psychiatry*.

Sheehan DV, Lecrubier Y, Sheehan KH, Amorim P, Janavs J, Weiller E*, et al* (1998). The Mini-International Neuropsychiatric Interview (M.I.N.I.): the development and validation of a structured diagnostic psychiatric interview for DSM-IV and ICD-10. *J Clin Psychiatry* **59 Suppl 20**: 22-33;quiz 34-57.

Smoski MJ, Felder J, Bizzell J, Green SR, Ernst M, Lynch TR*, et al* (2009). fMRI of alterations in reward selection, anticipation, and feedback in major depressive disorder. *Journal of affective disorders* **118**(1-3): 69-78.

Stoy M, Schlagenhauf F, Sterzer P, Bermpohl F, Hagele C, Suchotzki K*, et al* (2012). Hyporeactivity of ventral striatum towards incentive stimuli in unmedicated depressed

patients normalizes after treatment with escitalopram. *Journal of psychopharmacology* **26**(5): 677-688.

Tendolkar I, van Beek M, van Oostrom I, Mulder M, Janzing J, Voshaar RO*, et al* (2013). Electroconvulsive therapy increases hippocampal and amygdala volume in therapy refractory depression: a longitudinal pilot study. *Psychiatry research* **214**(3): 197-203.

Tisdall MD, Hess AT, Reuter M, Meintjes EM, Fischl B, van der Kouwe AJ (2012). Volumetric navigators for prospective motion correction and selective reacquisition in neuroanatomical MRI. *Magnetic resonance in medicine : official journal of the Society of Magnetic Resonance in Medicine / Society of Magnetic Resonance in Medicine* **68**(2): 389-399.

Trivedi MH, Rush AJ, Wisniewski SR, Nierenberg AA, Warden D, Ritz L*, et al* (2006). Evaluation of outcomes with citalopram for depression using measurement-based care in STAR*D: implications for clinical practice. *Am J Psychiatry* **163**(1): 28-40.

Utter AA, Basso MA (2008). The basal ganglia: an overview of circuits and function. *Neuroscience and biobehavioral reviews* **32**(3): 333-342.

Videbech P (1997). MRI findings in patients with affective disorder: a meta-analysis. *Acta Psychiatr Scand* **96**(3): 157-168.

Wennstrom M, Hellsten J, Ekstrand J, Lindgren H, Tingstrom A (2006). Corticosterone-induced inhibition of gliogenesis in rat hippocampus is counteracted by electroconvulsive seizures. *Biological psychiatry* **59**(2): 178-186.

Zhang WN, Chang SH, Guo LY, Zhang KL, Wang J (2013). The neural correlates of reward-related processing in major depressive disorder: a meta-analysis of functional magnetic resonance imaging studies. *Journal of affective disorders* **151**(2): 531-539.

Tables

Table 5-1. Demographic and Clinical Characteristics

	Patients, N = 53	**Controls, N = 33**
Age, mean (SD), y	44.1 (13.8)	39.3 (12.4)
Gender (M/F)	25/28	14/19
Race/ethnicity		
African American	3	3
Asian	4	3
Hispanic	6	2
White	38	24
Multi-ethnic	1	1
Adjusted education, y	15.78 (2.70)	16.94 (2.30)
Dextral/non-dextral [a]	37/12	28/4
Clinical Information		
RUL/mixed lead placement/bilateral [b]	27/6/1	
Unipolar/bipolar	45/8	--
Percent Responders/non-responders [c]	35/65	
Age at onset, mean (SD), y	24.26 (12.54)	--
Current episode, mean (SD), y	2.31 (4.81)	--
Lifetime illness, mean (SD), y	18.53 (13.27)	--
	Responders, N = 20	**Non-Responders, N = 14**
Age, mean (SD), y	44.9 (12.6)	37.2 (14.6)
Gender (M/F)	12/8	6/8
Race/ethnicity		
African American	1	1
Asian	1	3
Hispanic	2	2
White	15	8
Multi-ethnic	1	0
Adjusted education, y	10.1 (2.4)	9.6 (2.9)
Clinical Information		
# of ECT Index sessions, mean (SD)	10.35 (2.34)	13.0 (3.53)
# of ECT Index sessions, range	6-15	8-22
Unipolar/bipolar	16/4	12/2
Age at onset, mean (SD), y	26.84 (14.64)	20.07 (10.94)
Current episode, mean (SD), y	1.94 (3.04)	2.52 (3.63)
Lifetime illness, mean (SD), y	17.65 (11.30)	15.21 (11.63)

Time point	T1, N=53	T2, N=45	T3, N=34	C1, N=33	C2, N=31
HAM-D	24.34 (6.16)*	20.20 (6.23)†	12.46(8.04) ‡	--	--
QIDS-SR	20.60 (4.02)*	16.75 (5.47)†	10.82 (6.55)‡	--	--
MADRS	38.44 (9.31)*	31.47 (9.55)†	17.08 (11.94)‡	--	--

Abbreviations: T1: Patient baseline; T2: After the 2nd ECT; T3: After the ECT index series; C1: Control baseline; C2: Control follow-up; RUL: Right unilateral lead placement; HAM-D-17: Hamilton Rating Scale for Depression; QIDS-SR-16: Quick Inventory of Depressive Symptomatology – Self-Report; MADRS: Montgomery – Åsberg Depression Rating Scale. [a]Handedness was estimated using the modified Edinburgh Handedness Inventory (Oldfield, 1971) where a laterality quotient of < .7 defined non-dextrals. [b] Lead placement for patients completing all 3 time points. [r]esponse defined as >50% improvement in HAM-D scores over the course of treatment *Significant effect between T1 and T2, †significant effect between T2 and T3; ‡significant effect between T1 and T3.

Figures

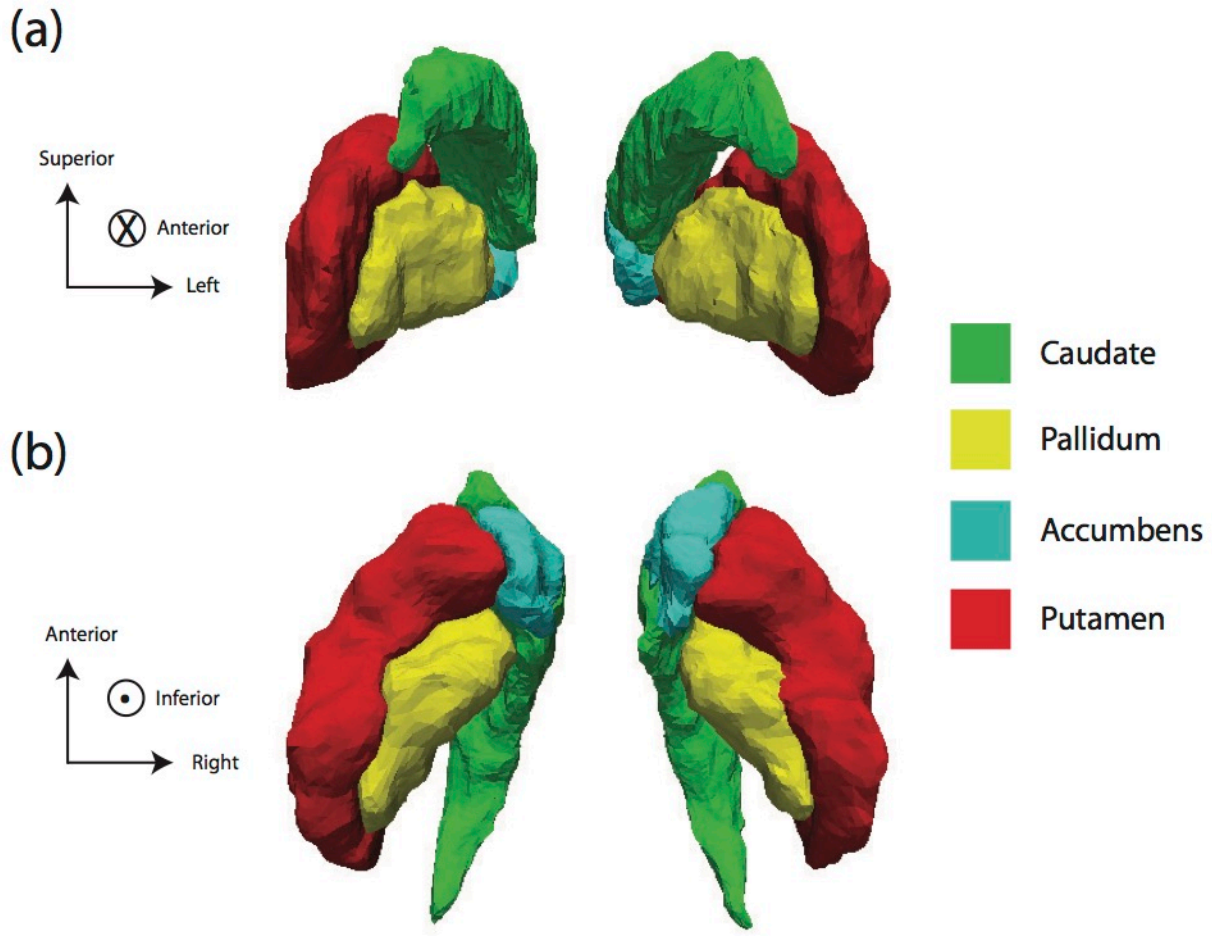

Figure 5-1. Subcortical structures including the putamen, pallidum and nucleus accumbens extracted from each MRI volume from (a) posterior and (b) superior perspectives. Images are in radiological orientation, i.e. left-right flipped.

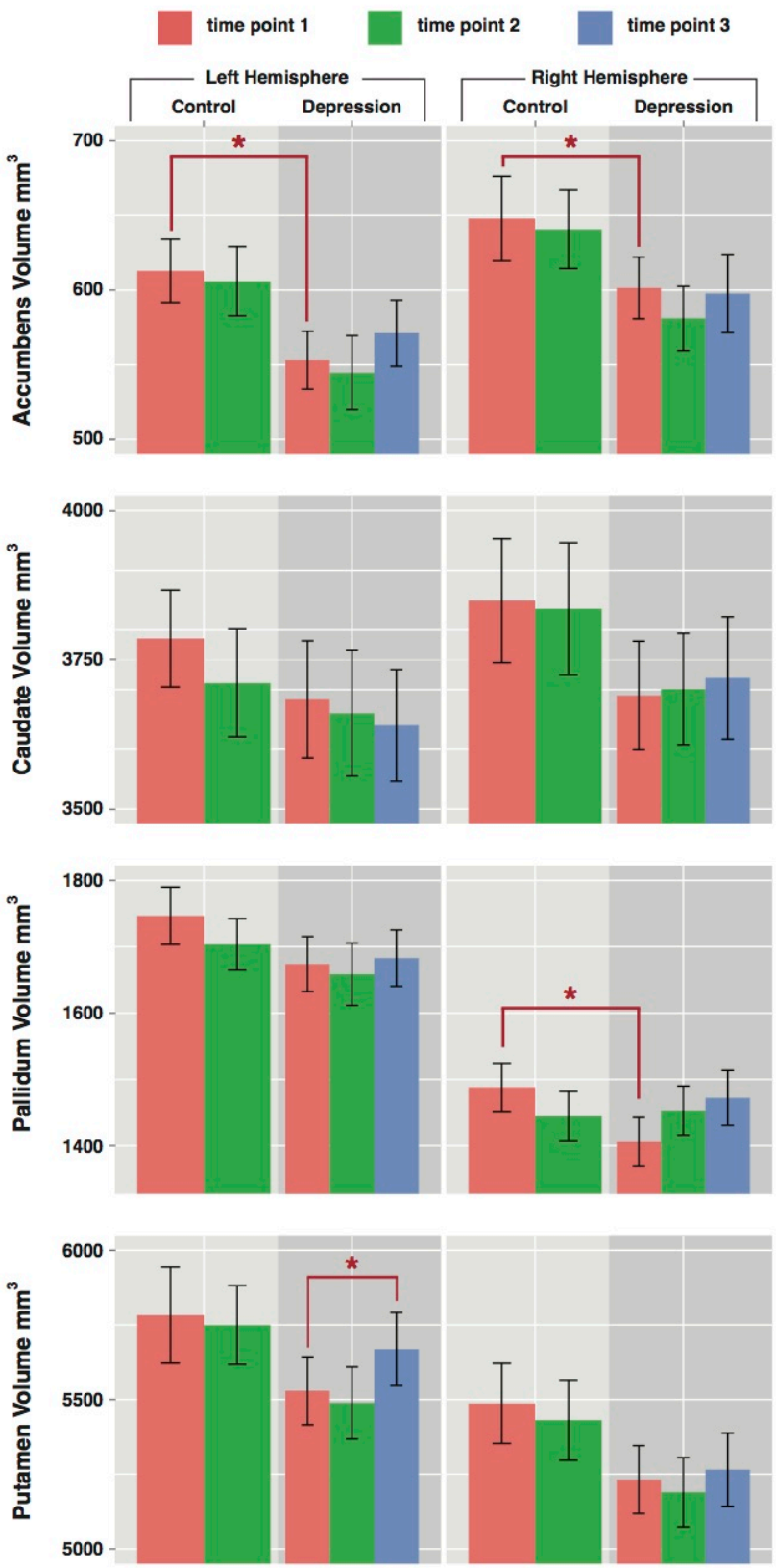

Figure 5-2. Average volume by group and time point for the accumbens, pallidum and putamen.

Error bars are +/- 1 standard error. Asterisks (*) indicate significant differences.

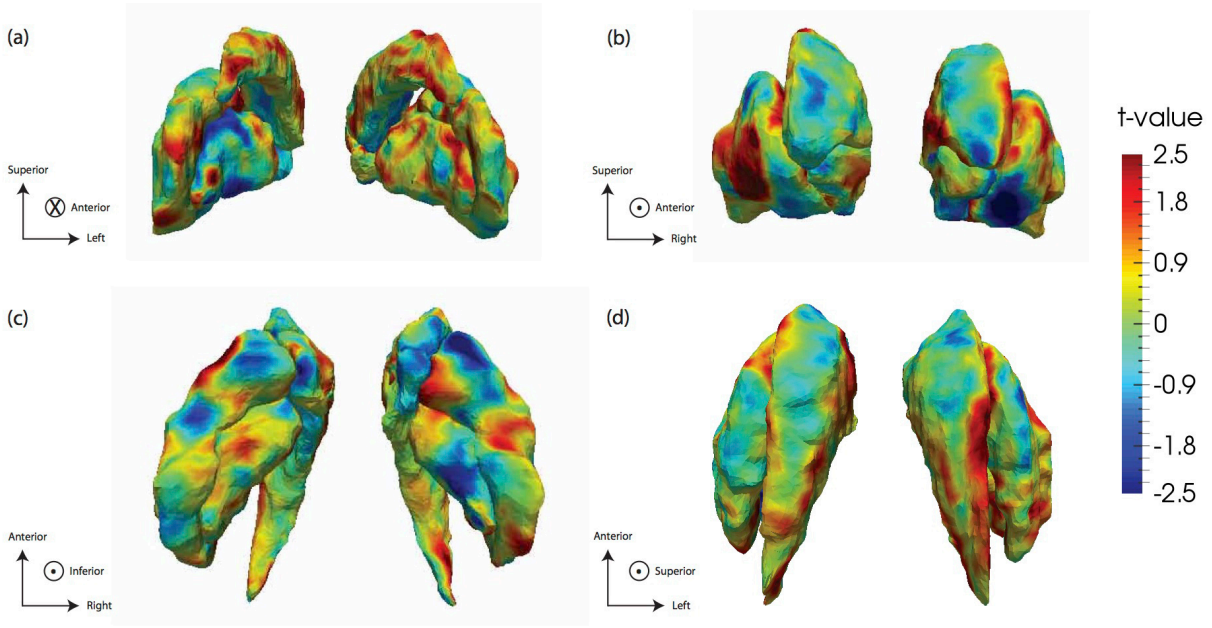

Figure 5-3. T-value maps of striatal and pallidal surfaces resulting from the mixed effects model examining the effect of ECT on thickness (radial distance - RD) over time. The perspectives are (a) superior, (b) inferior, (c) posterior, (d) anterior, (e) left lateral and (f) right lateral views. All maps are in radiological orientation (i.e., left-right flipped). Regions with warmer colors are expanding while those in cooler colors are contracting over time.

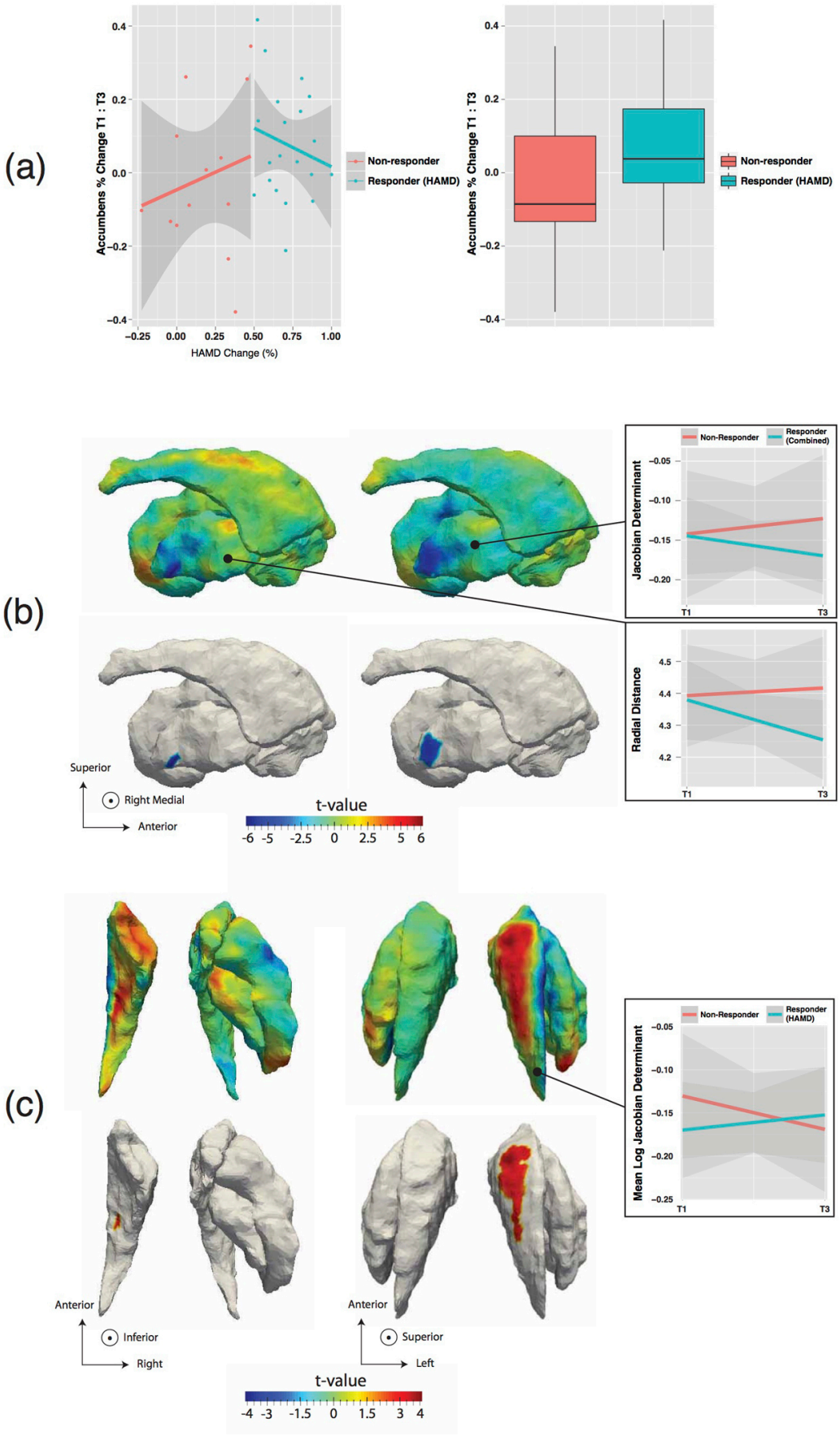
(a)
Accumbens % Change T1 : T3
HAMD Change (%)
Non-responder
Responder (HAMD)
(b)
Non-Responder
Responder (Combined)
Jacobian Determinant
Radial Distance
T1
T3
Superior
Right Medial
Anterior
t-value
-6 -5 -2.5 0 2.5 5 6
(c)
Non-Responder
Responder (HAMD)
Mean Log Jacobian Determinant
Anterior
Inferior
Right
Superior
Left
t-value
-4 -3 -1.5 0 1.5 3 4

Figure 5-4. (a) Percent change in nucleus accumbens volume between baseline and the end of the ECT index (T1 and T3) in patients defined as ECT responders and non-responders (b and c) Uncorrected (top) and FDR-thresholded (bottom) t-value maps of shape variation by response status for the pallidum. Negative t-values indicate smaller values in responders while positive t-values indicate larger values in responders. Panel b shows right hemisphere RD maps and panel c shows right hemisphere JD maps in responders compared to non-responders.

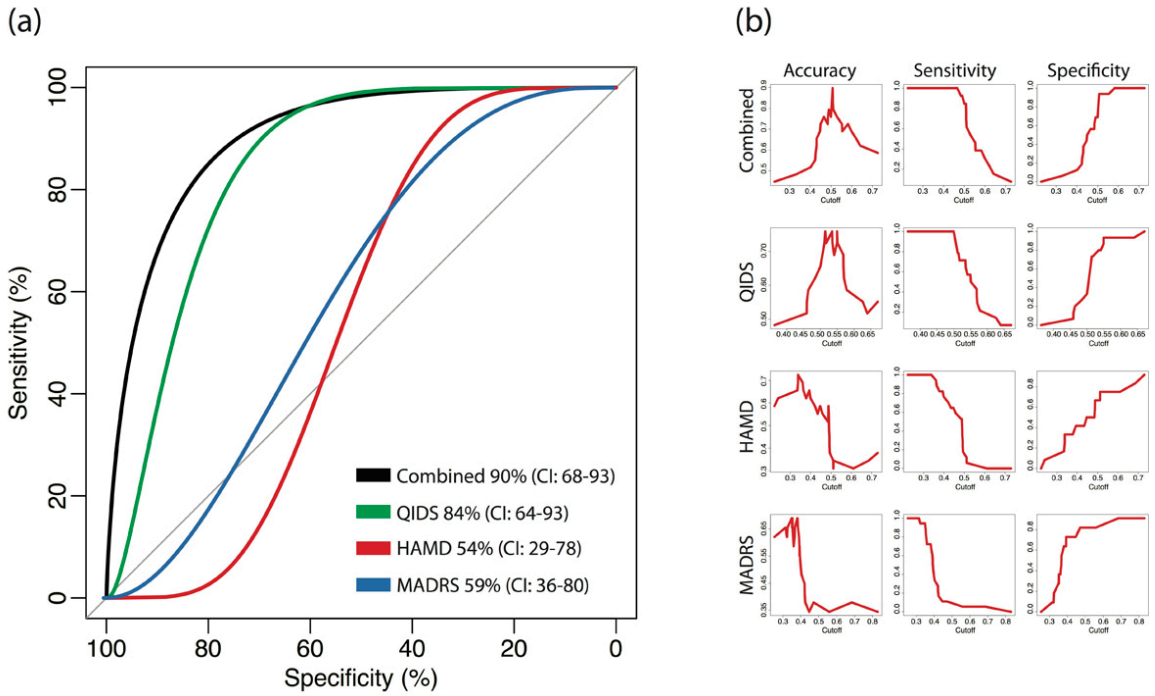

Figure 5-5. (a) Receiver operating characteristic curves resulting from support vector machines prediction of responsive patients from baseline shape and volume features. One curve is given for each mood scale (HAM-D, MARDS and QIDS) used to determine response status. 'All' refers to subjects who responded across all mood scales. (b) Plots of the accuracy, sensitivity and specificity values mapped separately for each model across a range of thresholds.

Chapter 6: Data-Driven Cluster Selection for Subcortical Shape and Cortical Thickness Predict Recovery from Depressive Symptoms[5]

Patients with major depressive disorder (MDD) who do not achieve full symptomatic recovery after antidepressant treatment have a higher risk of relapse. Compared to pharmacotherapies, electroconvulsive therapy (ECT) more rapidly produces a greater extent of response in patients with severe depression. However, prediction of which candidates are most likely to improve after ECT remains challenging.

Using structural MRI data from 42 ECT patients scanned prior to ECT treatment, we developed a random forest classifier based on data-driven shape cluster selection and cortical thickness features to predict remission. Right hemisphere hippocampal shape and right inferior temporal cortical thickness was most predictive of remission, with the predicted probability of recovery decreasing when these regions were thicker. Remission was predicted with an average of 78% accuracy. Classification of MRI data may help identify treatment-responsive patients and aid in clinical decision-making. Our results show promise for the development of personalized treatment strategies.

Introduction

About 16 million (6.9%) US adults suffer from at least one major depressive episode in a given year. Global 12-month prevalence rates are similar (~6 %), though vary regionally (Kessler and Bromet, 2013). Despite available therapies, only a minority (20-40%) of individuals will achieve full symptomatic remission after initial or successive treatment attempts (Kennedy and Paykel, 2004). Unfortunately, residual symptoms increase the risk of relapse (Keller, 2004),

[5] As of November 7th 2016, the content of this chapter is under review for publication and presentation at the 2017 annual International Symposium on Biomedical Imaging.

and with the recurrence of depressive episodes, symptoms become more refractory over time (Greden *et al*, 2011). The ability to predict the probability of therapeutic response would decrease the need for multiple lengthy medication trials, which appear needed in about 50% of patients (Gaynes *et al*, 2009), reduce suffering and enhance clinical outcomes. Several recent studies suggest that brain features extracted from structural neuroimaging data might relate to and predict symptom improvement (Phillips *et al*, 2015; Ten Doesschate *et al*, 2014). However, prognostic markers of post-treatment remission have not yet been identified.

Electroconvulsive therapy (ECT), an established treatment typically reserved for severe depression, works more quickly (response can occur in 2-4 weeks) and has higher remission rates than other standard therapeutic approaches (Husain *et al*, 2004). The fast acting and robust clinical effects of ECT make this treatment ideal for determining whether structural variations in the brain might predict individual recovery from depression after completing a series of treatments. The existing neuroimaging literature suggests brain abnormalities in prefrontal and temporal cortical association regions as well as subcortical hippocampal, amygdalar, thalamic, ventral striatal/pallidal, and brainstem centers are of high relevance to the pathophysiology of major depressive disorder (MDD) (Drevets *et al*, 2008). We and others have further shown that changes in these regions or networks occur with ECT (Joshi *et al*, 2016; Leaver *et al*, 2016a; Leaver *et al*, 2016b; Njau *et al*, 2016; Pirnia T, 2016; Wade *et al*, 2016). However, few prior studies have simultaneously investigated whether regional changes in volume, shape and/or gray matter thickness might predict recovery from symptoms. Using an unbiased data-driven approach applied to morphometric features extracted from regions across the brain, including those not expected to link with depression, this study thus set out to determine if variations in these features might serve as prognostic markers for future remission following ECT.

We additionally implement a novel data-driven approach to shape-based feature selection that defines clusters of shape features based on associations between shape and change in symptom severity over treatment. This approach has the benefit of preserving local information about a regions shape while simultaneously reducing the dimensionality of the feature set and the computational complexity. Similar patch-based approaches to shape analyses have been developed previously (Yushkevich *et al*, 2003), but to our knowledge this is the first time that a shape cluster selection approach was applied for prediction of remission in depression.

Materials and methods

Participants

42 patients from the University of California, Los Angeles (mean age, 41 years [SD 14 years]; range 19 - 74) all experiencing a DSM-IV defined major depressive episode and eligible to receive ECT were recruited as part of an ongoing study investigating treatment responsive biomarkers for antidepressant response in MDD. Patients were evaluated at two time points: 24 hours prior to ECT (T1) and within a week of completing ECT index (T2).

The Hamilton Depression Rating Scale (HAM-D-17) (Hamilton, 1960) was used to assess depression severity at each time point. Participants having a HAM-D-17 score of 8 or less at T2 were labeled remitters (Keller, 2003). 13 Patients remitted following ECT. The study protocol was approved by the Institutional Review Board at UCLA.

Image acquisition and segmentation

High-resolution motion-corrected multi-echo T1-weighted MPRAGE structural brain images (van der Kouwe *et al*, 2008) were acquired on a Siemens 3T Allegra system (Erlangen, Germany) for all subjects and time points (TEs/TR= 1.74, 3.6, 5.46, 7.32/2530 ms, TI=1260 ms, flip angle=7°, voxel resolution = 1.3×1×1 mm^3).

Previously validated FreeSurfer (Dale *et al*, 1999) workflows, which include removal of non-brain tissue, intensity normalization and automated volumetric parcellation based on probabilistic information from manually labeled training sets, were used for whole brain cortical (Desikan Killiany atlas-based parcellations) and subcortical segmentation. Each segmented image was visually inspected to ensure its quality.

Candidate features

Cortical thickness of 70 regions of interest (ROIs) and volumes of 14 subcortical ROIs were estimated from FreeSurfer segmentations. The local thickness (i.e. shape) values of the 14 subcortical structures, including the bilateral accumbens, amygdala, caudate, hippocampus, pallidum, putamen and thalamus, were further estimated using the Medial Demons framework described in (Gutman *et al*, 2012). In short, following non-linear warping to a spherical probabilistic template, local thickness of each subcortical surface was computed as the shortest distance from each vertex with respect to a skeletonized medial core traversing the anterior-posterior axis of the structure. This local thickness for each mesh was represented at each of the vertices whose number scaled roughly with the average volume. Depending on the ROI, the resolution of each mesh ranged from 900 to 2500 amounting to 27,120 vertices in total. Age was also included as a candidate feature due to its well-known association with brain morphometry and neural integrity.

Data driven subcortical shape cluster selection

To reduce the dimensionality of the feature set and preserve the ability to report on clinically informative subregions of a subcortical surface, we defined clusters of vertices and estimated the average cluster-level local thickness. Shape clusters of vertices were defined within the training set of each classification fold based on the two criteria: i) their individual, training

fold subject-wise correlation with the percent of change in HAM-D-17 score between the two scan times T1 and T2 ($\frac{HAMD\ T1-HAMD\ T2}{HAMD\ T1} = \Delta HAMD$) was above a threshold r_{thresh} and ii) the vertices with $|r| \geq r_{thresh}$ comprised a connected neighborhood cluster extent (CE) ≥ a threshold CE_{thresh} where $r_{thresh} \in \{0.025, 0.05, 0.1, 0.15, 0.2\}$ and $CE_{thresh} \in \{10,\ 20, 50, 100\}$. The effects of these parameterizations on classification performance were determined empirically via nested cross-validation described in section 2.6. The number and extent of shape clusters necessarily varied at each fold. Clusters identified in training folds were mapped to participants in testing folds and recomputed for cross-validation. Cortical thickness and subcortical volume measures were not subject to filtering as they contributed far less to feature set dimensionality.

Random forest classifier

Our classifier of choice was a random forest (RF) which is a supervised classifier built on an ensemble of classification and regression trees (CART) (Breiman, 2001) where each CART is composed of bootstrapped sample cases. Each decision node, v, within a CART is given a random subset of features for which the Gini impurity index is calculated as,

$$Gini(v) = \sum_{c=1}^{C} \hat{p}_c^v\ (1 - \hat{p}_c^v), \tag{1}$$

where $\hat{p}_c^v$ is the proportion of cases in class c at node v. CART nodes are split by the feature X_i maximizing the class purity of its child nodes, v^r and v^l by selecting the maximum $Gain\ (X_i, v)$ given by,

$$Gain\ (X_i, v) = \ Gini(X_i, v) - \omega_l Gini(X_i, v^l) - \omega_r Gini(X_i, v^r), \quad (2)$$

where ω_l and ω_r are the proportions of cases in node v assigned to child nodes v^r and v^l. The global importance I of feature X_i is taken as the summation of the decreases in the Gini coefficient at each node partitioned by X_i (Gray *et al*, 2013). Specifically,

$$I_{X_i} = \frac{1}{total\ tree\ number} \sum_{v \in S_{X_i}} Gain(X_i, v), \quad (3)$$

where S_{X_i} is the set of nodes split by X_i. RFs grow each CART to its full extent and determine the label of a new observation by majority vote of its constituent terminal nodes. Each RF was tuned using a grid search over the number of variables passed to each node from 2 to p, where p is the number of variables in the feature set. The constituent number of CARTs in each forest was 1000.

Nested cross-validation and feature selection

To further randomize subjects used for training and testing, we implemented a nested cross-validation approach, where the outermost loop performs error-averaging by repeating the experiment 5 times. At each iteration participants were randomly reassigned to one of 10 cross validation folds to stratify the training and disjoint hold-out datasets, while the inner most loop performs feature selection by further partitioning the subjects into 10 sub-folds and using them independently for feature selection. **Figure 6-1** illustrates the joint nested cross validation and feature selection process. The feature selection process used participants in 9 of the 10 sub-folds to define candidate shape clusters. Highly collinear features were removed if two features were correlated above a threshold ρ_{thresh} where $\rho_{thresh} \in \{0.5, 0.6, \ 0.7\ 0.8\ ,0.9, 0.95\}$. Of the two

highly correlated features, the one with the largest absolute correlation with all other features was removed from the feature set. Features surviving this initial threshold were then evaluated using 10-fold recursive feature elimination (RFE) (Guyon *et al*, 2002) where the internal classifier was also a RF composed of 1000 trees. The RFE algorithm proceeded by fitting a RF using all features and computing the importance (equation 3) of each feature in the full model. *P* feature subsets of sizes 1:*P* were created where *P* was the number of features surviving ρ_{thresh}. For all subsets, S_i, $i = 1{:}P$, the 1:*i*-th most important features were used to predict remission status with a RF. The feature set yielding the highest average accuracy across all 10 RFE folds was selected. RFE and all RF models were fit using the caret package in R (Kuhn, 2008).

As shown in Figure 6-1, the RFE process was repeated for all ten nested folds. Upon completion of the internal folds, we evaluated the frequency of a feature's occurrence in the optimal RFE subset and retained only those occurring with a frequency $f \geq f_{thresh}$ where $f_{thresh} \in \{0.2,\ 0.3, \ldots, 1\}$ is defined relatively as the *j*-th quantile of frequencies of an ROI's occurrence in the optimal feature set. f_{thresh} was necessarily defined at the vertex level for shape features. Vertices and individual ROIs surviving this thresholding process were subsequently used as features for prediction of the entire training set. Surviving vertices were re-clustered, and required to have CE $\geq CE_{thresh}$ (where CE_{thresh} is the same threshold used for initial cluster formation) and within cluster thickness averages were recomputed. Importantly, testing observations did not contribute to the feature selection process. Using a grid search we explored the space of all possible parameter combinations, r_{thresh}, CE_{thresh}, ρ_{thresh} and f_{thresh} resulting in a total of 1080 candidate parameterizations. Performances were averaged across all 5 repetitions of this process.

The prevalence of non-remitters was 69%; the baseline detection rate. Accuracy measures in binary classification problems with imbalanced samples are known to be biased towards the more prevalent class. To avoid inflated performance metrics we report on the balanced accuracy (BA) (Brodersen *et al*) defined as the average accuracy across both classes, formally BA = $\frac{1}{2}(\frac{True\ Positive}{Positive} + \frac{True\ Negative}{Negative})$. Our outermost loop allows us to further estimate the uncertainty of our performance estimates which is important given the increased likelihood of arriving at an accurate solution by chance in our large parameter space.

Results

Model performance

We selected the model parameterization yielding the highest average test BA across all 5 repeated folds. The highest BA was given by the parameters r_{thresh} = 0.025, CE_{thresh}, = 10 ρ_{thresh} = 0.95 and f_{thresh} = 1 resulting in a mean BA = 73% (range 64-79%), accuracy = 78% (range 61-83%), sensitivity = 85% (range 79-89%), specificity = 61% (range 46-69%), positive predictive value = 83% (range 77-86%), negative predictive value = 65% (range 54-75%) where non-remitters were the positive class.

Under this parameterization there were an average of 4 (SD = 2) features selected at each fold. The frequency of a feature's selection across cross validation folds is directly related to its overall importance by equation 3. Three features were selected in at over half (≥ 60%) of the models and therefore considered most important in predicting remission: two shape clusters of the right anterior hippocampus and the cortical thickness of the right inferior temporal cortex (ITC).

Associations between morphometry and clinical outcome

In order to understand the relationship between these regions and the predicted probability of a patient's remission, we fit a RF to 10 bootstrapped resamples of the patients using only these ROIs. **Figure 6-2**(a-b) illustrates this by plotting the predicted probability a hypothetical patient experiences symptom remission given an observed range of values in 20 even increments for each ROI while holding other ROIs at their respective observed means. A non-parametric LOESS model was fit to the resampled predicted probabilities. The predicted probability of remission declined sharply as the thickness of the right ITC and hippocampal clusters increased.

As a *post hoc* analysis we tested the correlation between the thickness of these regions and $\Delta HAMD$. Figure 6-2(c) plots the linear least squares fit of these associations. $\Delta HAMD$ was significantly anticorrelated with the first ($r = -0.43$, $p = 0.004$) and second (-0.38, $p = 0.01$) hippocampal clusters but not with ITC thickness (-0.27, $p = 0.08$). The significance of these associations survived correction for multiple comparisons using the standard 5% false discovery rate.

Additional shape clusters from several regions involved in reward circuitry and affected by MDD were selected with moderate frequencies including the bilateral amygdala (12%), left putamen (36%) and accumbens (22%). The frequency of each vertices' selection is shown in **Figure 6-3**. No other regions were selected in over 10% of the folds; age was never selected suggesting it was not a critical factor.

Discussion

A primary aim in prognostic pattern recognition is the stratification of patients into groups likely and unlikely to benefit from a course of treatment. Remission, which leads to a better long term prognosis (Keller, 2004), is the ultimate goal of treatment. Identifying which

individuals will make a full symptomatic recovery following ECT or any other antidepressant treatment will aid clinicians in determining optimal treatment strategies and help patients and their health care providers anticipate and manage future relapse risk. Using a large cohort of ECT patients from UCLA, we thus sought to identify prognostic biomarkers of remission from pre-treatment MRI scans.

Right hemisphere temporal lobe structures were most predictive of remission. These regions are biologically plausible since reduced hippocampal volume is widely implicated in the neuropathology of depression (Drevets *et al*, 2008; Schmaal *et al*, 2016) while the ITC is a center of integration for mood and emotional stimuli (Seminowicz *et al*). ECT has previously been demonstrated to induce neuroplastic changes in both structures (Joshi *et al*, 2016; Pirnia *et al*). We further probed our classifier to build a profile of regional characteristics indicative of remission. The predicted probability of remission was largely inversely associated with the thickness of these regions in our random forest classifier and subsequent tests of correlation confirmed that $\Delta HAMD$ was significantly anticorrelated with the baseline thickness of these regions.

This finding is consistent with several prior reports showing increased hippocampal volume with ECT (Abbott *et al*, 2014; Joshi *et al*, 2015) and our prior finding of a moderate relationship between smaller hippocampal volume at baseline and greater improvement in clinical response in an overlapping sample (Joshi *et al*, 2015). However, this is somewhat in opposition to a recent meta-analysis that reported reduced hippocampal volumes associated with lower remission likelihood to antidepressant drug therapies (Colle *et al*) though different mechanisms may occur for brain stimulation versus pharmacological interventions. It is also noteworthy that 83% of the ECT lead placements in our study were right unilateral (placed over

the right temporal area) which is ipsilateral to both the right ITC and right hippocampus. This may suggest that clinical outcome is partially determined by an interaction between the proximity of these structures to the induced current and their morphometry at the time of treatment. Future work will develop models that generalize across independent sites. Our current findings are encouraging and suggest that data-driven models based on neuroimaging may inform personalized treatment strategies.

Acknowledgements

Chapter 6 is a version of Wade BS, Sui J, Njau S, Leaver AM, Vasavada M, Gutman BA, Thompson PM, Espinoza R, Woods RP, Abbott CC, Narr KL, Joshi SH. (2017). Data-Driven Cluster Selection for Subcortical Shape and Cortical Thickness Predicts Recovery from Depressive Symptoms. IEEE Proceedings of International Symposium on Biomedical Imaging. In Review.

Jing Sui, Amber Leaver, Megah Vasavada, Randall Espinoza, Katherine Narr, Roger Woods and Christopher Abbott aided in data analysis and interpretation of findings. Stephanie Njau aided in data management. Boris Gutman developed the shape modeling methods used in this study. Shantanu Joshi and Paul Thompson were PIs of the study.

This study was supported by award number R01MH092301 from the National Institute of Mental Health supported this study.

References

Abbott CC, Jones T, Lemke NT, Gallegos P, McClintock SM, Mayer AR*, et al* (2014). Hippocampal structural and functional changes associated with electroconvulsive therapy response. *Transl Psychiatry* **4**: e483.

Breiman L (2001). Random Forests. *Machine Learning* **45**(1): 5-32.

Brodersen KH, Ong CS, Stephan KE, Buhmann JM The Balanced Accuracy and Its Posterior Distribution. *Proceedings of ICPR '10 Proceedings of the 2010 20th International Conference on Pattern Recognition*: 3121-3124.

Colle R, Dupong I, Colliot O, Deflesselle E, Hardy P, Falissard B*, et al* Smaller hippocampal volumes predict lower antidepressant response/remission rates in depressed patients: A meta-analysis. (1814-1412 (Electronic)).

Dale AM, Fischl B, Sereno MI (1999). Cortical surface-based analysis. I. Segmentation and surface reconstruction. *NeuroImage* **9**(2): 179-194.

Drevets WC, Price JL, Furey ML (2008). Brain structural and functional abnormalities in mood disorders: implications for neurocircuitry models of depression. *Brain structure & function* **213**(1-2): 93-118.

Gaynes BN, Warden D, Trivedi MH, Wisniewski SR, Fava M, Rush AJ (2009). What did STAR*D teach us? Results from a large-scale, practical, clinical trial for patients with depression. *Psychiatr Serv* **60**(11): 1439-1445.

Gray KR, Aljabar P, Heckemann RA, Hammers A, Rueckert D (2013). Random forest-based similarity measures for multi-modal classification of Alzheimer's disease. *NeuroImage* **65**(0): 167-175.

Greden JF, Riba MB, McInnis MG (2011). *Treatment resistant depression : a roadmap for effective care*, 1st edn. American Psychiatric Pub.: Washington, DC, xxv, 338 p.pp.

Gutman B, Wang Y, Rajagopalan P, Toga A, Thompson P (2012). Shape matching with medial curves and 1-D group-wise registration. *International Symposium on Biomedical Imaging* **9**: 716-719.

Guyon I, Weston J, Barnhill S, Vapnik V (2002). Gene Selection for Cancer Classification using Support Vector Machines. *Machine Learning* **46**(1): 389-422.

Hamilton M (1960). A rating scale for depression. *Journal of neurology, neurosurgery, and psychiatry* **23**: 56-62.

Husain MM, Rush AJ, Fink M, Knapp R, Petrides G, Rummans T*, et al* (2004). Speed of response and remission in major depressive disorder with acute electroconvulsive therapy

(ECT): a Consortium for Research in ECT (CORE) report. *The Journal of clinical psychiatry* **65**(4): 485-491.

Joshi SH, Espinoza RT, Pirnia T, Shi J, Wang Y, Ayers B*, et al* (2015). Structural Plasticity of the Hippocampus and Amygdala Induced by Electroconvulsive Therapy in Major Depression. *Biological psychiatry*.

Joshi SH, Espinoza RT, Pirnia T, Shi J, Wang Y, Ayers B*, et al* (2016). Structural Plasticity of the Hippocampus and Amygdala Induced by Electroconvulsive Therapy in Major Depression. *Biological psychiatry* **79**(4): 282-292.

Keller MB (2003). Past, present, and future directions for defining optimal treatment outcome in depression: remission and beyond. *Jama* **289**(23): 3152-3160.

Keller MB (2004). Remission versus response: the new gold standard of antidepressant care. *The Journal of clinical psychiatry* **65 Suppl 4**: 53-59.

Kennedy N, Paykel ES (2004). Residual symptoms at remission from depression: impact on long-term outcome. *Journal of affective disorders* **80**(2-3): 135-144.

Kessler RC, Bromet EJ (2013). The epidemiology of depression across cultures. *Annu Rev Public Health* **34**: 119-138.

Kuhn M (2008). Building Predictive Models in R Using the caret Package. *2008* **28**(5): 26.

Leaver AM, Espinoza R, Joshi SH, Vasavada M, Njau S, Woods RP*, et al* (2016a). Desynchronization and Plasticity of Striato-frontal Connectivity in Major Depressive Disorder. *Cereb Cortex*.

Leaver AM, Espinoza R, Pirnia T, Joshi SH, Woods RP, Narr KL (2016b). Modulation of intrinsic brain activity by electroconvulsive therapy in major depression. *Biological Psychiatry: Cognitive Neuroscience and Neuroimaging* **1**(1): 77-86.

Njau S, Joshi S, Leaver AM, Vasavada M, van Fleet J, Espinoza R*, et al* (2016). Variations in myo-inositol in fronto-limbic regions and clinical response to electroconvulsive therapy in major depression. *Journal of psychiatric research* **80**: 45-51.

Phillips ML, Chase HW, Sheline YI, Etkin A, Almeida JR, Deckersbach T*, et al* (2015). Identifying predictors, moderators, and mediators of antidepressant response in major depressive disorder: neuroimaging approaches. *Am J Psychiatry* **172**(2): 124-138.

Pirnia T, Joshi SH, Leaver AM, Vasavada M, Njau S, Woods RP*, et al* Electroconvulsive therapy and structural neuroplasticity in neocortical, limbic and paralimbic cortex. (2158-3188 (Electronic)).

Pirnia T JS, Khalil J, Leaver A, Woods RP, Espinoza R, Narr KL (2016). Electroconvulsive therapy and structural neuroplasticity in neocortical, limbic and paralimbic cortex. *Translational psychiatry* **6**(6): e832.

Schmaal L, Veltman DJ, van Erp TG, Samann PG, Frodl T, Jahanshad N*, et al* (2016). Subcortical brain alterations in major depressive disorder: findings from the ENIGMA Major Depressive Disorder working group. *Molecular psychiatry* **21**(6): 806-812.

Seminowicz DA, Mayberg Hs Fau - McIntosh AR, McIntosh Ar Fau - Goldapple K, Goldapple K Fau - Kennedy S, Kennedy S Fau - Segal Z, Segal Z Fau - Rafi-Tari S*, et al* Limbic-frontal circuitry in major depression: a path modeling metanalysis. (1053-8119 (Print)).

Ten Doesschate F, van Eijndhoven P, Tendolkar I, van Wingen GA, van Waarde JA (2014). Pre-treatment amygdala volume predicts electroconvulsive therapy response. *Frontiers in psychiatry* **5**: 169.

van der Kouwe AJ, Benner T, Salat DH, Fischl B (2008). Brain morphometry with multiecho MPRAGE. *NeuroImage* **40**(2): 559-569.

Wade BS, Joshi SH, Njau S, Leaver AM, Vasavada M, Woods RP*, et al* (2016). Effect of Electroconvulsive Therapy on Striatal Morphometry in Major Depressive Disorder. *Neuropsychopharmacology : official publication of the American College of Neuropsychopharmacology* **41**(10): 2481-2491.

Yushkevich P, Joshi S, Pizer SM, Csernansky JG, Wang LE (2003). Feature selection for shape-based classification of biological objects. *Information processing in medical imaging : proceedings of the conference* **18**: 114-125.

Figures

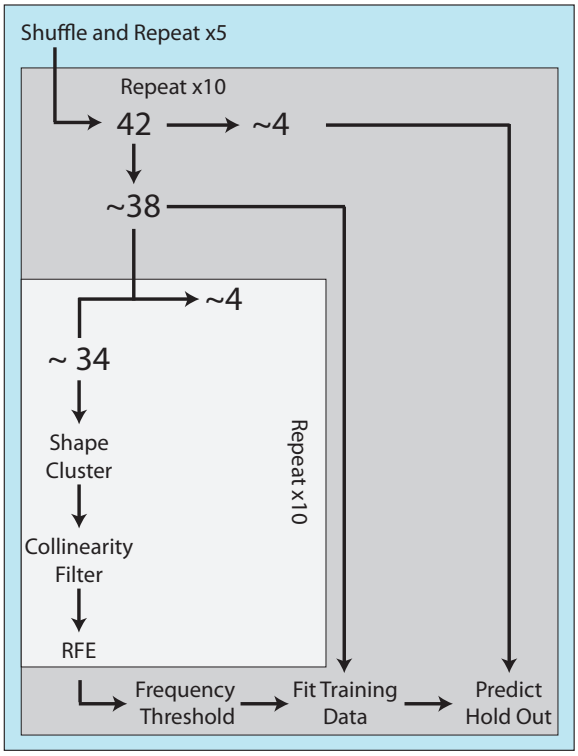

Figure. 6-1. Flowchart of classification process.

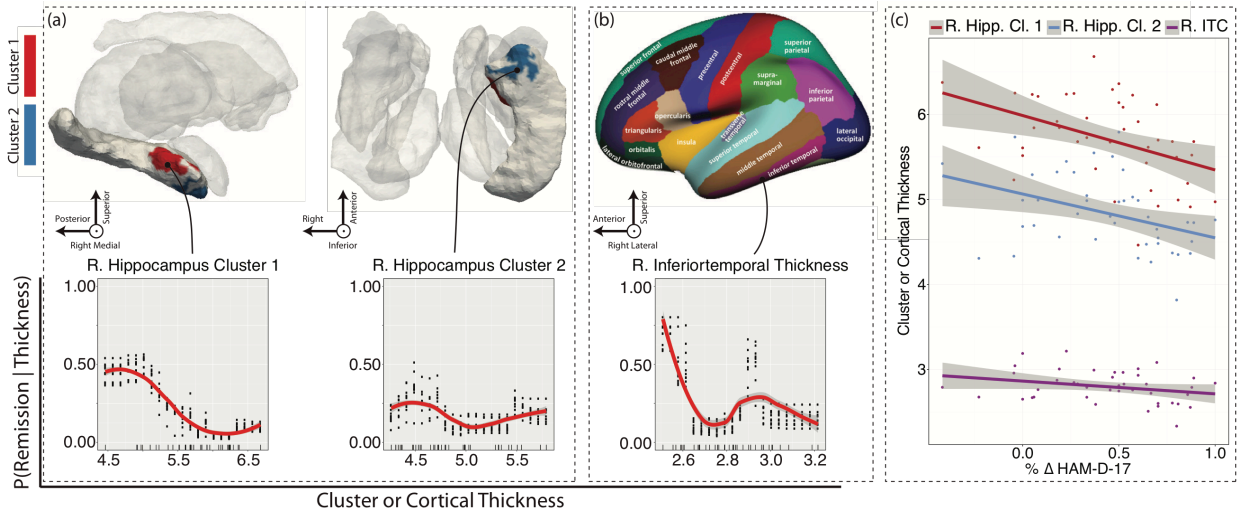

Figure. 6-2. Illustration of shape clusters (a) and cortical (b) ROIs (top) most important in the prediction of remission. Line plots (bottom) indicate the predicted probability of remission over an observed range (minimum to maximum in 20 even increments) of ROI thicknesses averaged across 10 bootstrapped resamples of the data set and refitted to the derived classifier. A non-parametric LOESS model was fit to the predicted responses. Points about each line indicate

predicted probabilities from each resample while rugs of each plot indicate the density of observed values in the whole sample. Note that orientation axes are provided below (a-b) as these are in radiological orientation (left-right flipped). (c) Plots least squares fits between the percent change in HAM-D-17 scores and baseline ROI thickness.

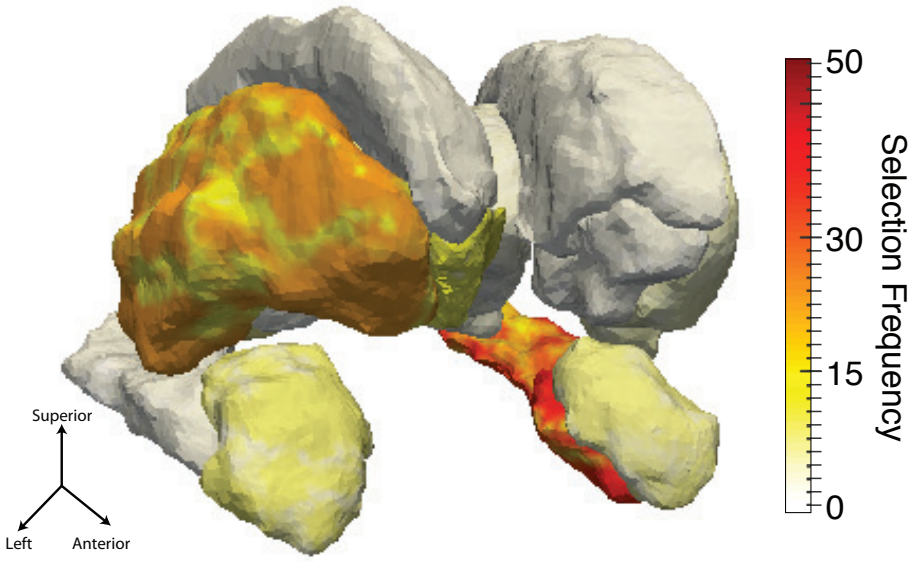

Figure. 6-3. Vertex selection frequency

Chapter 7: Ongoing work in the prediction of clinical relapse following electroconvulsive therapy

Introduction

Electroconvulsive therapy (ECT) elicits a high rate of clinical response, however, relapse rates following treatment also remain high despite ongoing maintenance therapy (Brakemeier *et al*, 2014; Kellner *et al*, 2006; Nordenskjold *et al*, 2013; Prudic *et al*, 2013; Sackeim *et al*, 2001). It is estimated that approximately 50-80% of patients with major depressive disorder (MDD) will suffer relapse after; 35% are expected to experience recurrent episodes and nearly 15% will suffer chronic, unremitting symptoms (Serra-Blasco *et al*, 2016).

There are currently no reliable neurobiological markers in clinical use for the identification of patients likely and unlikely to respond or maintain a durable response to antidepressant treatments of any form. As previously discussed, neurological mechanisms of ECT response remain poorly understood and mechanisms mediating or moderating response durability are even less understood. Prior research has even suggested that neural architecture responsible for acute response to ECT and long-term response durability may differ (Brakemeier *et al*, 2014).

Most investigations into the prediction of response durability (i.e. relapse) have focused on modeling associations between ultimate relapse and residual symptomatology (Judd *et al*, 1998) or number and severity of depressive episodes (Judd *et al*, 2000; Keller *et al*, 1992). Increased severity of these measures has been successfully associated with higher long-term relapse risk. Yet, few studies have investigated the viability of relapse prediction from neurobiological markers that could compliment the aforementioned clinical features a predictive framework.

A recent study by Serra-Blasco and colleagues implemented a naturalistic approach (Serra-Blasco *et al*, 2016) to predict relapse 5 years following treatment using structural MRI measures. Their group observed that right anterior cingulate gyrus volume was highly informative of subsequent relapse and accounted for an additional 20% of variability in depression rating scales above the use of clinical markers in isolation. Earlier studies by Frodl identified smaller hippocampal and anterior cingulate volumes as indicative of subsequent relapse (Frodl *et al*, 2008a; Frodl *et al*, 2008b). Hippocampal and anterior cingulate atrophy are among the most consistently reported neurological manifestations of MDD, lending credence to these findings. The studies by Frodl and Serra-Blasco were naturalistic in design, however, and did not restrict their investigations to patients receiving particular courses of treatment. Additionally, their findings are based on analysis of variance methods and did not implement cross-validation based methods to evaluate the prognostic values of these brain regions in relapse risk stratification.

Here, we build on our prior work presented in chapters 5 and 6 and seek to identify biomarkers to aid in risk stratification of long-term relapse. We use the predictive framework previously developed in chapter 6, however, currently without the use of subcortical shape descriptors (though these will be applied in the future). Using two independent patient cohorts from UCLA the University of New Mexico (UNM) we investigate the predictive value of MRI-based biomarkers based on pre-treatment and post-treatment measures as well as changes in brain structure between these two time points. We currently restrict our investigations to within-site predictions, however, due to wide age disparities between the two cohorts. Our preliminary findings are highly encouraging but will require independent replication as they are based on small sample sizes. The ability to identify patients likely to relapse following treatment would be

a crucial step towards developing more personalized management strategies and offsetting many of the personal and economic costs associated with the characteristic episodic recurrence of MDD.

Methods

Participants and image processing

A subset of the UCLA patient cohort reported on in the previous chapter and additional patients from UNM were followed 6-months after completing full ECT index. 17 patients from UCLA (mean age, 45 years [SD 12 years]; range 19 - 64) and 25 patients from the University of New Mexico (mean age, 65 years [SD 8 years]; range 25 - 94) were scanned 24 hours prior to initiation of ECT index and within a week of completing index. Of the UCLA cohort, 6 patients relapsed and 13 patients relapsed at UNM. It is important to acknowledge that much debate surrounds the topic of defining relapse and, naturally, much information and nuance is lost in designating arbitrary cutoffs based on numerical changes in depression rating scales. However, for our purposes a standard definition of relapse was used in which two criteria needed to be met: i) patients must have initially responded to ECT with a reduction in HAM-D-17 scores being $\geq$ 50% and ii) patients experience a return of $\geq$ 50% of symptoms following ECT index.

Imaging parameters and segmentation procedures were the same as those reported previously in chapter 6. Unlike our report in the previous chapter, subcortical shape analyses have yet been applied to the prediction of relapse; however, this is intended for future development of this project. Here, we instead only use FreeSurfer-derived subcortical volume and cortical thickness measures as the input features for our classifier.

Nested cross validation and parameterization

In an approach similar to that described in chapter 6, we randomized subjects used for training and testing by implementing a nested cross-validation approach, where the outermost loop performs error-averaging by repeated the experiment 10 times while shuffling subjects in each of the inner folds at each iteration. The next inner loop performs repeated 5-fold cross validation to randomly stratify the training and the disjoint hold-out datasets, while the inner most loop performs feature selection by further partitioning the subjects into 5 sub-folds and using them independently for feature selection.

An additional grid search over the parameters, ρ_{thresh} and f_{thresh}, was performed. Highly collinear features were removed if two features were correlated above a threshold ρ_{thresh} where $\rho_{thresh} \in \{0.1, 0.2, \ldots, 0.9\}$. The feature with the largest absolute correlation with all other features was removed from the candidate feature set. Features surviving this initial threshold were then evaluated using the RFE algorithm described previously (and detailed by Guyon (Guyon *et al*, 2002)) where the internal classifier was also a RF composed of 500 trees. Upon completion of the internal folds, we evaluated the frequency of a feature's occurrence in the optimal RFE subset and retained only those occurring with a frequency $f \geq f_{thresh}$ where $f_{thresh} \in \{0.1,\ 0.3, \ldots, 1\}$ is defined relatively as the *j*-th quantile of frequencies of an ROI's occurrence in the optimal feature set. Because binary classification problems are well-known to be biased towards the more prevalent class, we again used the balanced accuracy (BA) (Brodersen *et al*) defined as $\text{BA} = \frac{1}{2}\left(\frac{True\ Positive}{Positive} + \frac{True\ Negative}{Negative}\right)$ to evaluate model performance in order to mitigate performance inflation due to class imbalance.

This approach to repeated nested cross-validation was performed independently for features from baseline (pre-treatment, T1), follow-up (post-index, T2) and changes between time points (deltas). Deltas were defined simply as $\Delta X_i = T2X_i - T1X_i$, where X_i is the i-th feature

in the dataset. A $\Delta X_i > 0$ indicates that the given brain region's thickness or volume has increased over treatment index. Due to the substantial age differences across the two sites we only report here on classification of relapse within site.

Results

For the sake of brevity we only detail the highest performing models that attained an average BA $\geq$ 70% across the 10 repetitions of cross validation. Models not meeting this criterion are only presented summarily. Relapse at UCLA was most accurately predicted from morphological changes in brain structure over the course of index (deltas); post-treatment brain structure was nearly as predictive. At UNM, post-treatment (T2) brain structure was most predictive of later relapse and pre-treatment measures (T1) were nearly as predictive.

Balanced accuracy, positive predictive value (the probability that a patient classified as positive is truly positive) and negative predictive value (the probability that a patient classified as negative is truly negative) by site and time point are outlined in table 7-1.

Prediction of relapse from pre-treatment measures

Relapse of UNM patients from T1 measures was predicted with an average balanced accuracy of 71% (range, 63-84%), accuracy = 70% (range, 64-84%), sensitivity = 76% (range, 58-91%), specificity = 65% (range, 53-76%), positive predictive value = 67% (range, 60-78%) and negative predictive value = 75% (range, 64-90%). The most informative regions (as determined by being selected in the RFE process in $\geq$ 80% of repeated folds) were: the right thalamus and left accumbens volumes and the left temporal pole and right rostral anterior cingulate cortical thicknesses. Here, the left temporal pole thickness was largely inversely associated with predicted probability of relapse. Larger right thalamus volume tended to increase predicted relapse probability while increases in left accumbens volume and right rostral anterior

cingulate thickness resulted in generally lower predicted relapse probabilities when other regions were held at their observed means. The relationships between these regions' morphometry and predicted relapse probabilities are illustrated in **Figure 7-1**. The parameters of this model were $\rho_{thresh} = 0.3$ and $f_{thresh} = 0.1$. Relapse within UCLA was predicted at near-chance levels from T1 measures with an average balanced accuracy of 56%.

Prediction of relapse from post-treatment measures

For the classification of UCLA data, the highest performing parameterization at T2 was $\rho_{thresh} = 0.9$ and $f_{thresh} = 0.4$ which yielded an average balanced accuracy = 73% (range, 66 – 75%), accuracy = 81% (range, 76-82%), sensitivity = 100% (range, 100-100%), specificity = 46% (range, 33-50%) positive predictive value = 77% (range, 73-78%) and negative predictive value = 100% (range, 100-100%). Here, four regions were most informative the right precentral gyrus, right fusiform gyrus, left caudal anterior cingulate and left medial orbital frontal cortex. For each of these regions, the predicted probability of relapse increased in subjects having thicker cortices (these relationships are illustrated in **Figure 7-2**). The predicted probability of relapse was higher among patients having thinner right paracentral gyri, however, the rugs in figure 7-2 indicate that this is likely driven by the presence of a single observation.

In the classification of the UNM cohort from T2 measures, the parameters $\rho_{thresh} = 0.7$ and $f_{thresh} = 0.9$ provided the highest performance with an average balanced accuracy = 77% (range, 67 – 84%), accuracy = 77% (range, 68-84%), sensitivity = 74% (range, 66-91%), specificity = 80% (range, 69-92%) positive predictive value = 77% (range, 66-88%) and negative predictive value = 77% (range, 69-90%). Five cortical regions (illustrated in **Figure 7-3**) were considered most important in this model: the right frontal pole, right pars triangularis, the bilateral pericalcarine and right entorhinal cortices. Intriguingly, the relationship between

predicted probabilities of relapse given observed ranges of cortical thicknesses tended to be opposite to that observed at UCLA, with these regions being indicative of lower probabilities of relapse at thicker values. This difference is likely due to the fact that UCLA and UNM predictions were driven by disjoint sets of cortical regions.

Prediction of relapse from morphological changes over treatment index

Relapse was best predicted within UCLA from a model based on change scores with the parameterization $\rho_{thresh} = 0.8$ and $f_{thresh} = 1$ yielded an average balanced accuracy = 74% (range, 61 –82%), accuracy = 75% (range, 64-82%), sensitivity = 80% (range, 72-81%), specificity = 68% (range, 50-83%) positive predictive value = 82% (range, 72-90%) and negative predictive value = 64% (range, 50-71%). Interestingly, this model was constructed exclusively on the degree of change in left accumbens volume over index. As shown in **Figure 7-4**, patients with more increased left accumbens volumes over index were predicted to be more likely to relapse, in general. Prediction of relapse from changes over index within the UNM cohort attained a low BA of 61%.

Sensitivity analyses

To examine the probability that the classifier parameterizations resulting in the largest BA were arrived at by random chance of specific combinations of subjects or due to the presence of high-leverage subjects, we conducted a sensitivity analysis. This was approached by repeating the classification process for the models detailed previously at their respective optimal parameterizations 100 times. At each iteration 2.5% of the observations were randomly excluded. In **Figure 7-5** we compare the observed BAs reported above to the resampled distributions to both determine whether the observed performance is an outlier in this resampled distribution and, secondly, to examine whether the spread of the resampled distributions is

particularly wide which would also suggest highly variable performances potentially driven by particular subjects.

We note that the UNM T1, UNM T2 and UCLA Δ models all fall in high-density regions of the resampled BAs suggesting they are fairly estimated. The observed UCLA T2 model BA falls beneath the high-density region of the resampled distribution suggesting a conservative estimation. The percentiles of the observed BAs relative to their respective resampled distributions are as follows: UNM T1 = 77^{th} percentile, UNM T2 = 42^{nd} percentile, UCLA T2 = 18^{th} percentile and UCLA Δ = 74^{th} percentile. Notably, the high-density regions of the resampled distributions were well above 50%, however, it is also notable that the UCLA Δ distribution was spread widely with a number of observations being below 50% suggesting a high variance (i.e. potentially unreliable) model.

Discussion

In this ongoing work we have taken steps towards identifying biomarkers for the identification of patients who are at high risk for symptom relapse following reception of ECT. We have so far only developed site-specific classifiers. A major challenge in the future of this work will be to develop classifiers capable of predicting relapse across site. This has so far been very challenging as these two cohorts vary substantially in terms of age as well as degree of response to ECT. Natural age-related neurodegeneration is a substantial confound in the identification of MDD-related patterns of neurodegeneration that might inform subsequent relapse. Additional confounds include minor differences in ECT administration by site as well as the use of different scanners to image each patient cohort.

Future work will attempt to implement strategies such as instance weighting and domain adaptation to incorporate known differences in demographic and feature set distributions by site

into the classification model (Wachinger and Reuter, 2016). An additional consideration of these models' respective values will be the accuracy they provide as weighted by whether they are based on pre- or post-treatment where the former would clearly be considered the most valuable in a clinical setting. For instance, the highest performing UNM model was based on post-treatment observations and yielded a balanced accuracy of 77%. But, is this more or less valuable than the model built from pre-treatment measures that had an accuracy of 71%? Though the latter model is slightly less accurate it would have the added benefit of mitigating unnecessary side effects in patients identified as likely to relapse. Considerations such as this will be factored in to future directions of this work.

Our initial results in the classification of subsequent relapse within site are encouraging with both sites attaining over 70% accuracy when using features from post-treatment. The highest performing model from UNM was derived from this follow-up time point while the most predictive model at UCLA was derived from changes in brain structure over index. Ideally, we hope to develop a model capable of predicting relapse from pre-treatment measures of brain morphometry as this would help to rule out candidates who are unlikely to benefit in the long term. Of course, ECT is often an important line of treatment for its acute benefits as well as is the case for recipients who are imminently suicidal. Yet, a forecast of ECTs long-term benefits will be valuable to both the clinician and the patient in the medical decision making process.

References

Brakemeier EL, Merkl A, Wilbertz G, Quante A, Regen F, Buhrsch N*, et al* (2014). Cognitive-behavioral therapy as continuation treatment to sustain response after electroconvulsive therapy in depression: a randomized controlled trial. *Biological psychiatry* **76**(3): 194-202.

Brodersen KH, Ong CS, Stephan KE, Buhmann JM The Balanced Accuracy and Its Posterior Distribution. *Proceedings of ICPR '10 Proceedings of the 2010 20th International Conference on Pattern Recognition*: 3121-3124.

Frodl T, Jager M, Born C, Ritter S, Kraft E, Zetzsche T*, et al* (2008a). Anterior cingulate cortex does not differ between patients with major depression and healthy controls, but relatively large anterior cingulate cortex predicts a good clinical course. *Psychiatry research* **163**(1): 76-83.

Frodl T, Jager M, Smajstrlova I, Born C, Bottlender R, Palladino T*, et al* (2008b). Effect of hippocampal and amygdala volumes on clinical outcomes in major depression: a 3-year prospective magnetic resonance imaging study. *Journal of psychiatry & neuroscience : JPN* **33**(5): 423-430.

Guyon I, Weston J, Barnhill S, Vapnik V (2002). Gene Selection for Cancer Classification using Support Vector Machines. *Machine Learning* **46**(1): 389-422.

Judd LL, Akiskal HS, Maser JD, Zeller PJ, Endicott J, Coryell W*, et al* (1998). Major depressive disorder: a prospective study of residual subthreshold depressive symptoms as predictor of rapid relapse. *Journal of affective disorders* **50**(2-3): 97-108.

Judd LL, Paulus MJ, Schettler PJ, Akiskal HS, Endicott J, Leon AC*, et al* (2000). Does incomplete recovery from first lifetime major depressive episode herald a chronic course of illness? *Am J Psychiatry* **157**(9): 1501-1504.

Keller MB, Lavori PW, Mueller TI, Endicott J, Coryell W, Hirschfeld RM*, et al* (1992). Time to recovery, chronicity, and levels of psychopathology in major depression. A 5-year prospective follow-up of 431 subjects. *Archives of general psychiatry* **49**(10): 809-816.

Kellner CH, Knapp RG, Petrides G, Rummans TA, Husain MM, Rasmussen K*, et al* (2006). Continuation electroconvulsive therapy vs pharmacotherapy for relapse prevention in major depression: a multisite study from the Consortium for Research in Electroconvulsive Therapy (CORE). *Arch Gen Psychiatry* **63**(12): 1337-1344.

Nordenskjold A, von Knorring L, Ljung T, Carlborg A, Brus O, Engstrom I (2013). Continuation electroconvulsive therapy with pharmacotherapy versus pharmacotherapy alone for prevention of relapse of depression: a randomized controlled trial. *J ECT* **29**(2): 86-92.

Prudic J, Haskett RF, McCall WV, Isenberg K, Cooper T, Rosenquist PB*, et al* (2013). Pharmacological strategies in the prevention of relapse after electroconvulsive therapy. *J ECT* **29**(1): 3-12.

Sackeim HA, Haskett RF, Mulsant BH, Thase ME, Mann JJ, Pettinati HM*, et al* (2001). Continuation pharmacotherapy in the prevention of relapse following electroconvulsive therapy: a randomized controlled trial. *Jama* **285**(10): 1299-1307.

Serra-Blasco M, de Diego-Adelino J, Vives-Gilabert Y, Trujols J, Puigdemont D, Carceller-Sindreu M*, et al* (2016). NATURALISTIC COURSE OF MAJOR DEPRESSIVE DISORDER PREDICTED BY CLINICAL AND STRUCTURAL NEUROIMAGING DATA: A 5-YEAR FOLLOW-UP. *Depression and anxiety*.

Wachinger C, Reuter M (2016). Domain adaptation for Alzheimer's disease diagnostics. *NeuroImage* **139**: 470-479.

Tables

Table 7-1. Classifier performance by site by time point

	UCLA			UNM		
	T1	T2	Delta	T1	T2	Delta
BA	56%	73%	74%	71%	77%	61%
PPV	68%	77%	82%	67%	77%	61%
NPV	46%	100%	64%	75%	77%	62%

Abbreviations: BA = balanced accuracy; PPV = positive predictive value; NPV = negative predictive value

Figures

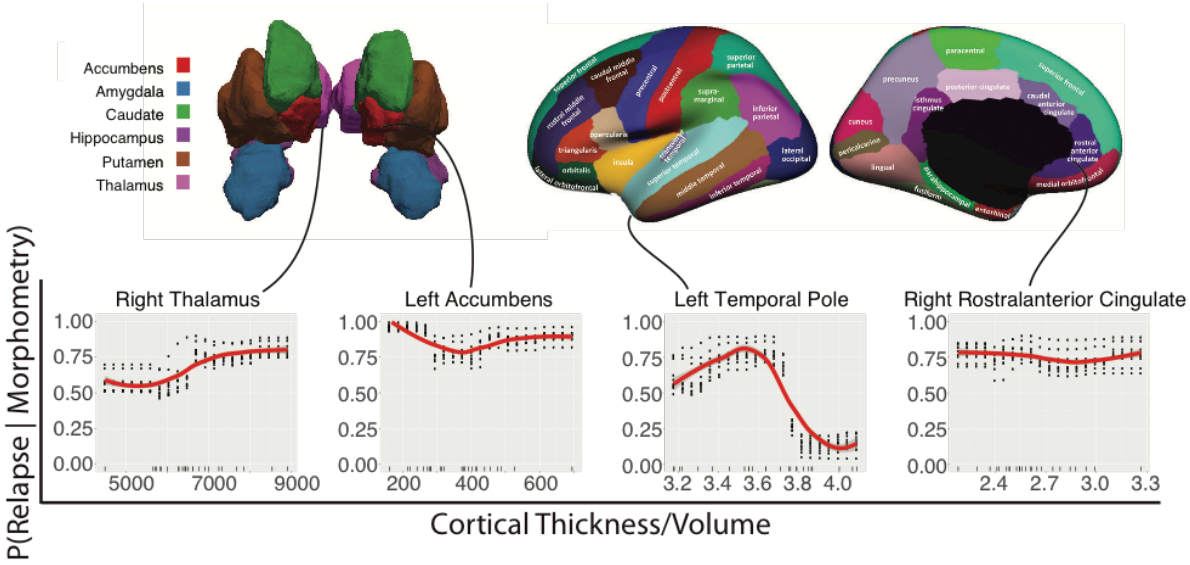

Figure 7-1. Cortical and subcortical regions (top) contributing most to the prediction of relapse at UNM prior to ECT index and the predicted probabilities of relapse given a range of observed cortical thicknesses (bottom). Predicted probabilities for each range are obtained by holding other regions at their observed means. Points about each line indicate predicted probabilities from each of 10 bootstrapped resamples taken at 20 evenly spaced increments from the minimum to maximum of the observed ranges of cortical thickness or subcortical volume values. Rugs of each plot indicate the density of observed values in the whole sample.

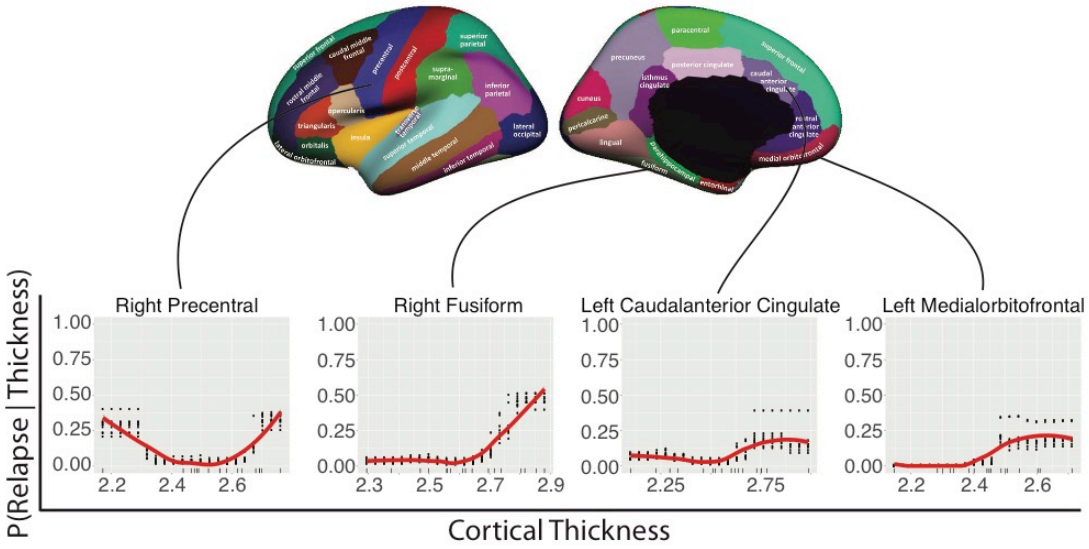

Figure 7-2. Cortical regions (top) contributing most to the prediction of relapse at UCLA following ECT index and the predicted probability of relapse given a range of observed cortical thicknesses (bottom). Points about each line indicate predicted probabilities from each of 10 bootstrapped resamples taken at 20 evenly spaced increments from the minimum to maximum of the observed ranges of cortical thickness values. Rugs of each plot indicate the density of observed values in the whole sample.

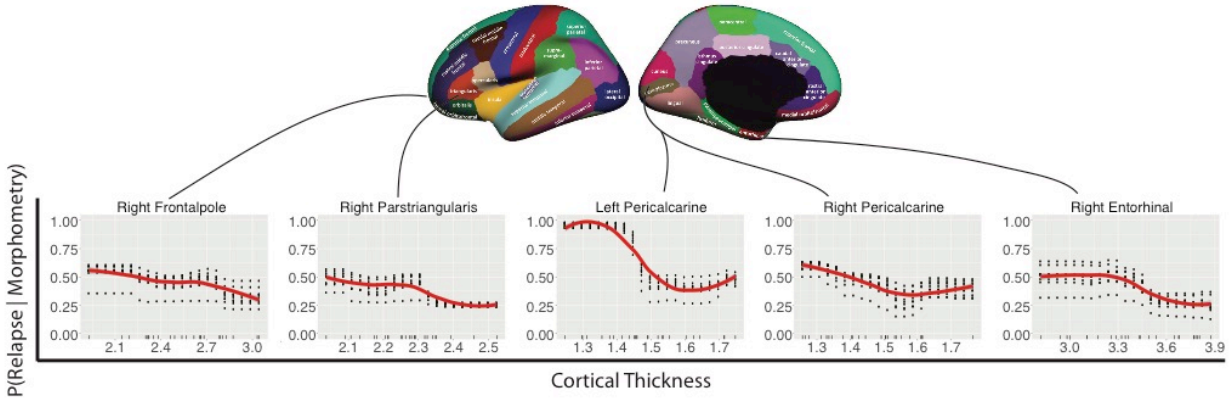

Figure 7-3. Cortical regions (top) contributing most to the prediction of relapse at UNM following ECT index and the predicted probability of relapse given a range of observed cortical thicknesses (bottom). Points about each line indicate predicted probabilities from each of 10 bootstrapped resamples taken at 20 evenly spaced increments from the minimum to maximum of the observed ranges of cortical thickness values. Rugs of each plot indicate the density of observed values in the whole sample.

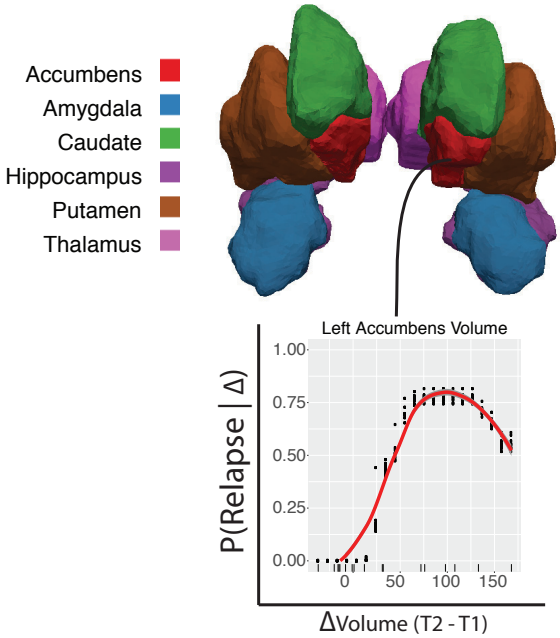

Figure 7-4. Illustration of the left accumbens (top) that contributed most to the prediction of relapse at UCLA when evaluating structural changes between T1 and T2. Again, the predicted probability of relapse for an observed range of changes in left accumbens volume (taken in 20 even increments) is shown below. Rugs indicate densities of observed change scores.

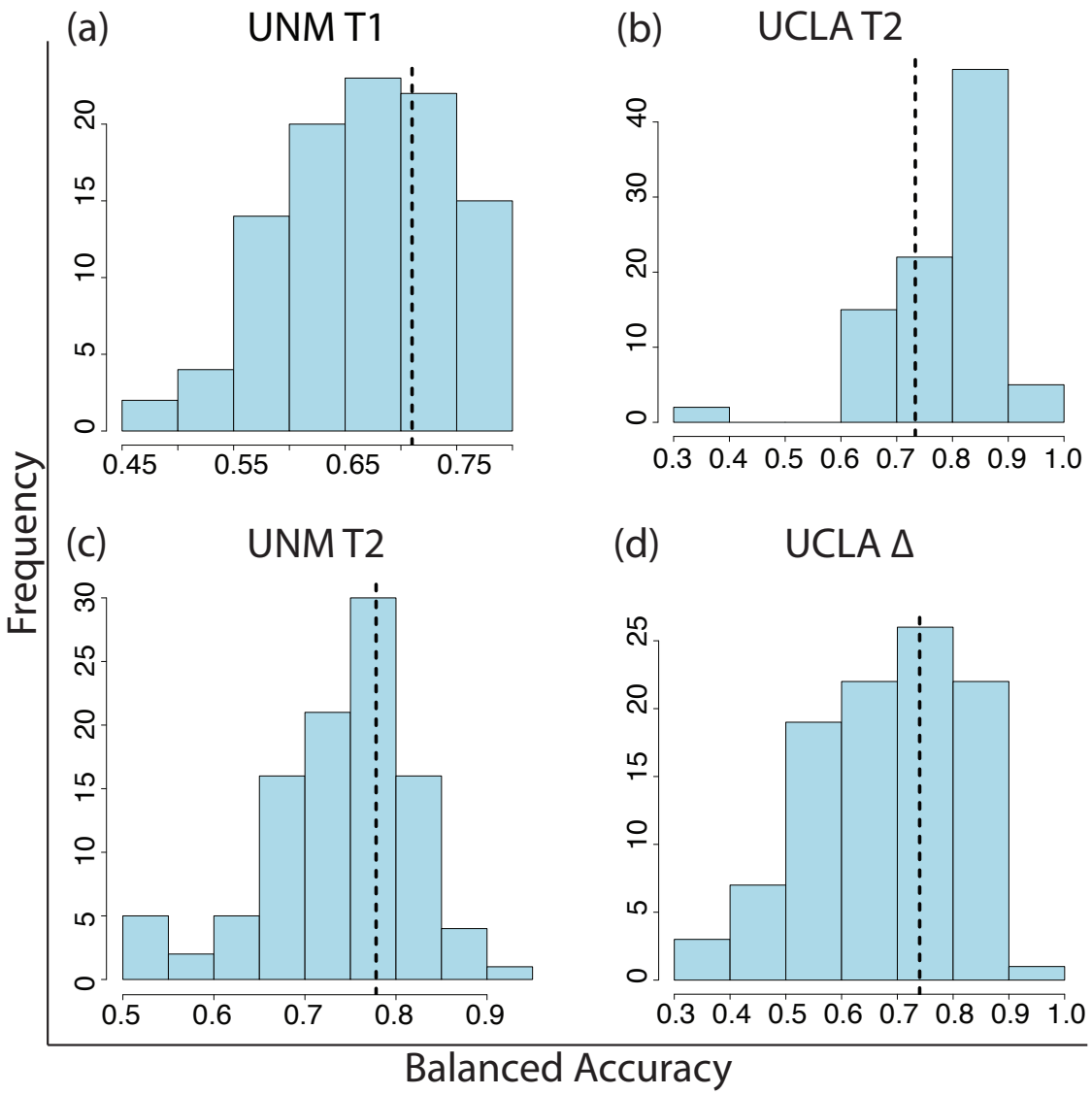

Figure 7-5. Observed balanced accuracies of high-performance models (vertical dashed lines) versus resampled distributions of balanced accuracies from (a) pretreatment measures of morphometry at UNM, (b) follow-up measures of morphometry from UCLA, (c) follow-up measures of morphometry from UNM and (d) changes in morphometry over index from UCLA.

Chapter 8: Conclusions

In this body of work we demonstrated the efficacy of high dimensional, locally defined shape data as a basis for biomarker discovery in two domains: the description of neurological manifestations of HIV infection and the identification of patients with severe major depressive disorder (MDD) who are likely to respond to an aggressive line of antidepressant treatment, electroconvulsive therapy (ECT). Descriptions of shape modeled local surface-based variations in the thickness (radial distance) and surface area dilation ratio (Jacobian determinant) of seven prominent subcortical structures: the accumbens, amygdala, caudate, hippocampus, pallidum, putamen and the thalamus. Broadly speaking, we found that information captured by these shape descriptors exceeded that captured by global measures of volume for the same structures. This is likely due to the subtle presentations of neurodegeneration exhibited by certain stages of disorders; these more subtle signals would not be discernable when averaged across an entire brain region, as is the case with volumetric measures. But, in exchange for more sensitive, local descriptors, we are confronted with a higher chance of detecting false positives and, in classification problems, the curse of dimensionality.

Chapter 2 explored the treatment of these shape descriptors as predictive features in the context of classifying Alzheimer's disease and its prodromal state, mild cognitive impairment. There we compared the use of feature selection methods and no feature selection to determine whether commonly used classification algorithms were prone to overfit to training data using these descriptors. We observed that the LASSO significantly improved the computational efficiency of classifiers using these descriptors but yielded relatively unstable performances across classification problems based on increasingly smaller sample sizes. We posited that this is due to the high degree of sparsity induced by the LASSO approach since more greedy, retentive

methods such as regularized random forests and no feature selection were more stable. These results suggest an expected tradeoff between computational efficiency and classification performance. On average, the greedier regularized random forest approach retained more features than the LASSO to classify mild cognitive impairment. As mild cognitive impairment has a more subtle and heterogeneous presentation than more advanced Alzheimer's disease, this implies that overly sparse feature selection requirements may fail to capture more spatially diffuse patterns of neurodegeneration.

In chapters 3-4 we investigated the effects of HIV infection on the aging brain at both geriatric (Chapter 3) and pediatric (Chapter 4) ends of the age spectrum. These studies were largely descriptive rather than predictive in scope. Among the elderly cohort, we observed significant local atrophy and global volumetric reductions in several subcortical structures in those who were HIV+. These findings are aligned with previous reports of more severe neurodegeneration in elderly HIV+ patients versus age-matched, uninfected controls (Canizares *et al*, 2014; Cohen *et al*, 2015).

Chapter 4 addressed how HIV infection affects the developing adolescent brain in a large cohort of perinatally infected Thai children. Unlike the elderly cohort, the pediatric study examined cross-sectional and longitudinal associations. While existing literature on pediatric HIV infection is far sparser than that on adults, our findings largely corroborated patterns of neurodegeneration observed in adults, highlighting again the basal ganglia's vulnerability to infection. Volumetric analyses did not reveal significant differences in this cohort and all reported findings were based on local shape characteristics. Cross-sectional observations revealed a significant reduction in the thickness of the right medial pallidum, the surface area of the left lateral pallidum and a region of the right amygdala in HIV+ children. The surface area of

the right amygdala was also enlarged in HIV+ children. Infection-by-treatment variation was observed as well with the thickness and surface area of many regions being increased in HIV+/cART+ children relative to controls. An increased rate of gain in the thickness of the right lateral pallidum and surface area of the left anterior accumbens of HIV+ children was observed when modeled longitudinally. Future studies including measures of metabolites via magnetic resonance spectroscopy and measures of cytokines would help to resolve whether the observed variation is due to inflammation stemming from excitotoxic damage to these regions. Given the proclivity of HIV for subcortical regions, particularly of the basal ganglia, this is a plausible explanation.

Chapters 5-7 focused more heavily on the development of prognostic, rather than descriptive, biomarkers. In chapter 5 we explored cross-sectional and longitudinal variation in subcortical morphometry among patients with MDD receiving ECT. We described differences between patients with MDD and unaffected controls as well as differences between patients who were responsive and unresponsive to ECT. Examined cross-sectionally, we reported reduced accumbens and pallidum volumes in patients versus controls prior to treatment. This corroborates prior reports of reduced striatal volumes in depressed cohorts (Koolschijn *et al*, 2009; Videbech, 1997). No shape-based differences were observed between patients with MDD and healthy controls, however. Among ECT patients, the left putamen increased in volume between baseline and the end of the ECT treatment index.

Morphometric differences were additionally observed based on subsequent patient responsivity to ECT. Specifically, responders had smaller overall accumbens volumes prior to treatment when compared to non-responders; the accumbens was additionally observed to increase among responders over treatment while moderate volumetric decreases were observed

over index in non-responders. Additionally, there were significant differential trajectories in the shape of the right medial pallidum and left superior caudate between responders and non-responders over index. These morphometric differences over index are consistent with the hypothesis that recovery from ECT is partially dependent on neuroplastic changes induced by treatment. But, whether these morphological variations are reflective of underlying inflammation resulting from the induced electrical current, the promotion of neurogenesis or both remains to be resolved and requires further investigation.

We further developed a support vector classifier using features of subcortical shape and volume to predict clinical response to ECT. We observed that pre-treatment measures of subcortical morphometry are capable of predicting response to ECT (i.e. a minimum of 50% improvement in mood) with an accuracy of 89%. However, the performance of this classifier was highly dependent upon which of three commonly used mood scales was used to assess patient response. Interestingly, it was a self-report scale that was the most predictive in isolation. It is unclear whether this gain in classification performance reflects an underlying strength in using the self-report scale (the QIDS) versus the clinician-administered scales (HAM-D and MADRS) or if certain chance alignment between the predictors in the feature set and outcome measures of the QIDS scale gave rise to this performance. Given the small sample size used in this study, the results merit independent replication.

The findings from this study provided additional evidence that ECT induces morphological changes (perhaps through inflammation and/or promotion of neurogenesis) in striatal and basal ganglia regions that are associated with clinical improvement and have the potential to inform personalized treatment. However, a further limitation of this study was that we did not relate characteristics of baseline features with later response. For example, is there a

characteristic profile of volume or shapes of these regions that are more associated with clinical response and, if so, what?

In chapter 6 we searched further for biomarkers of a more complete level of patient response to ECT, remission. We improved upon our earlier work in chapter 5 by probing our classifiers to obtain profiles of brain morphometry indicative of post-treatment remission or non-remission. We addressed a further limitation of chapter 5 by performing error averaging over repeated cross validation folds which allowed us to gauge our confidence in the classifier's estimates. Future work will additionally include sensitivity analyses of this classifier as in chapter 7. An additional development in this project was the use of data-driven approaches to clustering subcortical shape descriptors. This had the benefit of reducing the dimensionality of the classification problem (which had been the focus of chapter 2) while retaining our ability to refer to specific subfields of subcortical structures.

We reported three primary brain regions that were highly predictive of remission under this framework: the average local thickness of two regions of the anterior right hemisphere hippocampus and the right inferior temporal cortex. We probed the random forest model and observed that the predicted probability of remission decreased sharply as the thickness of these regions increased. We subsequently confirmed that pre-treatment thickness of the anterior hippocampus was strongly and significantly anticorrelated with improvement in mood scores over ECT index. Encouragingly, the temporal lobe structures identified by this data-driven framework are widely identified as being associated with symptom severity and recovery (Drevets *et al*, 2008) though they were selected from a wider collection of brain regions not normally associated with depression or recovery. Additional biologically relevant regions were identified (though less frequently). For example, structural and functional abnormalities are

frequently observed in serotonergically modulated emotional response circuitry, which include the accumbens, amygdala and pallidum which were also identified.

Future work in this area will focus on the development of classifiers having translational predictive abilities across independent sites. Though this was attempted using the UCLA and UNM cohorts, the results have so far not been compelling. However, a major confound of age exists between these two sites. Techniques for multisite classification such as domain adaptation in which subjects having similar characteristics across site are up-weighted in the training phase of classifier learning offer promising frameworks for overcoming these challenges. However, if an age disparity is the primary reason for sub-optimal classification performances an alternative strategy would be to develop classifiers based on windows of age ranges once adequately sized samples are available. Unfortunately, in the setting of cross-validation, we can not simply regress out confounding effects from training and testing folds using a single model as the resulting residualized values in the test set would be a partial function of values in the training folds thereby allowing for feedback between training and testing sets. However, again, given adequate sample sizes for both training and testing folds separate regression models could be fitted to training and testing folds independently; however, we currently do not have a sample size that would permit this approach.

Finally, chapter 7 introduced ongoing work in the area of patient risk stratification for relapse at 6-months following completion of ECT. We implemented an approach based on the classification process developed in chapter 6 except the use of shape features have not yet been applied. We compared brain imaging biomarkers predictive of subsequent relapse using features derived from pre-treatment, post-treatment and changes in brain structure over the course of treatment. Classifiers used features from both sites separately. Using these data-driven

approaches, we again constructed profiles of brain characteristics identified as likely and unlikely to relapse following reception of ECT. Models with reasonable levels of performance were subsequently evaluated using sensitivity analyses to both ensure that the observed performances were not arrived at through sheer chance combinations of subjects assigned to testing and training folds and to additionally determine whether influential/high-leverage subjects were influencing the fit of our models. Utilizing a wide parameter grid search, we were able to identify models with balanced accuracies above 70% for UCLA and UNM cohorts.

Future work will focus on the development of models with predictive value across sites. Again, the wide age differences between the UCLA and UNM cohorts introduced a confound of age-related brain differences which prevented classifiers from generalizing across sites. However, as we continue to recruit patients for these ongoing studies sample sizes will become amenable to the use of either domain adaptation or the training of age-range-specific models. We will additionally seek to predict changes in mood scales as continuous outcomes rather than arbitrary binary categories of response, remission and relapse.

Taken together, our work in both HIV and MDD demonstrates that high-dimensional shape data is an effective basis for biomarker discovery in MRI research and is likely to aid significantly in both predictive computer-aided diagnoses systems and future work in descriptive characterizations of neurological pathologies.

References

Canizares S, Cherner M, Ellis RJ (2014). HIV and aging: effects on the central nervous system. *Seminars in Neurology* **34**(1098-9021 (Electronic)): 27-34.

Cohen RA, Seider TR, Navia B (2015). HIV effects on age-associated neurocognitive dysfunction: premature cognitive aging or neurodegenerative disease? *Alzheimer's Research & Therapy* **7**(1758-9193 (Electronic)): 37.

Drevets WC, Price JL, Furey ML (2008). Brain structural and functional abnormalities in mood disorders: implications for neurocircuitry models of depression. *Brain structure & function* **213**(1-2): 93-118.

Koolschijn PC, van Haren NE, Lensvelt-Mulders GJ, Hulshoff Pol HE, Kahn RS (2009). Brain volume abnormalities in major depressive disorder: a meta-analysis of magnetic resonance imaging studies. *Human brain mapping* **30**(11): 3719-3735.

Phillips ML, Chase HW, Sheline YI, Etkin A, Almeida JR, Deckersbach T, *et al* (2015). Identifying predictors, moderators, and mediators of antidepressant response in major depressive disorder: neuroimaging approaches. *Am J Psychiatry* **172**(2): 124-138.

Videbech P (1997). MRI findings in patients with affective disorder: a meta-analysis. *Acta Psychiatr Scand* **96**(3): 157-168.